DESIGN AND VERIFICATION OF DIAMOND BASED CAPACITIVE MICROMACHINED ULTRASONIC TRANSDUCER

A THESIS SUBMITTED TO
THE GRADUATE SCHOOL OF NATURAL AND APPLIED SCIENCES
OF
MIDDLE EAST TECHNICAL UNIVERSITY

BY

AHMET MURAT ÇETİN

IN PARTIAL FULFILLMENT OF THE REQUIREMENTS
FOR
THE DEGREE OF MASTER OF SCIENCE
IN
ELECTRICAL AND ELECTRONICS ENGINEERING

FEBRUARY 2011

Approval of the thesis:

DESIGN AND VERIFICATION OF DIAMOND BASED CAPACITIVE MICROMACHINED ULTRASONIC TRANSDUCER

submitted by **AHMET MURAT ÇETİN** in partial fulfillment of the requirements for the degree of
Master of Science in Electrical and Electronics Engineering Department, Middle East Technical University by,

Prof. Dr. Canan Özgen _____
Dean, Graduate School of **Natural and Applied Sciences**

Prof. Dr. İsmet Erkmen _____
Head of Department, **Electrical and Electronics Engineering**

Assist. Prof. Dr. Barış Bayram _____
Supervisor, **Electrical and Electronics Eng. Dept., METU**

Examining Committee Members:

Prof. Dr. Cengiz Beşikci
Electrical and Electronics Eng. Dept., METU _____

Assoc. Prof. Dr. Şimşek Demir
Electrical and Electronics Eng. Dept., METU _____

Assoc. Prof. Dr. Haluk Külah
Electrical and Electronics Eng. Dept., METU _____

Assist. Prof. Dr. Barış Bayram
Electrical and Electronics Eng. Dept., METU _____

Dr. Said Emre Alper
Technical Vocational School of Higher Education, METU _____

Date: _____

I hereby declare that all information in this document has been obtained and presented in accordance with academic rules and ethical conduct. I also declare that, as required by these rules and conduct, I have fully cited and referenced all material and results that are not original to this work.

Name, Last Name: AHMET MURAT ÇETİN

Signature :

ABSTRACT

DESIGN AND VERIFICATION OF DIAMOND BASED CAPACITIVE MICROMACHINED ULTRASONIC TRANSDUCER

Çetin, Ahmet Murat

M.S., Department of Electrical and Electronics Engineering

Supervisor : Assist. Prof. Dr. Barış Bayram

February 2011, 94 pages

Potential applications such as high intensity focused ultrasound (HIFU) in medical therapeutics require larger output pressures. To offer unprecedented acoustic output pressure in transmit without the limitations, Capacitive Micromachined Ultrasonic Transducer (CMUT) operation modes of collapse and collapse-snapback are introduced in literature. Both operation modes require the membrane to contact the substrate surface, which poses a problem on the durability of the membrane in terms of structural integrity and tribological property. Large membrane deflection at collapse increases the stress within the membrane, and change of stress at ultrasound frequencies causes reduced lifetime and compromised reliability in these high output pressure operation modes.

Based on the additional requirements of these modes to reach high output transmit pressure at a sustainable transducer operation, diamond is proposed as the ultimate solution to be used as the membrane material. Mechanical (high Young's modulus, extreme hardness), thermal (large thermal conductivity, low thermal expansion coefficient), and electrical properties (insulator, large electrical breakdown field) of diamond are all in favor of its use in the microfabrication of CMUTs.

This thesis introduces the design and test results of the first diamond-based CMUTs as an alternative to silicon and silicon nitride based CMUTs. Simulations are performed using Finite Element Methods (FEM) using a commercially available software package, ANSYS.

The diamond-based CMUT is operated successfully both in air and immersion for the first time. A special experimental setup is prepared to gather huge amount of measurement data. Fully customizable in-house software is developed to command and control the test setup equipments for current dissertation and future work. Fresnel and Fraunhofer regions of the CMUT are characterized in sunflower oil using a combination of advanced hardware and software. The experimental results of radiation and diffraction for the diamond-based circular CMUT are verified by the theoretical calculations for a circular piston transducer. The results obtained from the first generation diamond-based CMUTs presented the diamond as a promising material for membranes in CMUTs.

Keywords: CMUT, Transducer, Diamond, Finite Element Analysis (FEA), Ultrasound

ÖZ

ELMAS TABANLI ULTRASONİK ÇEVİRGEÇLERİN TASARIMI VE DOĞRULANMASI

Çetin, Ahmet Murat
Yüksek Lisans, Elektrik ve Elektronik Mühendisliği Bölümü
Tez Yöneticisi : Yrd. Doç. Dr. Barış Bayram

Şubat 2011, 94 sayfa

Tıbbi tedavide, yüksek yoğunluklu odaklanmış ultrason gibi potansiyel uygulamalar büyük çıkış basınçları gerektirmektedir. Sınırlamalar olmadan iletimde görülmemiş akustik çıkış basıncı sunmak için, Kapasitif Mikroişlenmiş Ultrasonik Çevirgeçler için literatürde çökme ve çökme-bırakma çalışma modları tanıtılmaktadır. Her iki çalışma modu membranın taban yüzeyine temasını gerektirmektedir ki, bu yapısal bütünlük ve aşınma özelliği açısından membran dayanıklılığı üzerinde problem oluşturmaktadır. Yüksek çıkış basınçlı işletme modlarında çökme sırasındaki yüksek membran bükülmesi stresi artırmakta ve ultrasonik frekanslardaki stres değişimi ömrün kısalmasına ve güvenilirliğin tehlikeye girmesine sebep olmaktadır.

Bir çevirgeçin sürdürülebilir işletiminde yüksek çıkışlı basınç iletimine erişmek için bu modların ek gereksinimlerine dayanılarak, membran malzemesi olarak kullanılmak üzere elmas nihai çözüm olarak önerilmektedir. Elmasın mekanik (yüksek Young modülü, aşırı sertlik), termal (yüksek ısıl iletkenliği, düşük ısıl genleşme katsayısı) ve elektriksel (yalıtkanlık, yüksek elektriksel kırılma alanı) özellikleri, onun Kapasitif Mikroişlenmiş Ultrasonik Çevirgeçlerin mikro-üretiminde kullanılması lehindedir.

Bu tez, silikon ve silikon-nitrat tabanlı Kapasitif Mikroişlenmiş Ultrasonik Çevirgeç'lere alternatif olarak ilk elmas tabanlı Kapasitif Mikroişlenmiş Ultrasonik Çevirgeç'lerin tasarım ve test sonuçlarını göstermektedir. Simülasyonlar ticari olarak bulunabilen bir yazılım paketi, ANSYS, kullanılarak Sonlu Elemanlar Modeli ile gerçekleştirilmiştir.

Elmas tabanlı Kapasitif Mikroişlenmiş Ultrasonik Çevirgeç ilk defa hava ve sıvı içinde başarılı bir şekilde çalıştırılmıştır. Büyük miktarda ölçüm verisi toplamak için özel bir deneysel düzenek hazırlanmıştır. Mevcut çalışma ve gelecekteki işler için test düzeneğinin ekipmanlarını kumanda ve kontrol etmeye dönük tamamen özelleştirilebilir bir yazılım geliştirilmiştir. Kapasitif Mikroişlenmiş Ultrasonik Çevirgeç'in ayçiçek yağı içindeki Fresnel ve Fraunhofer bölgeleri gelişmiş donanım ve yazılım birleşimi kullanılarak karakterize edilmiştir. Elmas tabanlı Kapasitif Mikroişlenmiş Ultrasonik Çevirgeç'in ışınım ve dağılıma dair deneysel sonuçları dairesel piston çevirgeç için bulunan teorik hesaplamalar ile doğrulanmıştır. İlk nesil elmas tabanlı Kapasitif Mikroişlenmiş Ultrasonik Çevirgeç'lerden elde edilen sonuçlar, membranlar için elması gelecek vaad eden bir materyal olarak göstermektedir.

Anahtar Kelimeler: Kapasitif Mikroişlenmiş Ultrasonik Çevirgeç, Çevirgeç, Elmas, Sonlu Elemanlar Metodu, Ultrasonik

ACKNOWLEDGMENTS

I would like to thank to Prof. Dr. Cengiz Beşikci, Assoc. Prof. Dr. Şimşek Demir, Assoc. Prof. Dr. Haluk Külah and Dr. Said Emre Alper for their instructions and attendance to the presentation of this thesis.

I would like to express my sincere gratitude to Assist. Prof. Dr. Barış Bayram for his support, guidance and encouragement during my graduate study and the preparation stage of this thesis.

I would like to thank to members of ULTRAMEMS Research Group, Mehmet Cezar, Serra Altınoluk, Serdar Görümlü and Mehmet Yüksekkaya for sharing their knowledge, their support and hard work in the realization of first diamond-based CMUT project.

I would like to thank to my parents and family for their support and patience.

TABLE OF CONTENTS

LIST OF TABLES

TABLES

LIST OF FIGURES

FIGURES

CHAPTER 1

INTRODUCTION

1.1 Micro-Electro-Mechanical Systems

Micro-Electro-Mechanical Systems (MEMS) are used to define the systems composed of electromechanical devices created in a miniaturized world. Physical sizes change from micrometers to millimeters. Simple devices with no moving parts to complex devices can be designed with microfabrication technology in clean rooms and cost reduction can be obtained. One of the main criteria for a MEMS device is that there exist some elements showing mechanical functionality whether or not they can move [1]. Figure 1.1 shows the first rotary electrostatic side drive motors made with MEMS technology at UC Berkley in 1988.

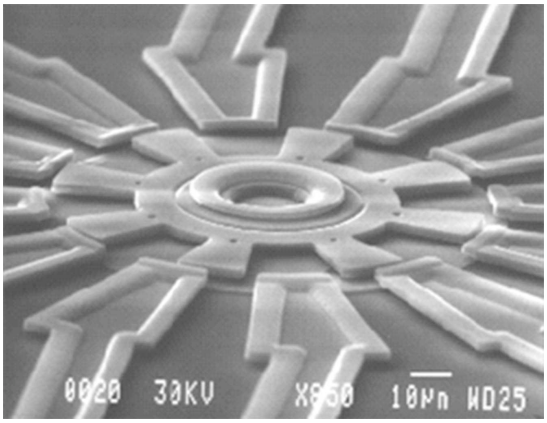

Figure 1.1: First Rotary Electrostatic Side Drive Motor [Richard Muller, UC Berkeley]. [2]

MEMS devices find more appliance in industry day by day. Sensors and actuators, using the

techniques of microfabrication, are developed for several different applications in industry (e.g. automotive, medicine, aerospace, meteorology etc.). Airbag systems, ink-jet printers, and projection systems are some products where the benefits of MEMS devices are introduced. Figure 1.2 shows that the market for MEMS devices was projected to reach $6.5 billion in July, 2010. The market is predicted to grow by $3 billion and reach $9.5 billion in 2014.

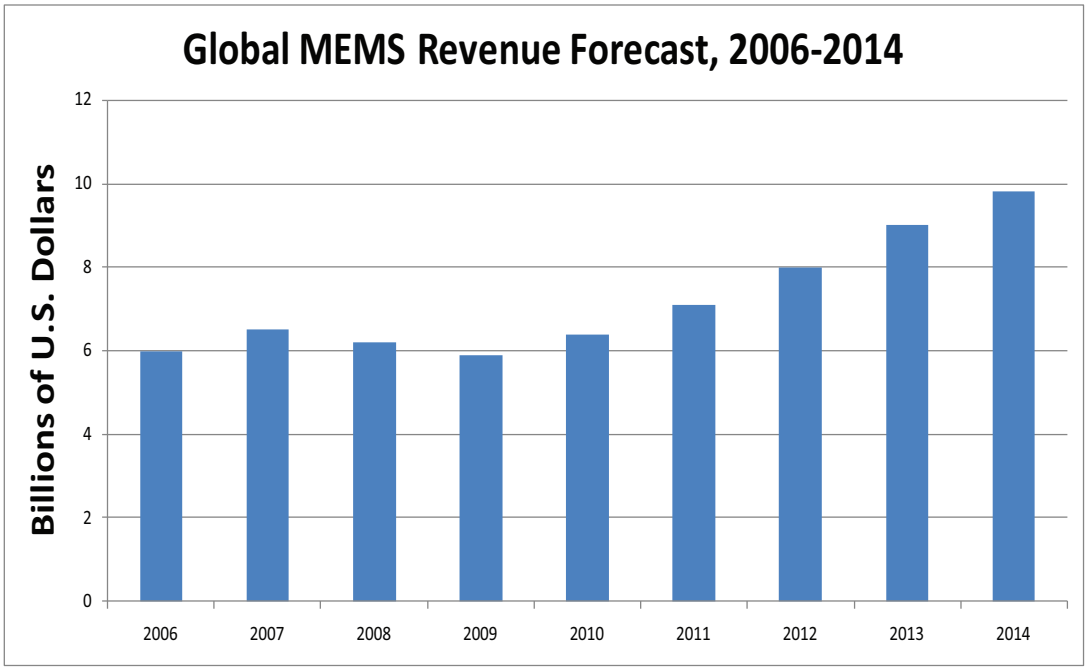

Figure 1.2: iSuppli's MEMS revenue forecast from 2006 to 2014 [3].

1.2 Transducers

A transducer converts one form of energy into another form (e.g. acoustic to electrical, electrical to light, etc.). There are several types of transducers. Pressure sensors, mass flow sensor, accelerometers, gyroscopes, antennas and infrared sensors can be listed as some of these. In industry or in daily life, these are used occasionally. As an example, ultrasonography devices are a kind of imaging system utilizing ultrasound and used in every hospital. These devices create images by converting acoustic pressure to electrical signals with the transducers built into them. Short pulses of sound waves are sent to body and returning waves are sensed

for diagnostics purposes. While sending acoustic waves, the input electrical energy of the transducer is converted into mechanical energy and vice versa in sensing mode.

Efficiency is an important parameter for transducers. There exist some amount of loss during the energy conversion. The efficiency for a transducer can be defined as the ratio of output energy to input energy.

Transducers can be developed by MEMS technology. This allows to produce small and cost-effective devices for many purposes. Accelerometers are one of these, which is widely known and used for airbag systems in automotive industry. Today, these MEMS based robust acccelerometers save life of many people in traffic accidents. Figure 1.3 shows an accelerometer designed using MEMS technology.

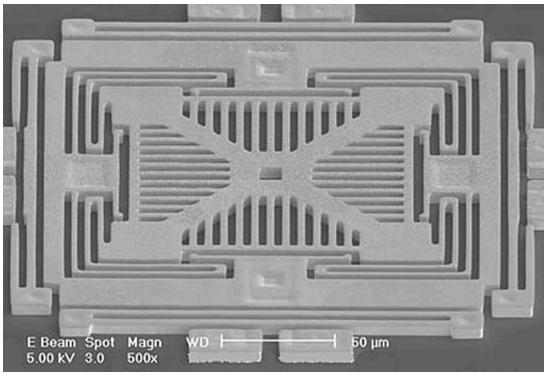

Figure 1.3: This micromechanical structure is the core of a 3-axis MEMS accelerometer. Such an open microstructure is very delicate, susceptible to degradation by dust, water, and almost any physical contact. Special tooling must be used to dice and package the chip, and hermetic packaging is required to ensure long-term reliability. [4]

1.3 Ultrasound

Acoustics was an art several years ago. Today, it is a field of science where complex behaviours of acoustic waves in different domains are studied and applied in industry. Acoustic waves are the result of oscillating pressure. When the frequency of oscillation is in the range of human hearing capability, it is named as sound. For higher frequencies above the upper limit of human hearing (greater than 20 KHz), it is defined as ultrasound. Ultrasound is used in many applications like medical imaging, ranging, flow metering, cleaning, non-destructive

evaluation, wafer temperature sensing [5]. To create ultrasonic waves at specific frequencies, transducers are utilized.

Piezoelectricity

$\Pi\iota\epsilon\sigma\eta$ (píesi) means pressure in Greek and ”piezo” comes from this word. Piezoelectricity is used to define the electricity caused by pressure. Jacques and Pierre Curie brothers were the first people who discovered, in 1880, that piezoelectric materials create electrical discharge when mechanical stress occurs on specific materials. Quartz, rochelle salts and tourmaline were elements on which piezoelectric effect was first observed. Alternately, the size of piezoelectric material changes when an electrical current is passed through.

Piezoelectric materials can be used in MEMS devices as a sensor to measure fluid density, fluid viscosity, impact force (e.g. airbag sensors) or to create acoustic waves in ultrasonic applications. Piezoelectric materials can be grouped as crystals and ceramics. SiO2 is a well-known piezoelectric material.

Piezoelectric materials are widely used to develop transducers in ultrasound applications. When solid medium is used for coupling of acoustic waves, piezoelectric transducers have good acoustic impedance match. However, when fluid (gaseous or liquid) is the coupling medium, piezoelectric transducers lack efficiency. The efficiency problem is caused by impedance mismatch between the piezoelectric transducers and fluid medium. Acoustic impedance of air is much lower than that of piezoelectric transducers. Acoustic impedance of water also mismatches with that of piezoelectric transducers. Impedance mismatch between piezoelectric transducers and air can be resolved to increase efficiency by using matching layers. However, this results with a lower bandwidth.

1.4 Capacitive Micromachined Ultrasonic Transducer

Capacitive Micromachined Ultrasonic Transducer (CMUT) is a device based on a capacitive structure which benefits from electrostatic forces created between two electrodes seperated from each other by a very small gap and is used to emit and receive acoustic waves at ultrasonic frequencies. Figure 2 shows an illustration of typical CMUT.

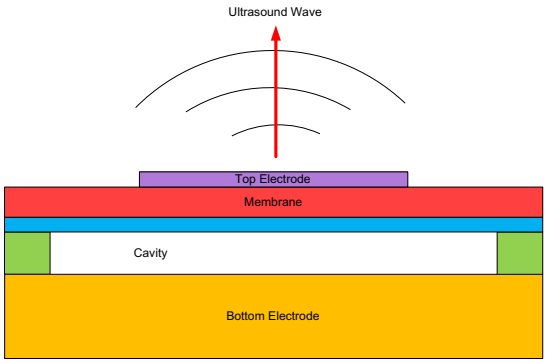

Figure 1.4: A cross-section of the cMUT [6].

In 1994, the first CMUT was invented at Stanford University [7]. In 1996, a new CMUT with an operating frequency above 10 MHz was developed. Micromachining technology allowed this to be a promising alternative to piezo-electric transducers [8]. It was a MUT with a silicon-nitride membrane suspended above silicon.

The idea of electrostatic transducers was as old as the piezoelectric transducers [9]. However, the need for high electric field for an efficient operation prevented the CMUTs to evolve as piezoelectric transducers. Then, later developments in micromachining technology allowed to build CMUTs competing with piezoelectric transducers. Advanced process technologies enabled to design CMUTs with submicron level gaps which let reasonable operational voltages to achieve high electric fields [9].

CMUTs can work in air with great impedance match and efficiency as well as in immersion [10]. Ultrasonic waves are produced or sensed through a coupling medium (i.e. gas, liquid or solid). While the vibrating part of the element is in use, it is not directly in contact with the subject. CMUTs have larger bandwidth in immersion, even at higher operational frequencies, when compared to piezo-based transducers [11].

1.5 Objectives and Organization of Thesis

Capacitive micromachined ultrasonic transducers (CMUTs) used in immersion are generally composed of vacuum-sealed cavities formed by membrane material [5]. The vacuum-sealed cavities are conventionally realized by two techniques. First one is the sacrificial release process where sacrificial material deposited before the membrane material is etched through the

etch holes, and etch holes are filled by deposition under low pressure to form the cavity [12]. The second one is direct wafer bonding method where two wafers (one having cavity patterning and the other having the membrane material) are bonded under elevated temperatures under vacuum [12].

Among these microfabrication methods, direct wafer bonding technology is more economical offering better process control, higher yield, and more novelties in CMUT designs than the sacrificial release process [13]. Direct wafer bonding technology enabled development of single crystal silicon membrane CMUTs rather than silicon nitride membrane ones. As the membrane and the substrate material are both silicon, direct wafer bonding at high temperatures (1100°C) is achieved without introducing any residual stress in the membrane [13]. Well-mature single crystal silicon technologies enable the specifications of the CMUT design be comfortably satisfied facilitating the realization of industrial grade CMUT products [12].

Energy conversion efficiency of CMUTs has been of primary importance for ultrasound applications, and improvement of this efficiency has been extensively studied for ultrasound transducers [14, 15]. Conventionally, the CMUT is biased at a voltage below the collapse voltage, and an AC signal is applied to generate ultrasound [5]. The efficiency of the transducer is drastically improved as the bias voltage approaches the close vicinity of the collapse voltage [15]. However, this high efficiency comes with a risk of membrane collapse onto the substrate. Additionally, the AC amplitude is limited to a small excitation voltage around a large bias voltage to prevent membrane collapse during operation. Therefore, the maximum output pressure of a CMUT is inherently limited by the requirements of the conventional operation.

For potential applications such as high intensity focused ultrasound (HIFU) in medical therapeutics, larger output pressures are essential. To offer unprecedented acoustic output pressure in transmit without the aforementioned limitations, novel CMUT operation modes of collapse [16] and collapse-snapback [17] are introduced. Both operation modes require the membrane to contact the substrate surface, which poses a problem on the durability of the membrane in terms of structural integrity and tribological property. Large membrane deflection at collapse increases the stress within the membrane, and change of stress at ultrasound frequencies causes reduced lifetime and compromised reliability in these high output pressure operation modes.

Collapse-snapback mode requires the collision of the contacting surfaces every cycle, and heat released needs to be dissipated quickly to maintain stable operation. Based on the additional requirements of these modes to reach high output transmit pressure at a sustainable transducer operation, diamond is proposed as the ultimate solution to be used as the membrane material. Mechanical (high Young's modulus, extreme hardness), thermal (large thermal conductivity, low thermal expansion coefficient), and electrical properties (insulator, large electrical breakdown field) of diamond [18] are all in favor of its use in the microfabrication of CMUTs. Chemical inertness and biocompatibility are further benefits of diamond for CMUTs to be utilized in corrosive environment and biological samples, respectively [18].

Diamond is a perfect membrane material candidate based on its material properties. However, unmature single crystal diamond (SCD) deposition technologies has prevented diamond membranes integration into CMUTs. Thin film SCD coated wafers are not commercially available for batch MEMS processes. Surface roughness of SCD is also high to be utilized for CMUT microfabrication based on direct wafer bonding technology.

Recently, with improvements in diamond material growth and technology, ultrananocrystalline diamond (UNCD) as a thin film were made commercially available. UNCD share a large portion of the benefits of the SCD with compromised features such as reduced resistivity due to graphitic forms enclosing polycrystalline diamond (SCD: insulator, UNCD: highly resistive). A remarkable feature of UNCD as a membrane material is its deposition as a thin film over a wafer surface with very low residual stress (i.e. < 50 MPa). UNCD, featuring smaller grain size and surface roughness has been recently explored for microelectromechanical systems (MEMS) applications such as RF MEMS resonators [19] and hybrid piezoelectric/UNCD cantilevers [20]. However, there are no studies of CMUTs with diamond membranes.

Microfabrication of CMUTs with diamond membranes (such as UNCD) - especially if based on the plasma-activated wafer bonding technology [21] - enables the utilization of key material properties of diamond such as high Young's modulus, extreme hardness and large thermal conductivity [18] to improve performance, reliability, and application range of CMUTs.

The objectives of this thesis are:

- To design the first diamond-based CMUTs in literature using Finite Element Methods.

- To characterize the first generation CMUTs both in air and immersion experimentally.
- To identify the Fresnel and Fraunhofer regions of the single transducer experimentally, and verify with theoretical diffraction calculations.

This thesis continues with Chapter 2 which gives an introduction to the CMUT theory. Chapter 3 includes all the details of CMUT design with Finite Element Methods and description of the mask used in manufacturing process. Chapter 4 shows the measurement results of the first generation diamond-based CMUTs both in air and immersion, and the verification of these results with theoratical calculations. Finally, Chapter 5 presents the conclusion of this dissertation.

CHAPTER 2

CMUT THEORY

2.1 Static Operation

Collapse and snapback voltages determine the operational characteristics of a CMUT. Since membrane is not a rigid structure, CMUT membrane bends as the electrostatic force increases. However, to solve the collapse voltage equation, some approximations has to be done. Thus, pressure on the CMUT membrane caused by the electrostatic force at any DC voltage level is assumed to be uniformly distributed [22].

Unbiased CMUT can be thought as a simple capacitor, where the stored energy is

$$E = \frac{1}{2}CV^2 \tag{2.1}$$

When the energy equation is differentiated with respect to membrane displacement, the electrostatic force on the membrane is [23]

$$F_{ele} = -\frac{d\left(\frac{1}{2}CV^2\right)}{dx} = \frac{\epsilon_0 A V^2}{2(d_0 - x)^2} \tag{2.2}$$

where V is the DC voltage applied to CMUT membrane, C is the capacitance between subsrate and the membrane and ϵ is the dielectric permittivity of vacuum, A is the area of the capacitor plates, x is membrane displacement, d is initial gap height.

In a simple model as shown in Figure 2.1, forces on the membrane can be represented as the

equilibrium between spring forces and electrostatic forces. Since we neglect the membrane bending and assume it to behave like a piston, linear spring constant gives

$$F_{mech} = kx \tag{2.3}$$

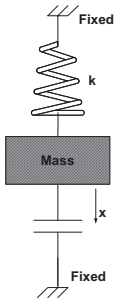

Figure 2.1: Simple lumped electro-mechanical model of CMUT.

In a first order model, total mechanical forces are equal to electrostatic forces exerted on the membrane. Thus,

$$m\frac{d^2x(t)}{dt^2} - \frac{\epsilon_0 AV^2(t)}{2(d_0 - x(t))^2 + kx(t)} = 0 \tag{2.4}$$

Equation (2.4) is a nonlinear differential equation of second order. However, in static operational mode of CMUT, steady-state solution can be found to be

$$kx = \frac{\epsilon AV^2}{2(d_0 - x)^2} \tag{2.5}$$

Equation (2.5) can be solved to find the relation between the membrane displacement and applied DC voltage [24].

$$V = \sqrt{\frac{2kx}{A\epsilon_0}}\,(d_0 - x) \tag{2.6}$$

Equation (2.6) can also be written as a 3rd order polynomial where a solution with only two positive real roots means the membrane is in equilibrium [8]:

$$\frac{2k}{A\epsilon_0}(x^3 - 2d_0x^2 + d_0^2x) - V^2 = 0 \tag{2.7}$$

As the voltage increases, membrane bends due to electrostatic forces. At a characteristic level, electrostatic force becomes larger than reverse mechanical force and the membrane collapses on the substrate [25]. This voltage level is named as collapse voltage and can be obtained by differentiating the above equation with respect to displacement:

$$\sqrt{\frac{k}{2A\epsilon_0 x}}(d_0 - x) - \sqrt{\frac{2kx}{A\epsilon_0}} = 0 \tag{2.8}$$

Hence,

$$x = \frac{d_0}{3} \tag{2.9}$$

where the electrostatic force is greater and the collapse voltage is

$$V_{collapse} = \sqrt{\frac{8kd_0^3}{27\epsilon_0 A}} \tag{2.10}$$

Equation (2.10) is an approximation assuming that membrane is a conductor. In case insulating material is used as a membrane, dielectric effect can be included as

$$V_{collapse} = \sqrt{\frac{8k}{27\epsilon_0 A}}(\frac{d_m}{\epsilon_r + d_0})^{3/2} \tag{2.11}$$

where ϵ_r is relative dielectric constant of the membrane and d_m is the membrane thickness.

Although Equation (2.11) gives the collapse voltage, assuming piston behavior for the membrane results in higher collapse voltage levels. A better result can be obtained if the bending of

membrane is considered. The membrane is assumed to be composed of infinitesimal elements which have different heights over the substrate as shown in Figure 2.2.

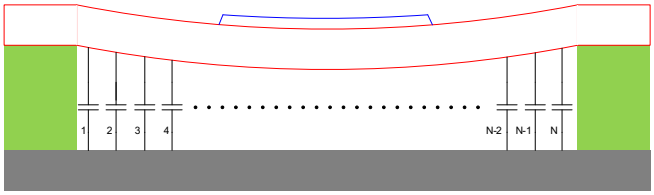

Figure 2.2: Total capacitance is the sum of capacitance values between the membrane and substrate. Membrane is a conductor in this figure. Deflected profile of the membrane causes varying capacitances.

Transducer is assumed to be circular. The varying distances cause different capacitance values composing the total capacitance of the transducer. Electrostatic force on a single element is [14]

$$F_i = \frac{\epsilon_0 V^2 A_i}{2d_i^2} \tag{2.12}$$

and

$$d_i = \frac{d_m}{\epsilon_r} + d_0 \tag{2.13}$$

where d_i is the effective distance, d_m is the membrane thickness, d_0 is the air gap and ϵ_r is the relative dielectric constant of the membrane. For a uniformly distributed force on a circular membrane, displacement of the circular element can be written as

$$w_i(r) = \begin{cases} \dfrac{F_i}{8D\pi}\left\{\dfrac{(r_m^2+b_i^2)(r_m^2-r^2)}{2r_m^2} + (b_i^2+r^2)\ln\dfrac{r}{r_m}\right\} & r > b_i \\ \\ \dfrac{F_i}{8D\pi}\left\{\dfrac{(r_m^2-b_i^2)(r_m^2+r^2)}{2r_m^2} - (b_i^2+r^2)\ln\dfrac{r_m}{b_i}\right\} & r \le b_i \end{cases} \tag{2.14}$$

where b_i is radius of circular element, F_i is the force applied and D is flexural rigidity. Using these equations and iterative numerical methods, collapse voltage can be found.

Snapback voltage is one of the CMUT characteristic parameter. When membrane is collapsed electrostatic force is greater than spring force. Membrane does not begin to restore its shape abruptly when the applied voltage is decreased. There exists a hysteresis effect between collapse and snap-back voltages. Snap-back voltage for a non-conducting membrane can be written as

$$V_{snapback} = \sqrt{\frac{2kd_0d_m^2}{\epsilon_m A}} \tag{2.15}$$

2.2 Dynamic Operation

When CMUT is biased with DC voltage below collapse voltage, AC voltage is applied above it to create a vibrating CMUT. Electrostatic pressure can be written as [8];

$$P_E(r) = \frac{\epsilon_0\epsilon_m^2(V_{DC}^2 + 2V_{DC}V_{AC}cos(\omega t) + V_{AC}^2cos(\omega t)^2)}{2\left[t_m\epsilon_0 + (t_a - x(r))\epsilon_m\right]^2} \tag{2.16}$$

where ω is the operating frequency, t_m is the membrane thickness, t_a is the air gap distance, and ϵ_m is the relative permittivity of the membrane. For $V_{DC} >> V_{AC}$, CMUT can be operated in a linear region. The membrane deflection is caused by the superposition of both static and dynamic terms. The frequency of the applied AC signal should be same as the resonance frequency of the membrane [8].

2.3 Energy Conversion Efficiency

When a CMUT is excited with AC signal, acoustic waves are produced with the mechanical response of the membrane. The transducer converts the electrical energy at its input to mechanical energy. The efficiency of this conversion is defined with the electromechanical coupling coefficient, which is the ratio of the produced mechanical energy to the total energy stored in the transducer. The equation is [14]:

$$k_T^2 = \frac{E_{mech}}{E_{total}} = \frac{E_{mech}}{E_{mech} + E_{elec}} \tag{2.17}$$

Coupling coefficient can be easily obtained if piston-shaped parallel plate capacitor approximation is used. Membrane bending is ignored and the capacitor top plate is assumed to be supported by a spring while bottom plate is fixed. The electromechanical coupling coefficient for this model is [14]:

$$k_T^2 = \frac{2x}{d_0 - x} \tag{2.18}$$

where d_0 is the initial gap between the electrodes and x is the displacement of the top electrode. However, membrane dielectric effect shall also be included for a CMUT with top electrode positioned on the membrane top surface. Then coupling coefficient can be written as:

$$k_T^2 = \frac{2x}{d_0 + \frac{d_m}{\epsilon_r} - x} \tag{2.19}$$

where d_m is the membrane thickness and ϵ_r is the relative dielectric coefficient of membrane.

Equation 2.19 gives the coupling coefficient until displacement of top plate is one third of initial effective gap. Equation 2.9 shows that membrane collapses when the displacement is one third of effective distance. At this point, coupling coefficient has its maximum value which is 1.

Fraser *et al.* [26] calculates k_T^2 for CMUT membrane using fixed capacitance C^S and free capacitance C^T. C^S is the total capacitance of the transducer at any DC voltage bias and C^T is the slope of the charge-voltage curve [15]. Coupling coefficient is defined as [26]:

$$k_T^2 = 1 - \frac{C^S}{C^T} \tag{2.20}$$

Ignoring the parasitic capacitances, fixed capacitance and free capacitance are written as:

$$C^S = \frac{\epsilon_0 A}{d_{eff} - x}$$
$$C^T = \frac{\epsilon_0 A}{d_{eff} - 3x} \tag{2.21}$$

2.4 Equivalent Circuit

CMUT is a system composed of electrical and mechanical parts, which is named an electromechanical device. The problems for an electromechanical system can be solved analytically using an equivalent electrical circuit. Voltage sources can be used to represent mechanical forces and current sources can replace velocities. The equivalent circuit of a CMUT can be shown as in Figure 2.3 [24, 27].

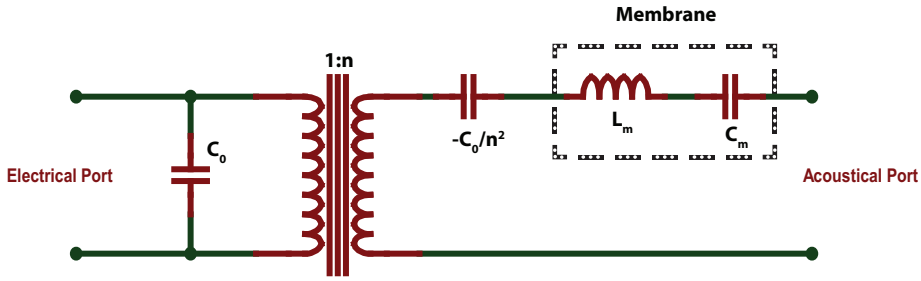

Figure 2.3: EquivalentCircuit.

Transformer is used to define the conversion between electrical input and mechanical ouput. The conversion ratio, n, gives the sensitivity of the transducer. Equation 2.22 shows that increasing the CMUT membrane size or decreasing the gap between the substrate and the membrane improves the sensitivity.

$$n = \frac{\epsilon_0 A}{(d_{eff} - x)^2} \tag{2.22}$$

2.5 Radiation

Ultrasonic transducers have different radiation patterns which change according to their sizes and operational frequencies. The radiation from a point source is introduced to start with. This section gives a general guideline for the radiation of ultrasonic waves. Then, an outline for the emission from a circular piston transducer is provided.

2.5.1 Point Source

Point sources radiate waves in spherical uniformity. Simple wave equation can be used as a starting point [28, 29].

$$\Delta^2 p - \frac{1}{c^2}\frac{\partial^2 p}{\partial t^2} = 0 \tag{2.23}$$

where p is pressure and c is wave speed. This equation can be expanded for cartesian coordinates as

$$\frac{\partial^2 p}{\partial x^2} + \frac{\partial^2 p}{\partial y^2} + \frac{\partial^2 p}{\partial z^2} - \frac{1}{c^2}\frac{\partial^2 p}{\partial t^2} = 0 \tag{2.24}$$

and in spherical coordinates

$$\frac{1}{r^2}\frac{\partial}{\partial r}\left(r^2\frac{\partial p}{\partial r}\right) + \frac{1}{r^2}\frac{1}{sin\theta}\frac{\partial}{\partial \theta}\left(sin\theta\frac{\partial p}{\partial \theta}\right) + \frac{1}{r^2 sin^2\theta}\frac{\partial^2 p}{\partial \psi^2} - \frac{1}{c^2}\frac{\partial^2 p}{\partial t^2} = 0 \tag{2.25}$$

Since the pressure is not dependent on angular variations, Equation (2.25) can be written in one dimension as

$$\frac{1}{r^2}\frac{\partial}{\partial r}\left(r^2\frac{\partial p}{\partial r}\right) - \frac{1}{c^2}\frac{\partial^2 p}{\partial t^2} = 0 \tag{2.26}$$

or

$$\frac{\partial^2(pr)}{\partial r^2} - \frac{1}{c^2}\frac{\partial^2 p}{\partial t^2} = 0 \tag{2.27}$$

Acoustic impedance is written as

$$Z = \rho V_0 \frac{k^2a^2}{1+k^2a^2} + j\rho V_0 \frac{ka}{1+k^2a^2} \tag{2.28}$$

and the particle velocity is

$$\upsilon = \frac{A}{a} e^{j(\omega t - ka)} \tag{2.29}$$

Assuming continuity of radiation and for $ka << 1$

$$A = j\rho_0 V_0 k a^2 \upsilon_0 \tag{2.30}$$

Thus, pressure equation for a point source is [28]

$$p = \frac{A}{r} e^{j(\omega t - ka)} = \frac{j\rho_0 V_0 k a^2 \upsilon_0}{a} e^{j(\omega t - ka)} \tag{2.31}$$

2.5.2 Circular Piston Transducer

A circular CMUT, as shown in Figure 2.4, can be approximated as a circular piston in an infinite baffle in ultrasonic radiation analysis [28]. Circular piston is rigid and all points on the surface vibrate in phase. Acoustic waves are radiated in the forward direction only. Huygen principle can be used to solve the wave equation. Each point on the piston surface is treated to contribute as a single source element and wave propagation is superposition of waves radiated from these elements. Hence the pressure at a distance r is,

$$dp = \frac{j\rho_o V_o k}{2\pi r} \upsilon dA e^{j(\omega t - kr')} \tag{2.32}$$

where ρ_0 is the density of the medium, V_0 is the velocity of sound in the medium, k is the wave number, υ is the amplitude of the surface velocity at an angular frequency of ω, r is the distance from the transducer center, and r' is the distance from the transducer surface.

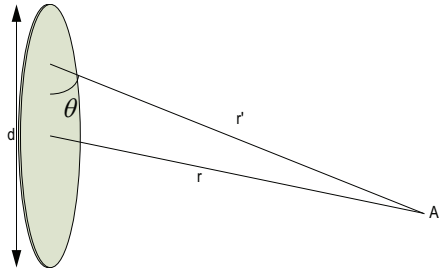

Figure 2.4: Source element vibrating on a circular piston with diamater d and located at a distance r.

This expression can be integrated to find total pressure at a point in a region. The regions are splitted in two parts: Far Field (Fraunhofer) and Near Field (Fresnel).

Far Field

$$r^{'} = \sqrt{r_2 + y_2 - 2rysin\theta cos\phi} \tag{2.33}$$

For $r >> d$, the region is defined as Fraunhofer (Far Field) region. When Equation 2.33 is expanded in Taylor's series with approximation,

$$r^{'} = r - sin\theta cos\phi \tag{2.34}$$

Using Equation 2.34, total pressure at point A can be integrated as,

$$p = \frac{j\rho_0 V_0 k}{2\phi r}\upsilon_0 e^{j(\omega t - kr)} \int_0^{d/2} xdx \int_0^{2\pi} e^{jkxsin\theta cos\phi} d\phi \tag{2.35}$$

where $r^{'} = r$ for amplitude part.

Bessel functions of the first kind can be used to integrate Formula 2.35.

$$\int_0^{2\pi} e^{-j(kySin\theta Cos\phi d\phi)} = J_0(kysin\theta) \tag{2.36}$$

$$\int_0^{d/2} J_0(kysin\theta)xdx = xJ_1(x) \tag{2.37}$$

and

$$p = \frac{j\rho_0 V_0 ka^2}{2r} \upsilon_0 e^{j(\omega t - kr)} \left[\frac{2J_1(kasin\theta)}{kasin\theta}\right] \tag{2.38}$$

where ρ_0 is the density of the medium, V_0 is the velocity of sound in the medium, k is the wave number, a is the radius of the transducer, υ_0 is the amplitude of the surface velocity at an angular frequency of ω, r is the distance from the transducer center, and θ is the angle with the transducer normal. The term in brackets which contains Bessel function is known as directivity function and shown in Figure 2.5. The directivity specifies the pressure variation with direction [28]

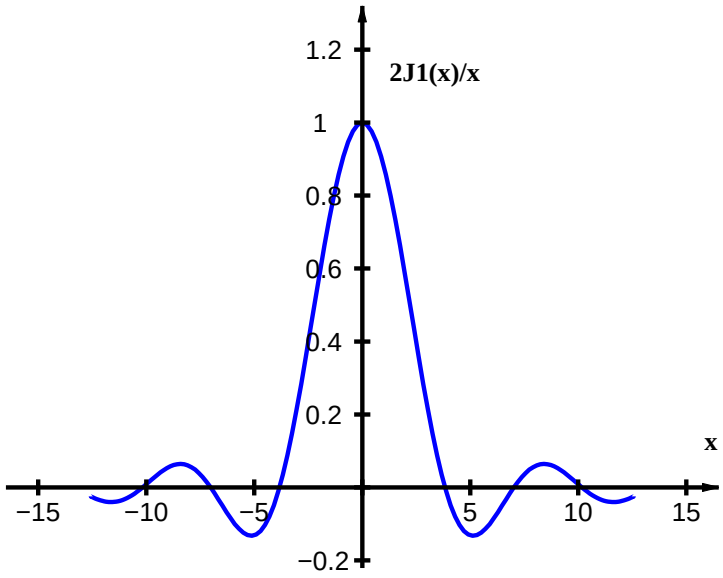

Figure 2.5: Directivity function for the circular piston transducer for pressure.

Directivity function helps us to characterize the radiation pattern of a transducer. The output pressure radiated from a transducer does not travel in one focused direction only. Although maximum energy is obtained on the axis which is normal to and at the center of the circular transducer, some part of the energy radiates through the side paths. The main beam contains the maximum energy. Side lobes are the unwanted parts on a radiation pattern. In transmitting mode, circular transducer causes interference with its sidelobes in an operating environment. As a sensor, a circular transducer gets interference due to high side lobe gain. Figures 2.6, 2.7 and 2.8 show polar diagrams of radiation patterns for a circular transducer operating in different frequencies in the same medium.

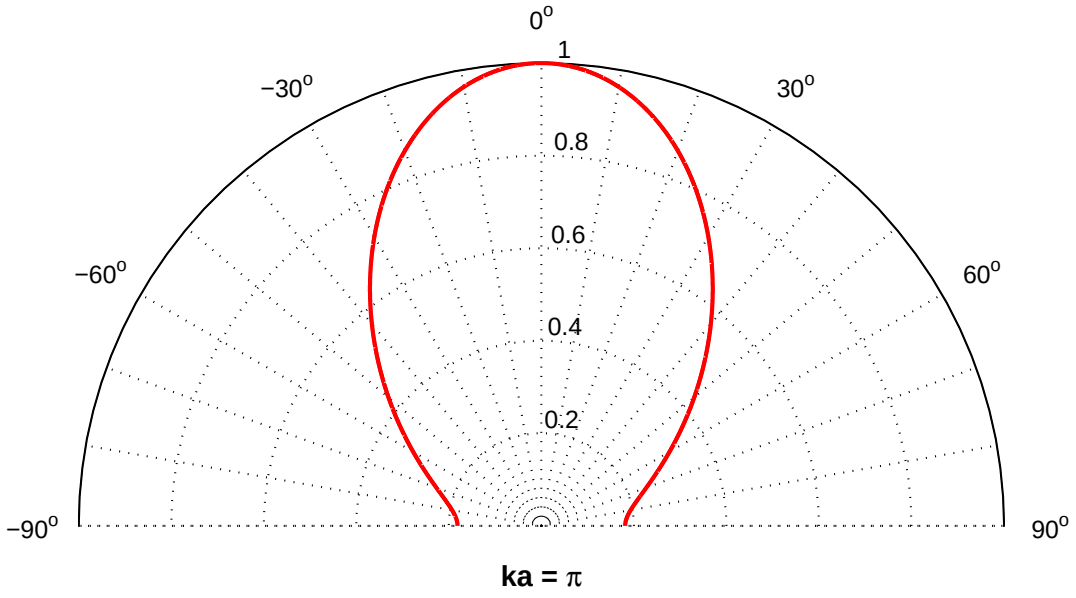

Figure 2.6: Radiation pattern of circular piston transducer in linear scale for $ka = \pi$.

It is obvious that beamwidth of main lobe decreases as the ratio of transducer radius and wave length increases. Figures 2.9, 2.10 and 2.11 allow a better understanding of the sidelobe effect. It is shown that 3 dB beamwidth is narrower and gain levels of sidelobes are much lower at higher frequencies. Narrow beamwidth means better targeting capability and non-interference operation.

Near Field

Fresnel region is the near field region. Fresnel distance can be found by integrating the Equation 2.32 for $r' = \sqrt{r^2 + \sigma^2}$ [28],

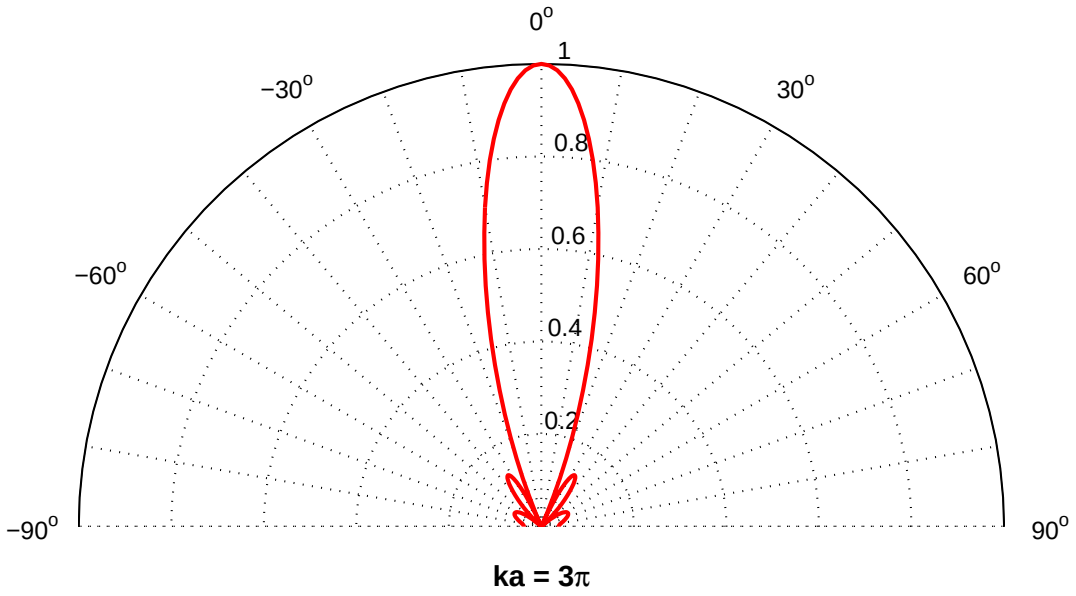

Figure 2.7: Radiation pattern of circular piston transducer in linear scale for $ka = 3\pi$.

$$p = \rho_0 V_0 \upsilon_0 e^{(j\omega t)} \left(e^{-jk\sqrt{r^2+\sigma^2}} - e^{-jkr} \right) dA \tag{2.39}$$

and getting the real part,

$$p = \rho_0 V_0 \upsilon_0 a^2 \sqrt{[2 - 2cosk(\sqrt{r^2+z^2} - z)]} \tag{2.40}$$

In near field, there are several peaks of acoustic waves as shown in Figure 2.12. The interference caused by point sources on transducer surface is eliminated at Fresnel distance.

We can find the distances where the peaks occur such that

$$z = \frac{4r_0^2 - n^2\lambda^2}{4n\lambda} \tag{2.41}$$

where maximums occur if n is odd and minimums occur if n is even. Farthest maximum occurs at n=1, which is $z_F = a^2/\lambda$. Fraunhofer (Far Field) region starts at $z = z_F$. The circular transducer starts to behave like a point source in far field.

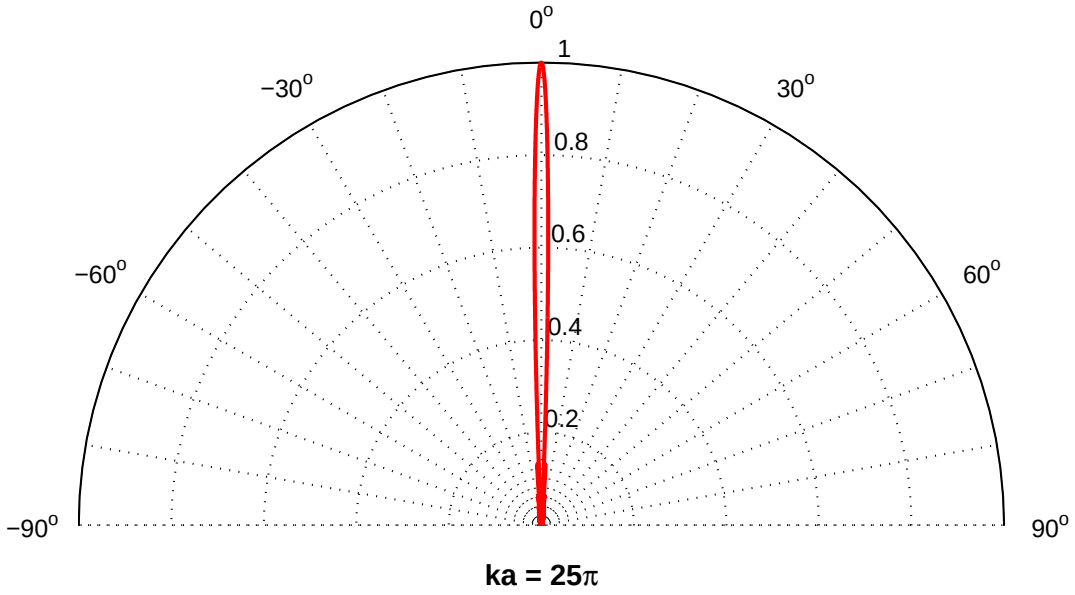

Figure 2.8: Radiation pattern of circular piston transducer in linear scale for $ka = 25\pi$.

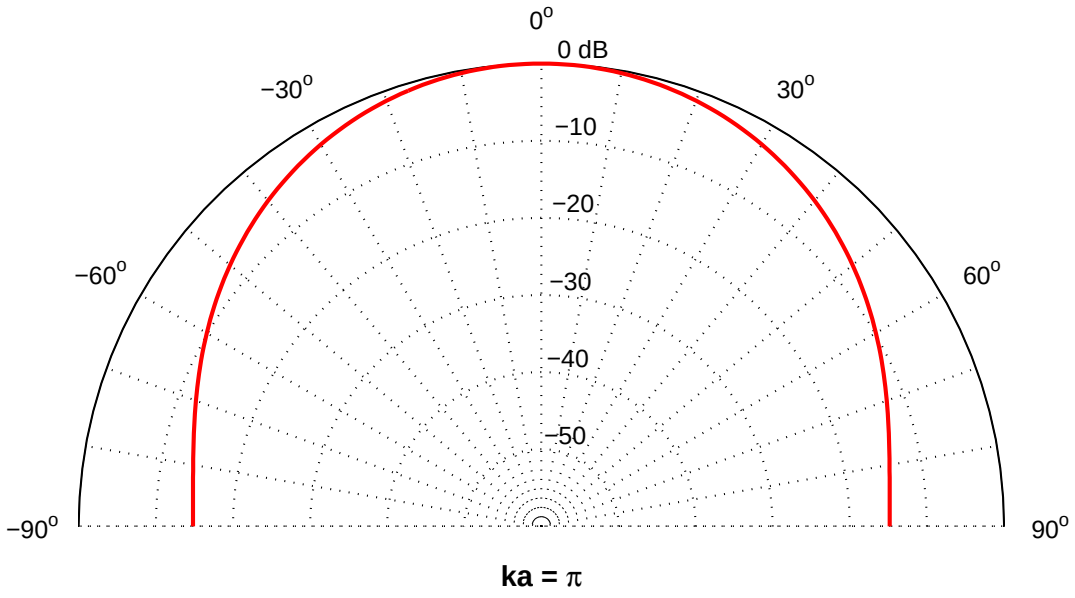

Figure 2.9: Radiation pattern of circular piston transducer in logarithmic scale for $ka = \pi$.

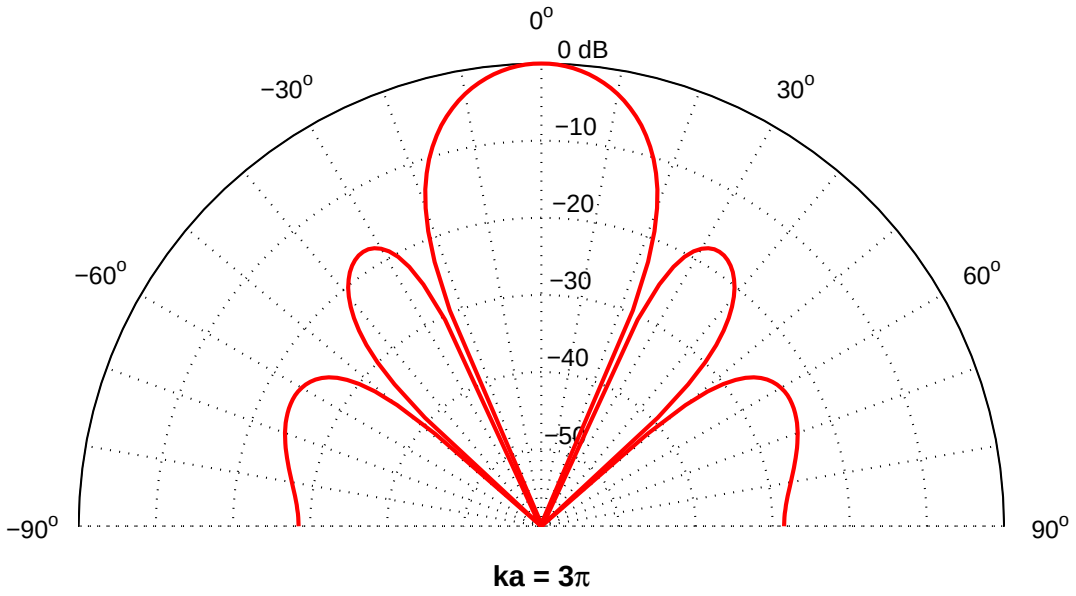

Figure 2.10: Radiation pattern of circular piston transducer in logarithmic scale for $ka = 3\pi$.

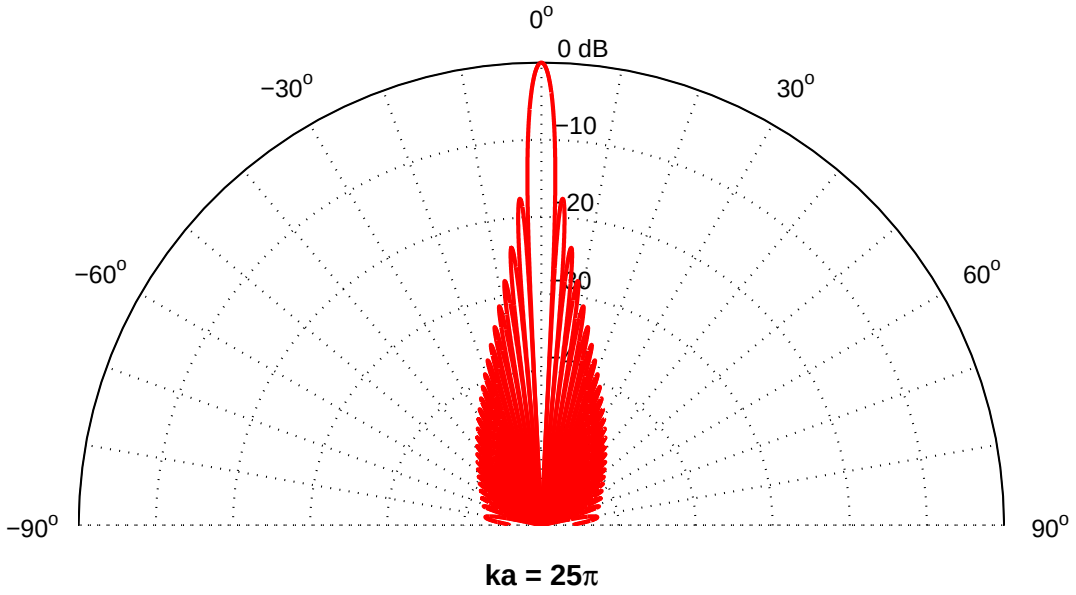

Figure 2.11: Radiation pattern of circular piston transducer in logarithmic scale for $ka = 25\pi$.

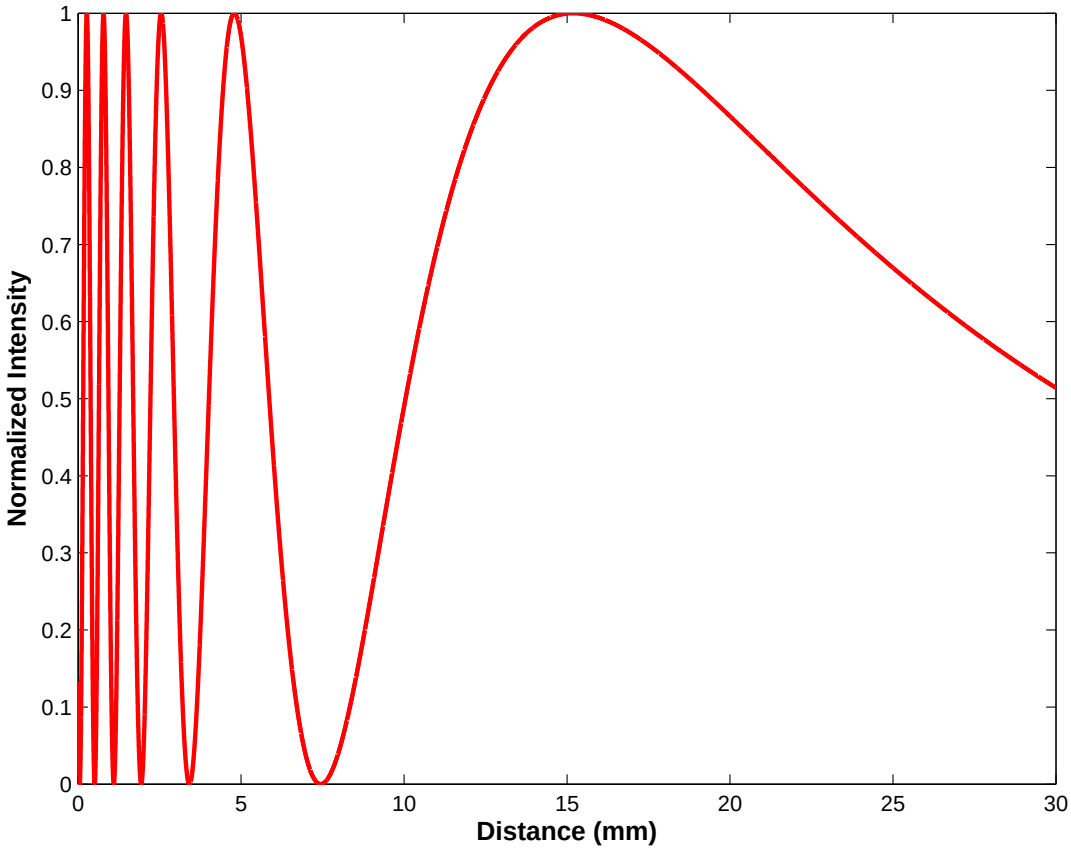

Figure 2.12: Normalized pressure intensity on the axis normal to and at the center of circular transducer surface. Transducer radius is 2.5 mm. Fresnel distance is 15mm where the last peak occurs.

CHAPTER 3

FINITE ELEMENT ANALYSIS AND DESIGN

3.1 Introduction

FEA (Finite Element Analysis) uses numerical methods to simulate behaviour of products in several environments. Using this method and some approximations, solving complex nonlinear partial differential equations is possible in a reasonable duration, based on PCs with high processing power.

In industry, 2D modeling and 3D modeling are two types used for modeling the product. If the product has a symmetrical structure, 2D modeling can be used to simplify the problem and simulate in less time while sacrificing some accuracy. 3D modeling gives more accurate results but complexity of the problem increases. A 3D model needs more time and more computer processing power to simulate.

Basically, upon modelling the product, a complex mesh is created. Mesh is the result of subdividing the model into several elements and these elements are composed of several nodes. According to the type of the problem, suitable element types with required degrees of freedom are chosen. Equations are solved iteratively using pre-defined boundry conditions and degrees of freedom defined for the each element. Element types are chosen carefully to decrease the solution time. Mesh is created in a way to prevent non-converged results.

Today there are commercially available software packages to solve these time-consuming and complex problems. Each has some advantages and disadvantages when compared to each other. ANSYS (ANSYS Inc., PA, USA) is used as a software package for simulation in this study.

3.2 Modeling

CMUT cell is created with diamond membrane on a silicon substrate. Membrane is supported on silicon-dioxide creating a vacuum gap between the silicon substrate and diamond membrane. A layer of high temperature oxide is created on the diamond membrane to be able to bond the wafers. Aluminim electrode is used on top of the membrane. The schematic cross section of the CMUT cell is shown in Figure 3.1.

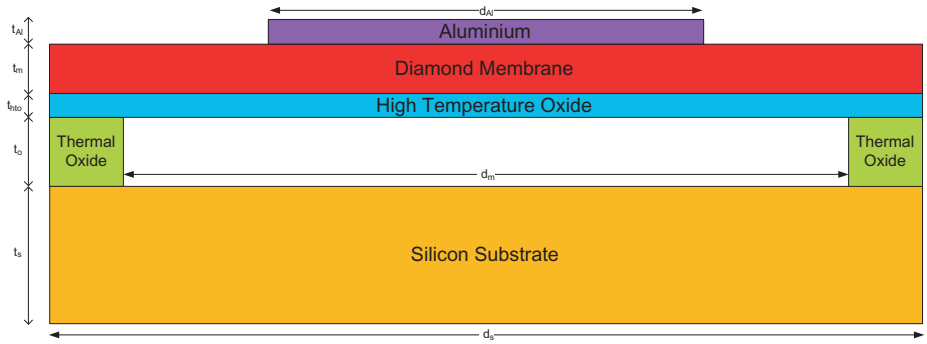

Figure 3.1: Schematic cross section of the single CMUT cell

Material properties used in these simulations are given in 3.1

Table 3.1: Material properties used in ANSYS simulations.

Materials	Poisson Ratio	Young's modulus (GPa)	Density (kg/m3)	Relative Permittivity
Diamond	0.07	850	3300	5.68
Si	0.29	169	2332	11.8
Aluminium	0.35	70	2700	
SiO_2	0.17	75	2200	3.78
Vacuum	---	---	---	1

Finite Element Analysis is performed for CMUTs with different sizes using commercially available software, ANSYS (ANSYS Inc., PA, USA). Since single CMUT has a rotational symmetry, a 2D model is created with axisymmetric elements for electrostatic analysis.

PLANE42, which is defined by four-nodes, with stress stiffening and large deflection capabilities are used for structural meshing. Boundary conditions are set by defining DOF (degree of freedom) values for structural elements. Atmospheric pressure is applied as surface load on the element faces of membrane and the top electrode. A coupled electrostatic-structural analysis is performed to get the simulation results. Vacuum area inside the sealed region under membrane is defined to be morphed during analysis.

CONTA171 with TARGE169 are used as contact-target elements. These elements are located on the surfaces of substrate and High Temperature Oxide (HTO) to detect the contact through penetration when the membrane deflection occurs under atmospheric and electrostatic loads. Target-contact elements have same material properties with surfaces they stick to.

An 8-node charge-based electric element, PLANE121, with only one degree of freedom, voltage, is used to define physical properties for static analysis.

Mapped meshing is used for the components to get converged results in a resonable time. Smaller sizes are used for components where large deflection occurs. Meshed model of the single cell is shown in Figure 3.2.

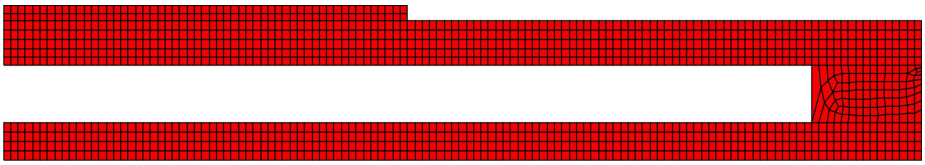

Figure 3.2: Axisymmetric mesh model of the single CMUT cell

The structure is supported at the bottom and clamped at the symmetry axis to prevent movement in the horizontal direction since this is an axisymmetric structure [Figure 3.3].

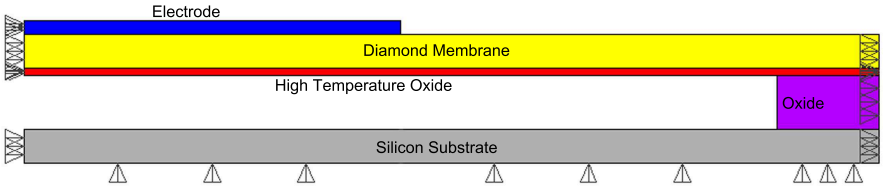

Figure 3.3: Structural boundry conditions applied to the axisymmetric model of the single CMUT cell

3.3 Static Analysis

Static analysis is performed to obtain the steady-state status of a structure under applied static loads [30]. The effects of loads changing with the time are not included in this analysis unless they are approximated as static equivalent loads. Inertia and damping effects are ignored. Stress values and distribution on the structure, nodal displacement values of the structure and nodal forces are the results which can obtained by a structural static analysis. External forces, steady-state inertial forces, displacements and temperatures are some of the loads which can be applied.

ANSYS allows to perform a static analysis of structures with linear or non-linear material properties. All these are introduced in a command file which also includes the model description, analysis parameters, calculations and export functions for post-processing. Static analysis of the CMUTs with diamond membranes are performed to find the effect of air pressure on membrane deflection, calculate stress values and determine collapse-snapback voltages. The analyses are performed on 3 Dell T5400 workstations with 2x QuadCore Intel Xeon E5420 (2500 MHz) CPU and 8 GB memory. CPU intensive and time consuming analyses are performed in a distributed progress on 3 workstations at the same time.

3.3.1 Air Deflection

Although the CMUT is not biased with a DC voltage, membrane deflection occurs due to air pressure in the operational environment. The vacuum between the diamond membrane and the silicon substrate causes this deflection under atmospheric pressure. Atmospheric pressure creates uniformly distributed forces on the diamond membrane and aluminium electrode. It is

applied as surface load on the selected lines (i.e. top line of membrane and electrode areas). The forces caused by suraface loads are transferred to mesh elements during the simulation. As the membrane deflection occurs at each iterative step during simulation, ANSYS uses morphing. Movement of non-structural elements (i.e. vacuum between membrane and substrate) are constrained by applying boundry conditions on displacement degrees of freedom. Mesh displacements of non-structural elements are used to prevent mesh distortion.

Diamond membrane has material properties such as high Young's Modulus and extreme hardness. However, since the thickness of the membrane is not very high, varying deflections based on membrane radii occur.

In a CMUT design, residual stress caused by manufacturing process is an important factor to be avoided. Thermal expansion coefficient defines the volumetric change of material structure under different thermal conditions. Since thermal expansion coefficient of diamond is lower than that of silicon, some amount of compressive stress may occur on the membrane. ANSYS lets us to define pre-stressed models in the static structural simulations. Compressive stress causes the diamond membrane deflection profile to change. Results of static structural simulation for different CMUT radii and compressive stress values on the diamond membrane are given in Table 3.2.

Table 3.2: Natural deflection values under atmospheric pressure for CMUTs with different radii and residual compressive stress.

Compressive Stress (MPa)	Deflection (µm)				
	60-µm	44-µm	36-µm	27-µm	22-µm
0	0.2615	0.0793	0.0364	0.0121	0.00554
100	0.3964	0.0996	0.0422	0.013	0.00579
200	0.6595	0.1337	0.0503	0.0142	0.00606
300	1.011	0.2005	0.06221	0.0155	0.00639
400	1.33	0.3599	0.0813	0.0173	0.00677

The values in Table 3.2 are deflection of collapsed nodes on the membrane where maximum

displacement occurs. Since this is a circular CMUT, these points are the centers of membranes.

As it can bee seen, membrane deflection increses as the radius of the membrane increases. Residual compressive stress also increases the displacement of nodes on the membrane. However, after a treshold value, membrane profiles show unexpected behaviours. Membrane deflection profiles for CMUTS with radii 60 μm, 44 μm, 36 μm, 27 μm and 22 μm are given in Figures 3.4, 3.5, 3.6, 3.7 and 3.8 respectively.

The lines in the figures represent the cross-sections of circular membranes when their shapes are changed due to atmospheric pressure. Each line in a figure shows the behaviour of membranes with different residual compressive stress values. Since the transducer structure has an axisymmetric circular shape, only half of the membrane cross-section is given. Negative deflection values mean that the membrane is bending through the substrate and positive deflection values mean that the membrane is bending up.

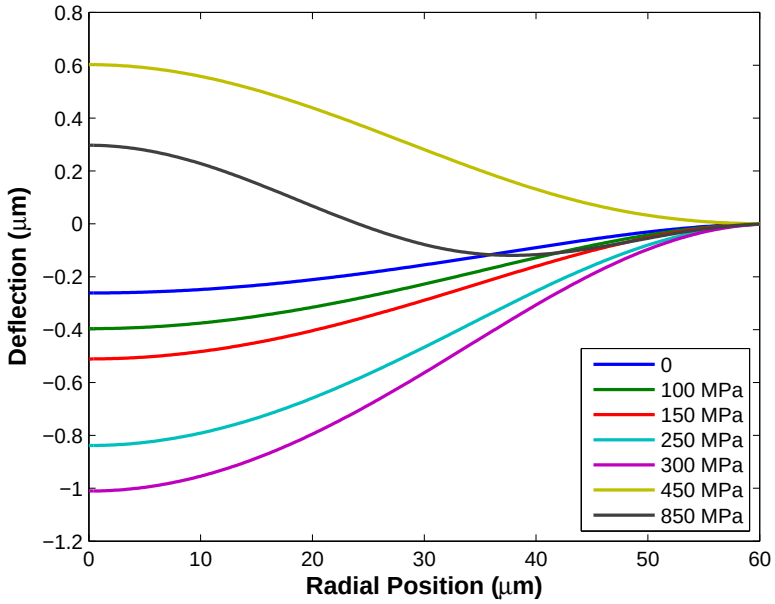

Figure 3.4: Deflection profile for a CMUT with radius 60μm and the effect of compressive stress.

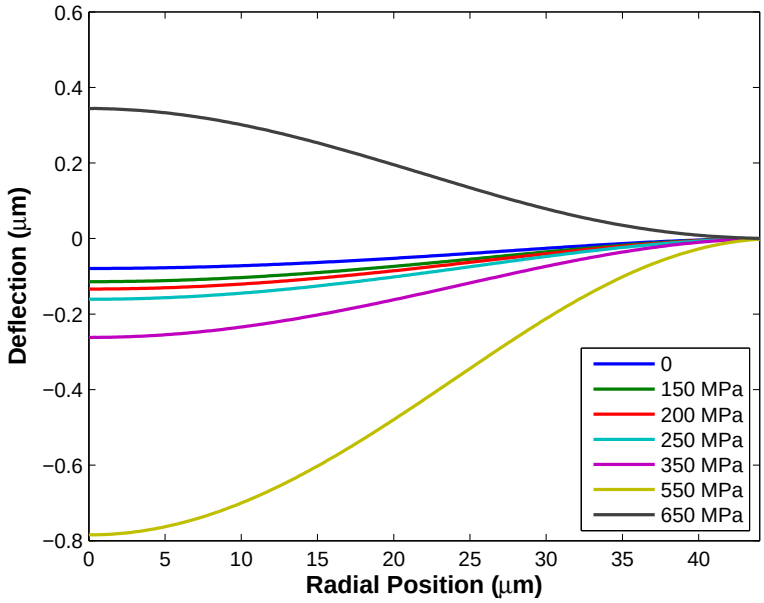

Figure 3.5: Deflection profile for a CMUT with radius 44μm and the effect of compressive stress.

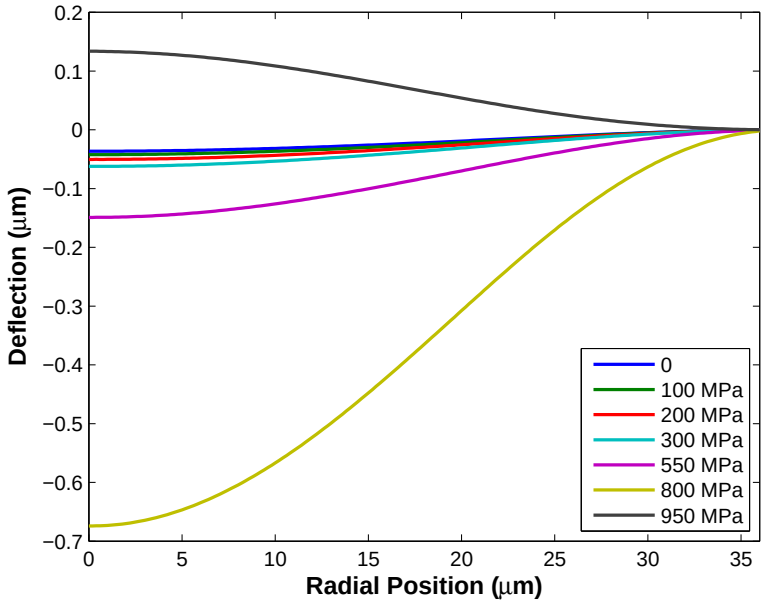

Figure 3.6: Deflection profile for a CMUT with radius 36μm and the effect of compressive stress.

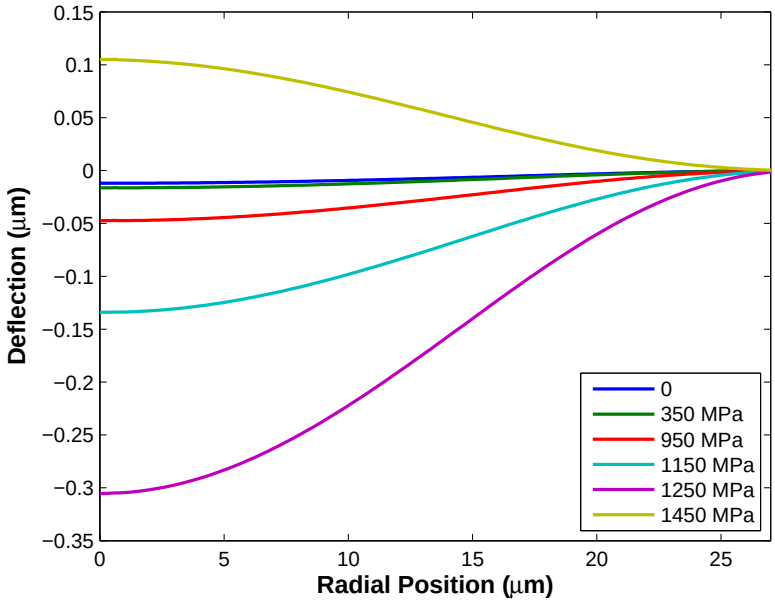

Figure 3.7: Deflection profile for a CMUT with radius 27μm and the effect of compressive stress.

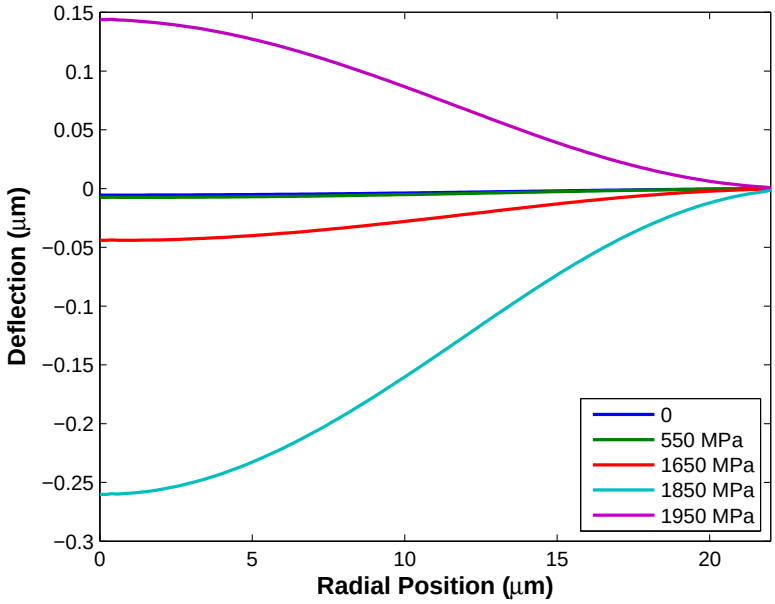

Figure 3.8: Deflection profile for a CMUT with radius 22μm and the effect of compressive stress.

As the radii of membranes decrease, the effect of compressive stress decreases. Figure 3.9 shows the relation between compressive stress and membrane deflection for CMUTs with five different sizes.

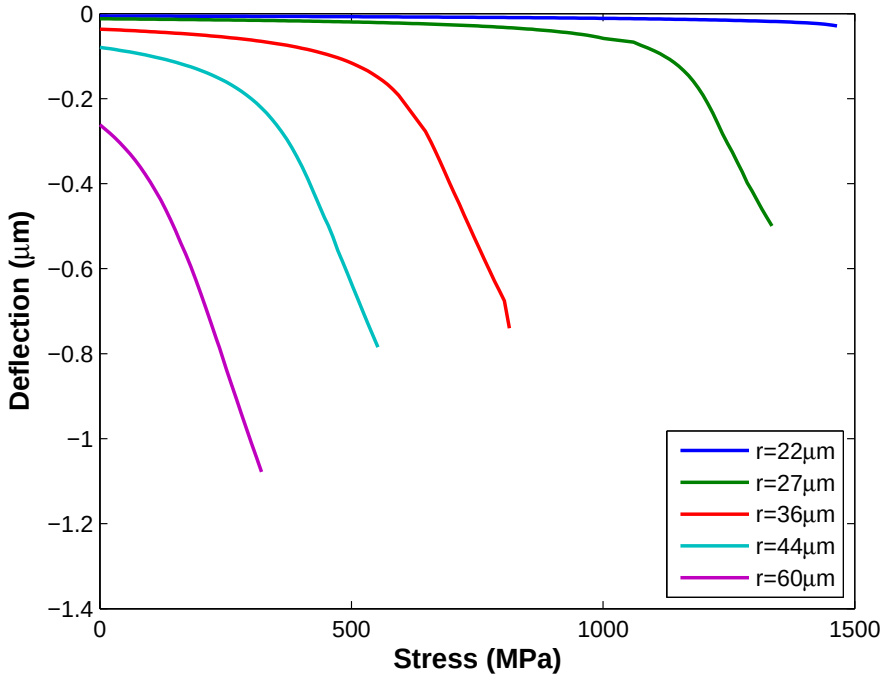

Figure 3.9: Deflection versus Compressive Stress for CMUTs with different radii

For small radii, compressive stress is not effective. However, compressive stress should be avoided for circular CMUTs with high radii.

3.3.2 Stress Analysis

Stress is a measure of material response to external forces. This can be caused by pressure on the membrane due to environmental conditions, electrostatic forces due to bias voltages or manufacturing processes for a CMUT. It is an important factor which effects the behaviour of a transducer. Therefore, in finite element analysis, an exact model needs to consider the stress distribution on the structure.

Basic schematic of the CMUT was given in Figure 3.1. There exist a vacuum region inside

the CMUT sealed with diamond membrane bonded on the oxide layer through the high temperature oxide grown on the diamond. Since membrane thickness is not high when compared to radius, deflection occurs under atmospheric pressure although diamond is a special material with high Young's Modulus and extreme hardness. A steady-state structural analysis is performed to obtain stress values and distribution on the nodes. Atmospheric pressure, as the static load, is applied on the membrane and electrode surface. Air deflection for various sized CMUTs were given in Table 3.2. Static structural stress analyses results are given in Figures 3.10, 3.11, 3.12, 3.13 and 3.14 for CMUTs with radii 60 μm, 44 μm, 36 μm, 27 μm and 22 μm respectively.

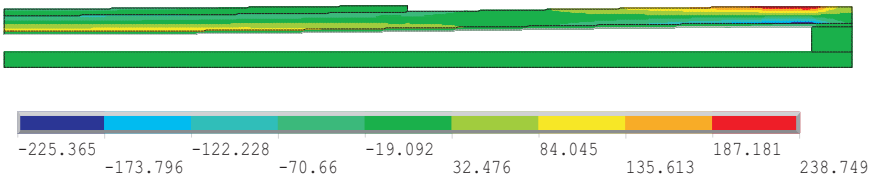

Figure 3.10: Stress distribution on the CMUT membrane due to atmospheric pressure. Stress value unit is MPa. CMUT radius is 60 μm and atmospheric pressure is 0.1 MPa.

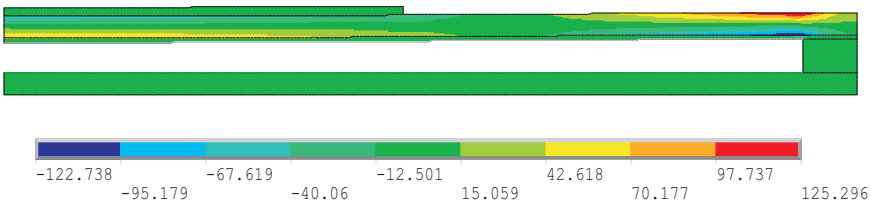

Figure 3.11: Stress distribution on the CMUT membrane due to atmospheric pressure. Stress value unit is MPa. CMUT radius is 44 μm and atmospheric pressure is 0.1 MPa.

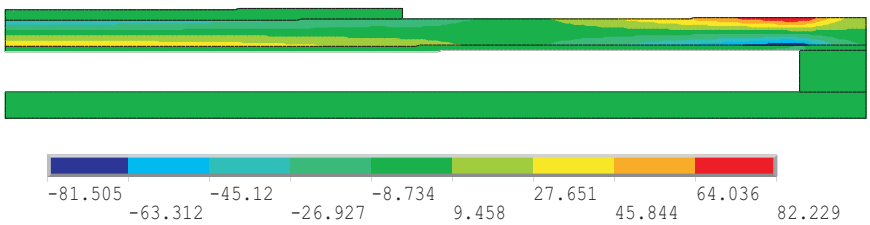

Figure 3.12: Stress distribution on the CMUT membrane due to atmospheric pressure. Stress value unit is MPa. CMUT radius is 36 μm and atmospheric pressure is 0.1 MPa.

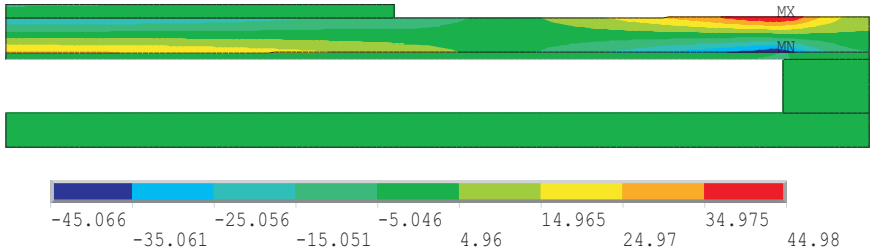

Figure 3.13: Stress distribution on the CMUT membrane due to atmospheric pressure. Stress value unit is MPa. CMUT radius is 27 μm and atmospheric pressure is 0.1 MPa.

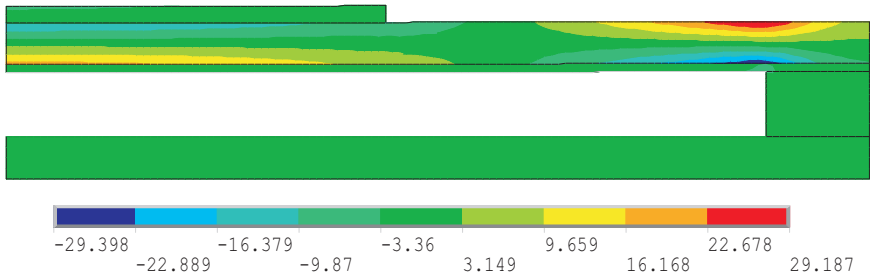

Figure 3.14: Stress distribution on the CMUT membrane due to atmospheric pressure. Stress value unit is MPa. CMUT radius is 22 μm and atmospheric pressure is 0.1 MPa.

It is obvious that stress types are compressive at the central regions of membranes and tensile at membrane edges which are clamped on oxide supports. Maximum compressive stress values increase as the CMUT radii increase as expected. The stress values are proportional with the deflection values of diamond membranes.

3.3.3 Electrostatic Analysis

An analysis to find the displacements caused by electrostatic forces, a coupled electrostatic-structural analysis is performed. Electrostatic-structural coupling involves the coupling of electrostatic forces with the mechanical response of the structure. This type of simulation is occasionally used for MEMS devices such as CMUTs, comb drives, torsional mirrors and accelerometers [30]. Collapse-snapback voltages are calculated utilizing this analysis.

Insulating Membrane

Capacitive micromachined ultrasonic transducers (CMUTs) are used either in transmit mode or in receive mode. In transmit mode, the movement of membrane creates ultrasonic waves in air or in immersion. In receive mode, acoustic pressure applied on the membrane surface is converted to electrical signal with its capacitive structure.

In a typical application, CMUT is biased with DC voltage and an AC signal. These signals are applied between the top electrode on the membrane and the highly doped substrate [Figure 3.15]. DC bias voltage creates an electrostatic force on the membrane causing it to collapse towards the substrate surface. Increasing DC bias causes the membrane bending to increase. At a specific DC voltage value, membrane is collapsed totally. This value is named as collapse voltage.

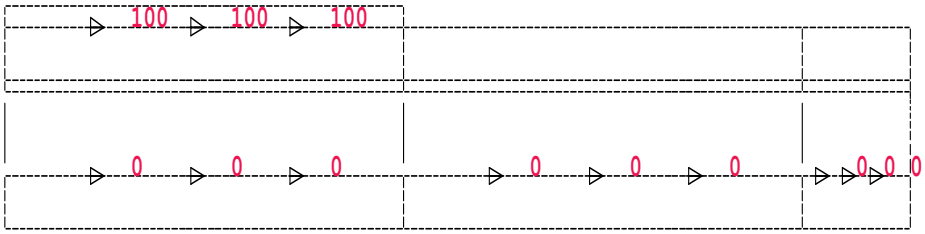

Figure 3.15: DC bias voltage is applied between the top electrode on the membrane and the highly doped substrate. The values in red color show voltage levels. 100 V appears on the bottom surface of the top electrode and ground connection is represented with 0 V which appears on the top surface of the substrate.

Collapse voltage is dependent on CMUT structural dimensions as well as the material properties. Since it is more efficient to operate a CMUT close to its collapse voltage [16], it is crucial to find this value accurately.

When a DC voltage is applied, electrostatic force is created on the diamond membrane surface. This force causes the membrane to bend through the substrate. The deflection of membrane, then, causes the electrostatic force to change. This cycle continues until an equilibrium is reached. Coupled electrostatic-structural analysis is performed in ANSYS to solve collapse voltage problem. ESSOLV macro of ANSYS solves this cycle iteratively and continues until a defined convergence value is reached.

At total collapse, membrane touches the substrate. Decreasing the DC bias voltage does not

helps the membrane to snap back abruptly. There exist an hysteresis effect.

Several simulations have been performed for different CMUT sizes and membrane-substrate distances (i.e. net gap) to characterize the operational value of collapse voltage. Figures 3.16, 3.17, 3.18, 3.19 and 3.20 show the relationship between net gap and collapse-snapback voltages for CMUTs with radii 60 μm, 44 μm, 36 μm, 27 μm and 22 μm respectively. Net gaps are the minimum membrane-substrate distances, which occur at the center of circular CMUT and includes air deflection effect caused by atmospheric pressure and compressive stress if exists. In the mentioned figures, compressive stress values are zero and atmospheric pressure values are 0.1 MPa.

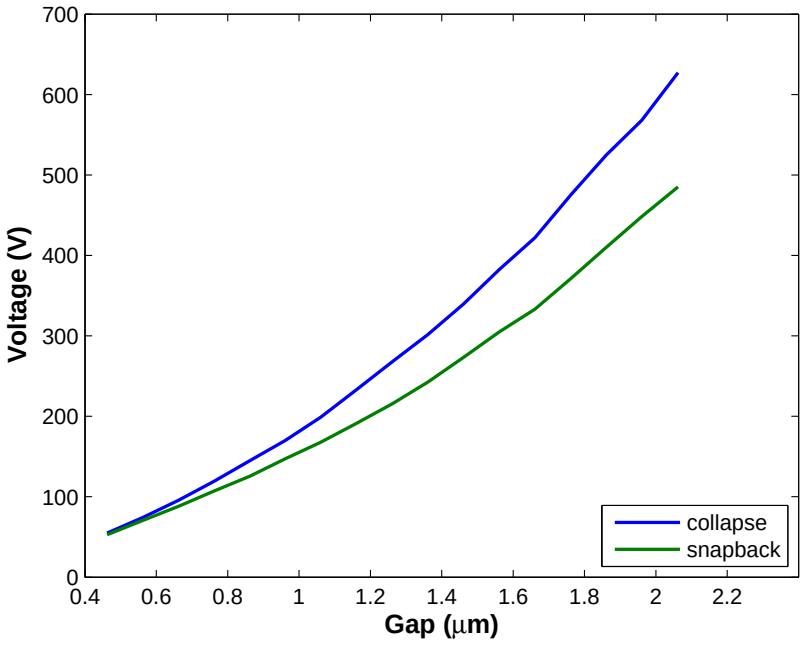

Figure 3.16: The relationship between net gap and collapse-snapback voltage under atmospheric pressure of 0.1 MPa. Residual compressive stress is ignored. Membrane size is 60 μm.

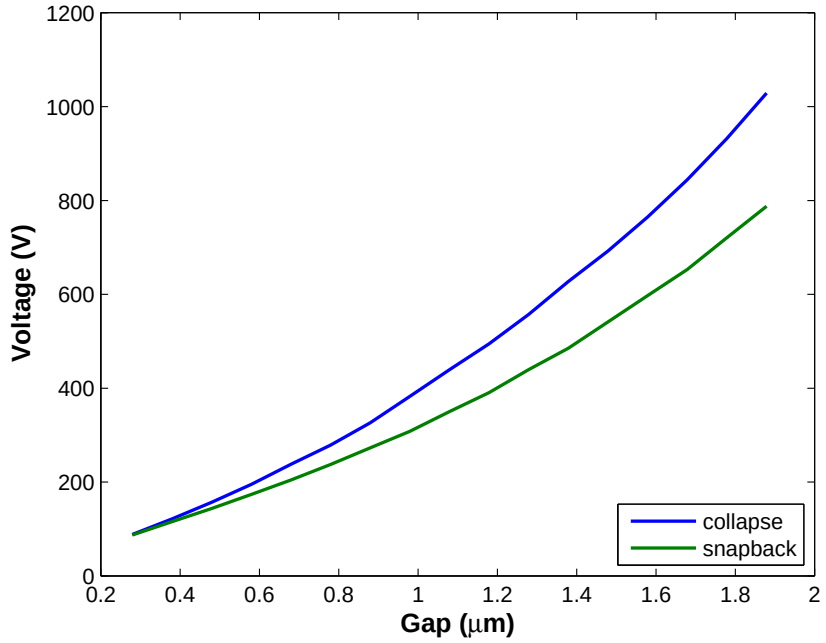

Figure 3.17: The relationship between net gap and collapse-snapback voltage under atmospheric pressure of 0.1 MPa. Residual compressive stress is ignored. Membrane size is 44 μm.

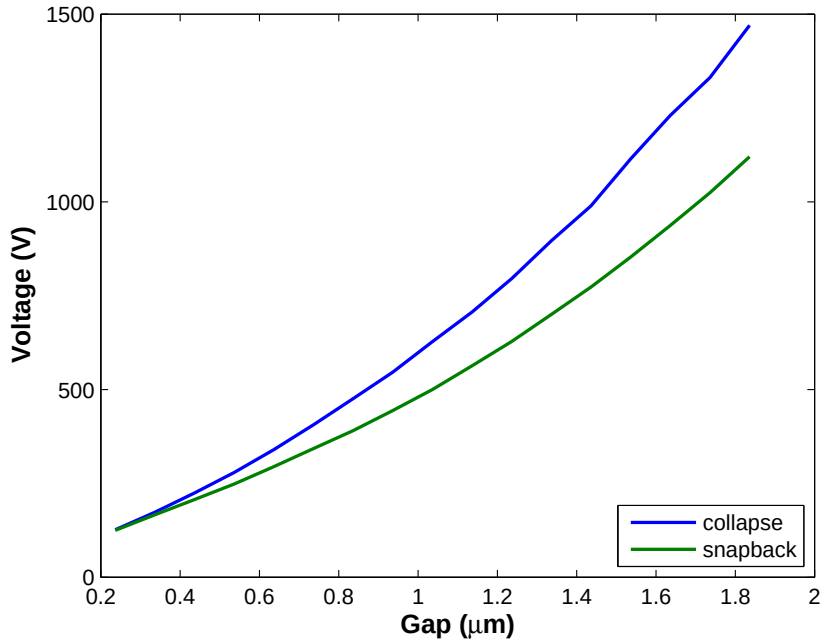

Figure 3.18: The relationship between net gap and collapse-snapback voltage under atmospheric pressure of 0.1 MPa. Residual compressive stress is ignored. Membrane size is 36 μm.

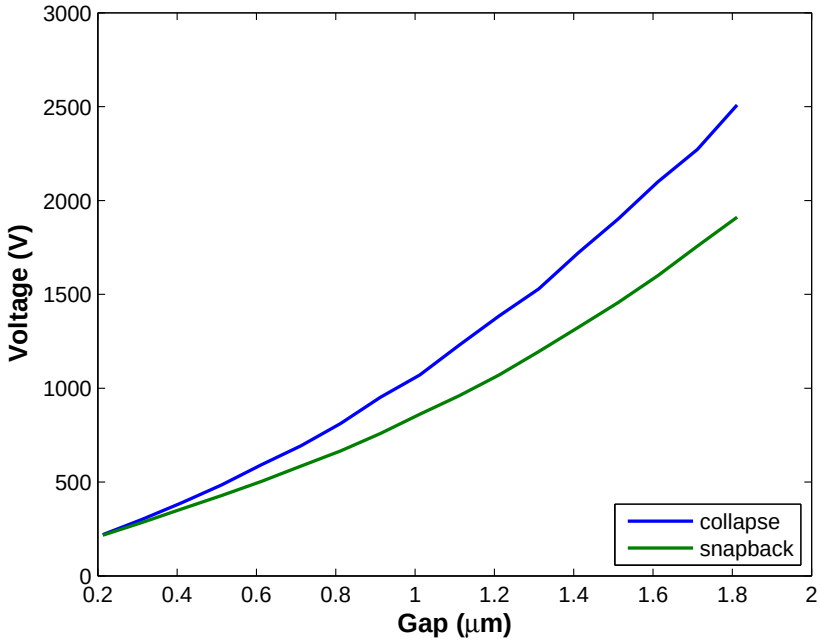

Figure 3.19: The relationship between net gap and collapse-snapback voltage under atmospheric pressure of 0.1 MPa. Residual compressive stress is ignored. Membrane size is 27 μm.

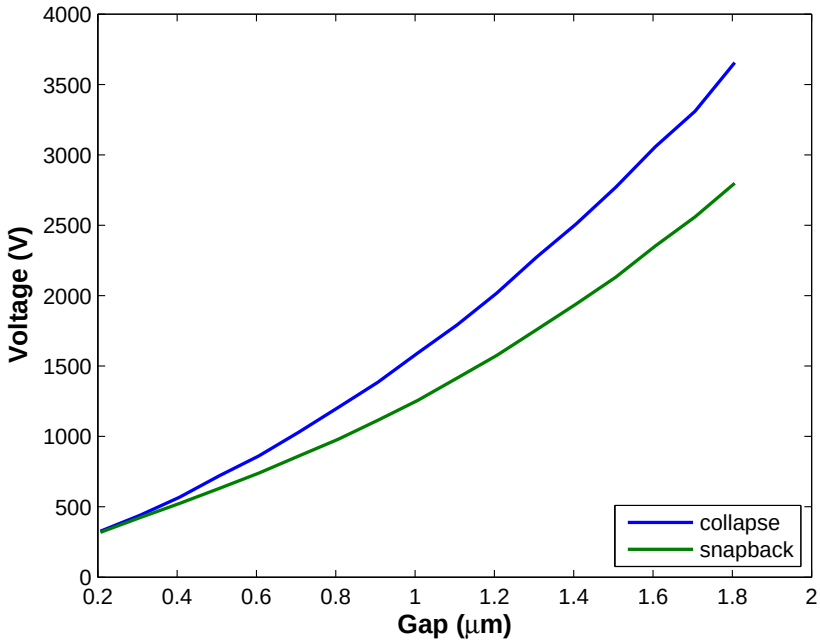

Figure 3.20: The relationship between net gap and collapse-snapback voltage under atmospheric pressure of 0.1 MPa. Residual compressive stress is ignored. Membrane size is 22 μm.

Figure 3.21 shows the relationship between the maximum displacement and applied DC bias voltage under atmospheric pressure of 0.1 MPa. Residual compressive stress is ignored in this simulation. While the voltage increases with a step size of %2, the slope also increases. Decreasing distance between the membrane and the substrate causes the electrostatic force to increase in a non-linear behaviour [Equation (2.12)]. Although Equation (2.9) states a higher distance where the collapse occurs for a piston shaped membrane, bending effect on the membrane causes lower distances available.

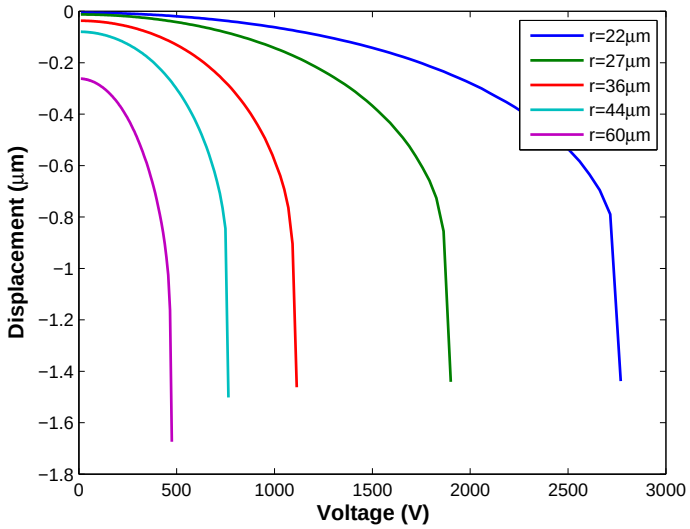

Figure 3.21: The relationship between the maximum displacement and applied DC bias voltage under atmospheric pressure of 0.1 MPa. Residual compressive stress is ignored. Net gap is 1.5 μm for all CMUTs.

Figure 3.22 shows the relationship between the capacitance and applied DC bias voltage. It is obvious that capacitance change is minimum for the CMUT with the smallest radius. Each point on the membrane has a specific displacement value which can be calculated with Equation (2.14). As the membrane radius increases deviation of nodal displaments increase, which means that membrane curvature also increases.

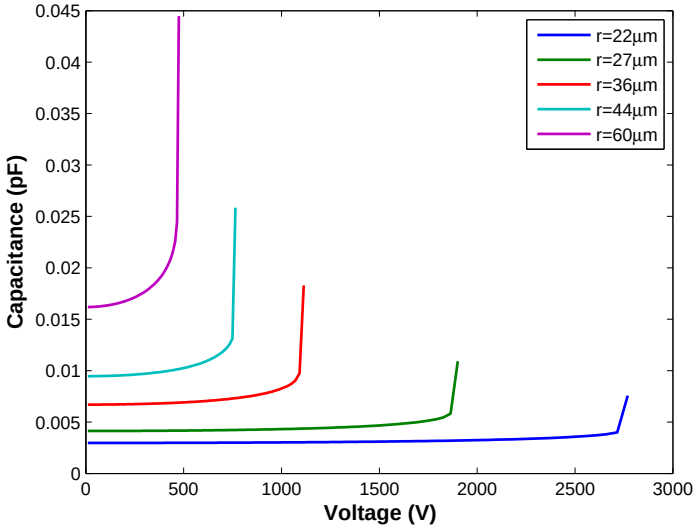

Figure 3.22: The relationship between the capacitance and applied DC bias voltage under atmospheric pressure of 0.1 MPa. Residual compressive stress is ignored. Net gap is 1.5 μm for all CMUTs.

The relationship between the DC bias voltage and electrical energy stored on the capacitor is given in Figure 3.23.

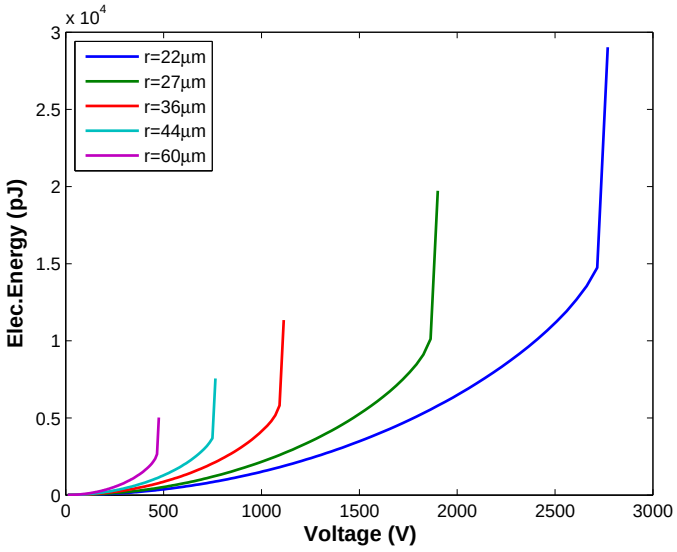

Figure 3.23: The relationship between the electrical energy and applied DC bias voltage under atmospheric pressure of 0.1 MPa. Residual compressive stress is ignored. Net gap is 1.5 μm for all CMUTs.

The relationship between the DC bias voltage and mechanical energy stored on the capacitor is given in Figure 3.24.

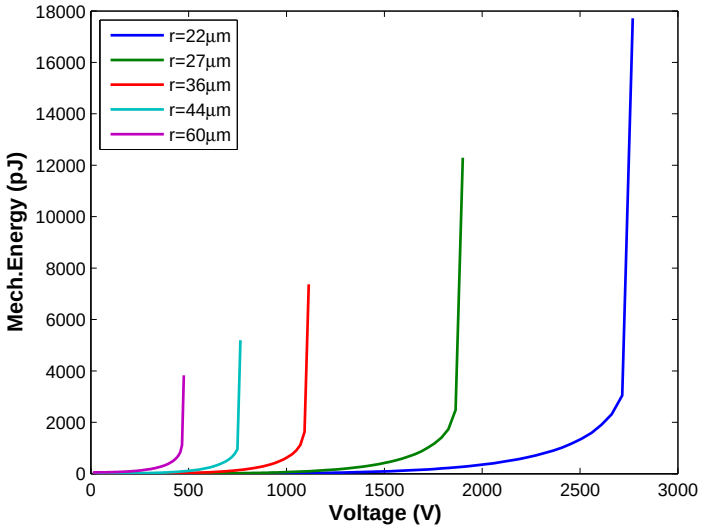

Figure 3.24: The relationship between the mechanical energy and applied DC bias voltage under atmospheric pressure of 0.1 MPa. Residual compressive stress is ignored. Net gap is 1.5 μm for all CMUTs.

Although diamond is a hard material and resistant in collapse-snapback operation, the voltage levels to operate diamond-based CMUTs in this mode are very high. Table 3.3 provides the collapse-snapback voltages for an insulating diamond used as a membrane.

Table 3.3: The relationship between Collapse/Snapback voltages and net gap under atmospheric pressure of 0.1 MPa for different CMUT sizes. Residual compressive stress is ignored.

Net Gap (μm)	6 0 μm		44 μm		36 μm		27 μm		22 μm	
	Collapse (V)	Snapback (V)	Collapse (V)	Snapback (V)	Collapse (V)	Snapback (V)	Collapse (V)	Snapback (V)	Collapse (V)	Snapback (V)
0.2	54.91	52.76	88.31	86.93	126.1	125.1	219.6	216.2	326.3	318.7
0.3	73.9	70.43	121.2	115.6	173.2	166.4	301.5	285	439.2	422
0.4	95.59	88.12	156.8	143.4	224	206.5	390	356.5	568.1	523.7
0.5	118.9	106.8	195	173.7	278.5	248	484.9	428.1	720.5	630.4
0.6	144.9	125.6	237.7	204.3	339.5	294.4	591.1	503.3	861.1	740
0.7	169.8	147.2	278.5	237.2	405.7	342.3	692.5	584.3	1029	860.2
0.8	198.9	167.8	326.3	272.8	475.4	390	811.4	665.6	1206	979.6
0.9	233	191.2	382.3	307.7	546.1	443.7	950.7	757.6	1385	1114
1.0	267.7	215.4	439.2	350	627.2	499.8	1071	861.5	1591	1255
1.1	301.5	242.6	494.6	390.3	706.4	562.9	1230	960.8	1792	1414
1.2	339.5	273.2	557	439.5	795.5	627.7	1385	1071	2018	1576
1.3	382.3	304.7	627.2	485.1	895.9	699.9	1529	1195	2272	1757
1.4	422.1	333.1	692.5	541	989.1	772.7	1722	1325	2509	1940
1.5	475.4	371.4	764.6	597.3	1114	852.8	1901	1456	2770	2131
1.6	524.8	410	844.2	652.9	1230	936.8	2099	1599	3058	2353
1.7	568.1	448.3	932.1	720.9	1331	1024	2272	1757	3310	2560
1.8	627.2	485.1	1029	787.9	1470	1120	2509	1911	3655	2798

Conducting Membrane

Although natural diamond is an insulating material, ULTRANANOCRYSTALLINE diamond (UNCD) which is grown on silicon wafer can have lower resistivity values under different circumstances applied during the process. In this case, the voltage applied to electrode on the membrane appear below the membrane [Figure 3.25].

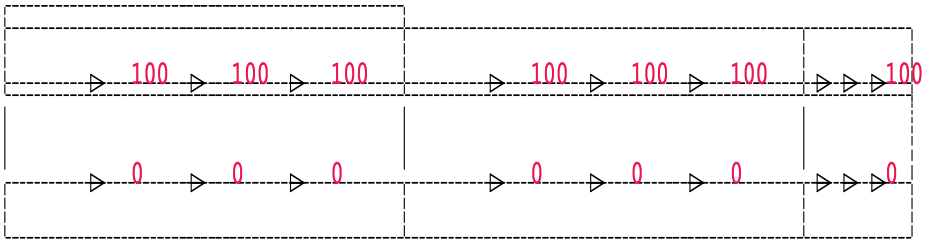

Figure 3.25: DC bias voltage is between the top electrode on the membrane and the highly doped substrate. The values in red color show voltage levels. 100 V appears on the bottom surface of the diamond membrane since it is conducting and ground connection is represented with 0 V which appears on the top surface of the substrate.

Since the effective gap [Equation (2.13)] is decreased with a conducting membrane, lower bias voltage causes the membrane to collapse. Figures 3.26, 3.27, 3.28, 3.29 and 3.30 show the relationship between net gap and collapse-snapback voltages for CMUTs with radiuses 60 μm, 44 μm, 36 μm, 27 μm and 22 μm respectively. It is obvious that collapse voltages of CMUTs with conducting membranes are much lower than the collapse voltages of CMUTs with insulating diamond membranes.

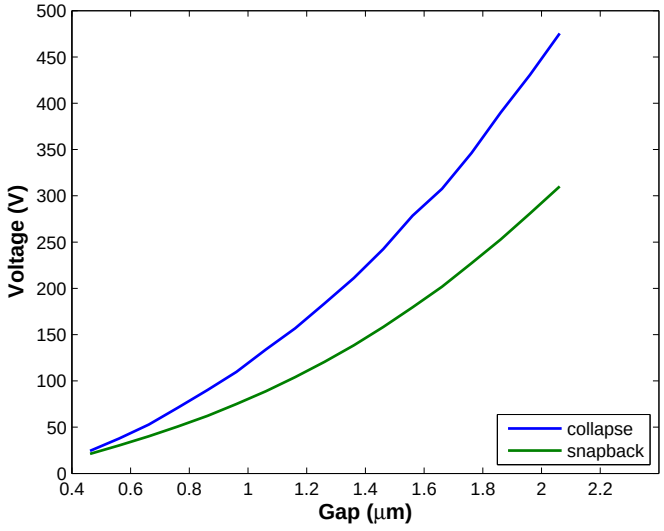

Figure 3.26: The relationship between net gap and collapse-snapback voltage under atmospheric pressure of 0.1 MPa. Residual compressive stress is ignored. Membrane radius is 60 μm.

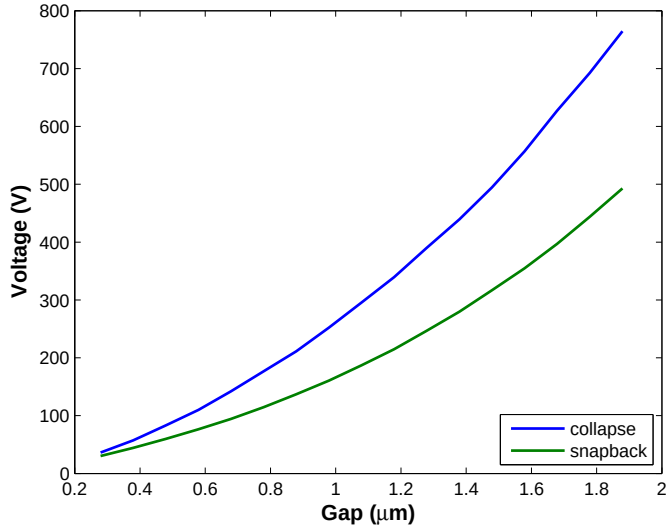

Figure 3.27: The relationship between net gap and collapse-snapback voltage under atmospheric pressure of 0.1 MPa. Residual compressive stress is ignored. Membrane radius is 44 μm.

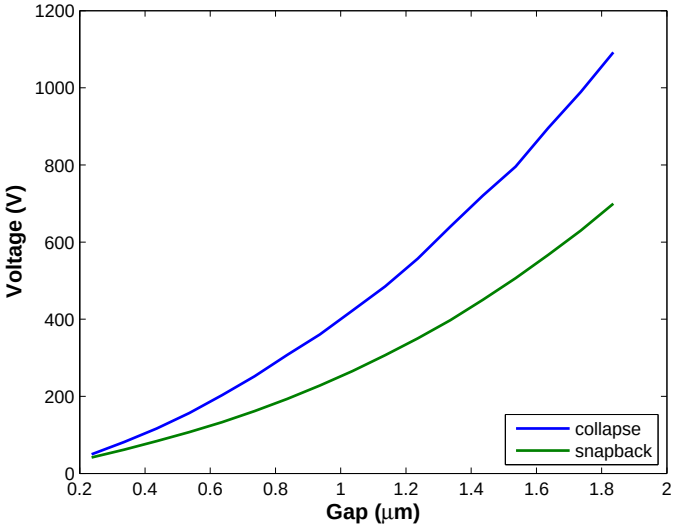

Figure 3.28: The relationship between net gap and collapse-snapback voltage under atmospheric pressure of 0.1 MPa. Residual compressive stress is ignored. Membrane radius is 36 μm.

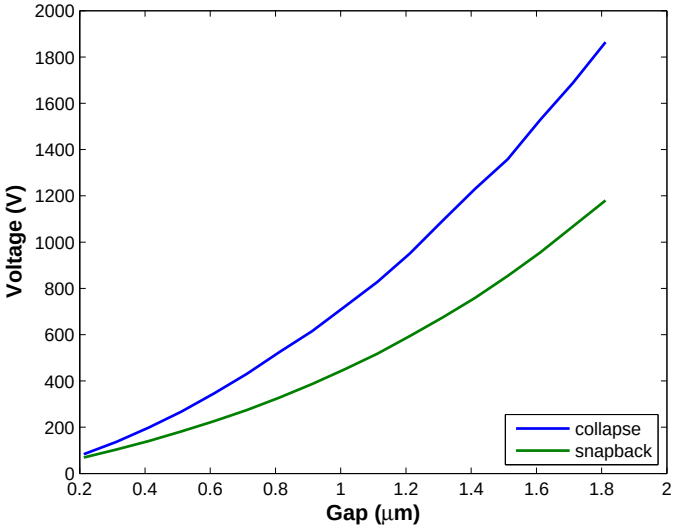

Figure 3.29: The relationship between net gap and collapse-snapback voltage under atmospheric pressure of 0.1 MPa. Residual compressive stress is ignored. Membrane radius is 27 μm.

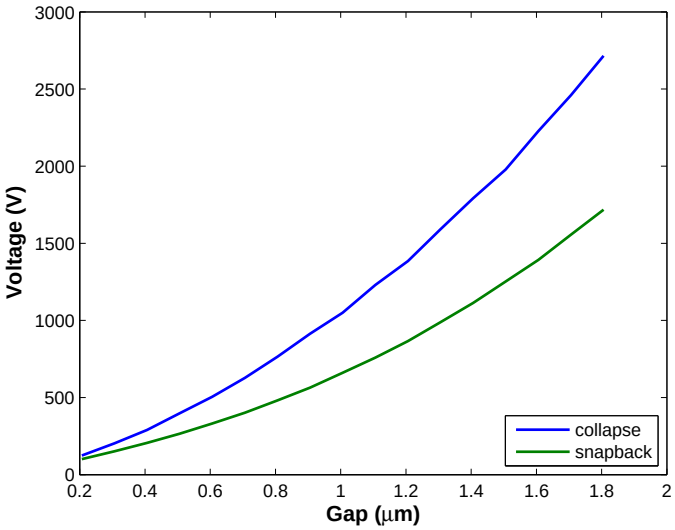

Figure 3.30: The relationship between net gap and collapse-snapback voltage under atmospheric pressure of 0.1 MPa. Residual compressive stress is ignored. Membrane radius is 22 μm.

The maximum displacement changes with the varying bias voltage [Figure 3.31]. Figure 3.32 shows the relationship between capacitance and bias voltage. Electrical energy and mechan-

ical energy changes with varying bias voltages as indicated in the insulating membrane case [Figures 3.33 and 3.34 respectively].

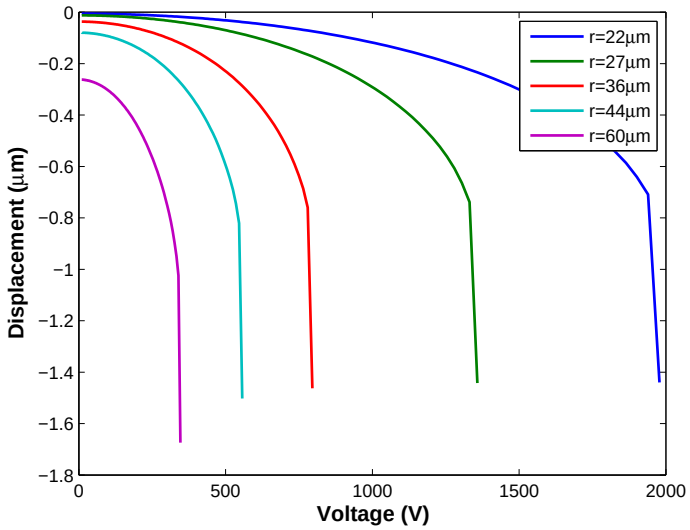

Figure 3.31: The relationship between the maximum displacement and applied DC bias voltage under atmospheric pressure of 0.1 MPa. Residual compressive stress is ignored. Net gap is 1.5 μm for all CMUTs.

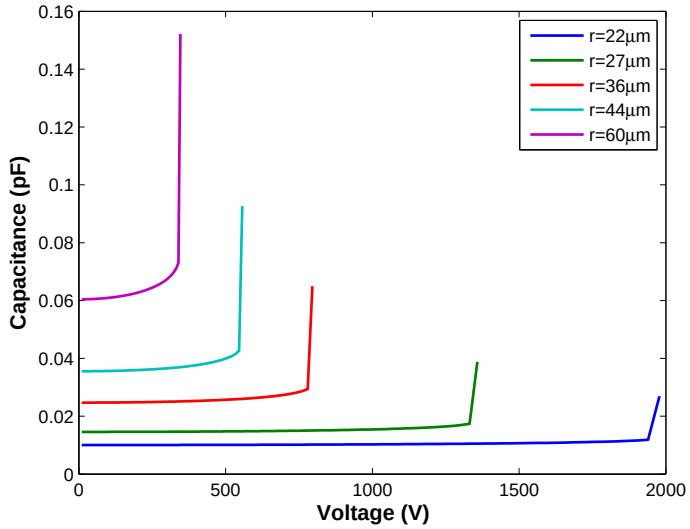

Figure 3.32: The relationship between the capacitance and applied DC bias voltage under atmospheric pressure of 0.1 MPa. Residual compressive stress is ignored. Net gap is 1.5 μm for all CMUTs.

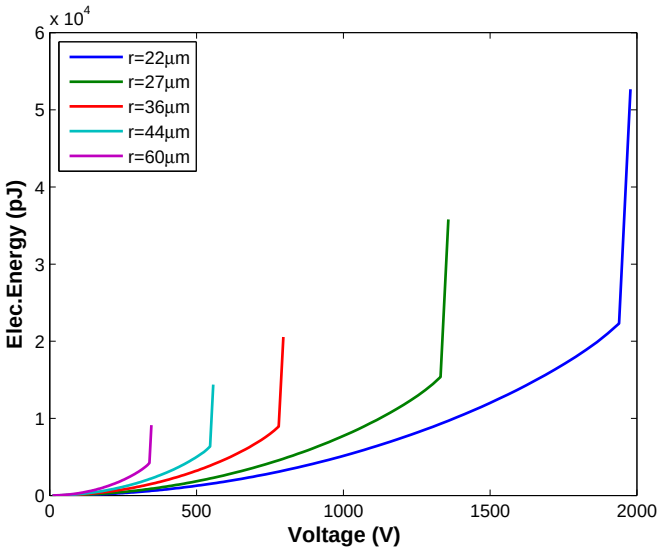

Figure 3.33: The relationship between the electrical energy and applied DC bias voltage under atmospheric pressure of 0.1 MPa. Residual compressive stress is ignored. Net gap is 1.5 μm for all CMUTs.

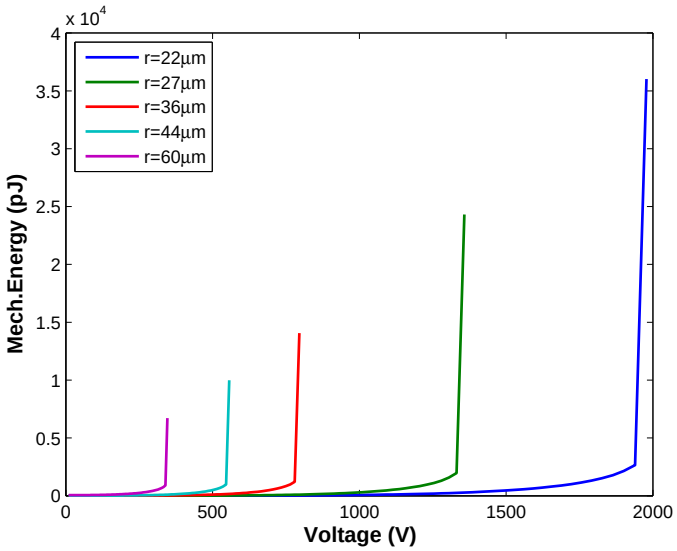

Figure 3.34: The relationship between the mechanical energy and applied DC bias voltage under atmospheric pressure of 0.1 MPa. Residual compressive stress is ignored. Net gap is 1.5 μm for all CMUTs.

Table 3.4 gives the collapse-snapback voltages for five different CMUT sizes with varying net gaps. All the values in this table are obtained for diamond-based CMUT without any residual

stress. When there exist a residual compressive stress in a diamond membrane, collapse-snapback voltages decrease. This is due to increased bending of membrane caused by compressive stress. Table 3.5 provides the obtained values with the analysis of CMUT with initial stress.

Table 3.4: The relationship between Collapse/Snapback voltages and net gap under atmospheric pressure of 0.1 MPa for different CMUT sizes. Residual compressive stress is ignored.

Net Gap (μm)	6 0 μm		44 μm		36 μm		27 μm		22 μm	
	Collapse (V)	Snapback (V)	Collapse (V)	Snapback (V)	Collapse (V)	Snapback (V)	Collapse (V)	Snapback (V)	Collapse (V)	Snapback (V)
0.2	24.38	21.14	36.23	30.28	49.73	41.57	83.22	68.92	123.7	100.5
0.3	37.69	30.33	57.12	44.18	81.59	61.83	136.5	103.5	202.9	151.4
0.4	52.77	40.2	83.22	59.81	116.5	83.75	198.9	140.6	289.8	206
0.5	71.03	50.77	109.8	76.35	156.8	107.2	267.7	181.9	397.8	265.7
0.6	90.08	62.28	142	94.33	202.9	133.1	346.3	225.9	504.5	331.1
0.7	109.8	75.06	176.6	114.5	252.2	161.6	430.6	274.1	627.2	401.8
0.8	133.9	88.89	211.1	136.9	307.5	193.4	524.8	328	764.6	480.9
0.9	156.8	104.1	252.2	160.6	360.3	228	614.9	386.7	913.8	564
1.0	183.7	120.6	295.5	187	422.1	265.5	720.5	450.3	1050	660.1
1.1	211.1	138.5	339.5	214.8	484.9	306.8	827.6	517.3	1230	759
1.2	242.5	158.2	390	246.8	557	350.3	950.7	594.2	1385	865.6
1.3	278.5	179.5	439.2	279.6	639.8	397.4	1092	674	1591	988.1
1.4	307.5	201.8	494.6	316.8	720.5	450.3	1230	759	1792	1113
1.5	346.3	227.2	557	354.6	795.5	506.5	1358	853.9	1978	1252
1.6	390	252.9	627.2	396.9	895.9	566.9	1529	955.7	2228	1392
1.7	430.6	280.9	692.5	443.7	989.1	629.8	1688	1068	2460	1556
1.8	475.4	310.1	764.6	492.8	1092	699.6	1864	1180	2715	1718

Table 3.5: The relationship between Collapse/Snapback voltages and net gap under atmospheric pressure of 0.1 MPa for different CMUT sizes. Residual compressive stress of 200 MPa is included.

Net Gap (μm)	6 0 μm		44 μm		36 μm		27 μm		22 μm	
	Collapse (V)	Snapback (V)	Collapse (V)	Snapback (V)	Collapse (V)	Snapback (V)	Collapse (V)	Snapback (V)	Collapse (V)	Snapback (V)
0.2	<10	<10	22.08	19.84	40.00	34.06	76.88	63.07	116.50	95.59
0.3	<10	<10	38.44	30.93	66.93	51.50	126.10	94.60	191.20	142.60
0.4	<10	<10	57.12	43.29	97.50	70.08	183.70	129.20	278.50	194.70
0.5	11.95	9.90	78.42	56.67	131.20	90.73	247.30	167.10	374.80	251.80
0.6	28	22.53	103.50	71.14	169.80	113.40	319.90	208.70	475.40	313.80
0.7	42.44	34.49	131.20	88.17	211.10	139.30	397.80	254.80	591.10	383.30
0.8	59.43	46.89	160.00	107.50	257.30	167.80	475.40	304.50	720.50	458.80
0.9	78.42	60.34	195.00	128.70	307.50	199.40	568.10	359.50	861.10	538.20
1.0	99.45	75.37	228.50	152.60	367.50	234.00	665.60	421.20	1009.00	626.60
1.1	123.7	91.29	267.70	178.80	422.10	270.40	779.90	487.40	1159.00	724.30
1.2	147.8	108.50	313.60	207.10	484.90	312.50	895.90	559.90	1331.00	832.00
1.3	176.6	128.30	360.30	239.20	557.00	359.00	1009.00	638.40	1499.00	948.70
1.4	206.9	149.50	405.70	272.60	627.20	406.70	1136.00	723.40	1688.00	1075.00
1.5	237.7	172.70	466.00	309.50	706.40	460.80	1280.00	814.70	1901.00	1203.00
1.6	273.0	196.20	524.80	348.50	795.50	518.90	1413.00	910.50	2141.00	1355.00
1.7	313.6	223.00	579.50	391.60	878.30	579.80	1591.00	1019.00	2364.00	1505.00
1.8	353.2	249.70	652.60	435.90	989.10	645.20	1756.00	1132.00	2610.00	1672.00

3.4 Frequency Analysis

Specifying the resonant frequencies for CMUTs is very important to operate them with maximum efficiency. Harmonic simulations of diamond membrane based CMUTs are performed with Finite Element Analysis using ANSYS. Each analysis is defined as a system and can be used to create integrated schemes. A pre-stress analysis is performed and the output of

this analysis is used as input of modal analysis to find the resonance frequencies. Material properties were given in Table 3.1.

3.4.1 Modal Analysis

In a CMUT design, determining the operational frequencies is crucial. Each CMUT is designed to generate highest acoustic energy with maximum efficiency at the required operating frequency. A CMUT creates maximum mechanical energy at its natural frequencies. The basic approach to find the natural frequencies is to perform modal analysis. Modal analysis is the starting point of dynamic analysis (e.g. dynamic transient analysis, harmonic response analysis or spectrum analysis) [30]. The result of this analysis shows also the shape of the structure at its natural frequencies.

When a dynamic load is applied on the membrane of CMUT, the response will be dynamic. Such an operational regime requires that CMUT will perform the desired response. ANSYS allows a modal analysis to be run on the structure. The modal analysis of ANSYS is linear which means that any nonlinear properties are ignored even they are defined. There exists several methods to extract mode frequencies. Block Lanczos, Supernode, PCG Lanczos, reduced and unsymmetric methods are some of these [30].

If the modal analysis is performed in an undamped situation, ANSYS solves the following equation in modal analysis [30]:

$$[K]\{\phi_i\} = \omega_i^2[M]\{\phi_i\} \tag{3.1}$$

where [K] is stiffness matrix, $\{\phi_i\}$ is mode shape vector (eigenvector) of mode, ω_i^2 is the natural frequency of mode and [M] is the mass matrix.

When only few modes are required and 3D-solid elements are used in a large model, PCG Lanczos method solves the problem faster with Lanczos algorithm. This method allows to find only the lowest eigenvalues. Although a frequency range in the spectrum can be defined to find the mode frequencies, it is not recommended when the lowest mode frequency is much greater than zero [30].

While PCG Lanczos is useful to find few modes of very large models, Block Lanczos method allows to find many modes of a structure. Block Lanczos method also utilizes Lanczos algorithm. If it is required to find the eigenvalues in a given spectrum range, this method performs best. The eigenvalues are extracted with the same speed either in the lower range of the spectrum or in the higher range of the spectrum. However Block Lanczos method requires high disk capacity.

Supernode and Reduced methods also give the modes with less disk space and memory. In modal analysis of CMUTs with diamond membranes, the model in Figure 3.2 is used with Block Lanczos method to obtain the first 6 mode frequencies. Young's modulus, Poisson's ratio and density properties are introduced for the stuctural elements.

The first analysis was to find the relationship between the natural frequencies and anchor height (i.e. defined with the distance between the substrate and the membrane). Table 3.6 gives the results of this analysis.

Table 3.6: Relationship between anchor rigidity and resonant frequencies for CMUT with radius 60 μm.

Net Gap (µm)	Mode 1 (MHz)	Mode 2 (MHz)	Mode 3 (MHz)	Mode 4 (MHz)	Mode 5 (MHz)	Mode 6 (MHz)
0.2	1.85	7.54	16.8	29.8	46.2	66.3
0.3	1.85	7.53	16.8	29.8	46.2	66.2
0.4	1.85	7.52	16.7	29.7	46.1	66.1
0.5	1.84	7.51	16.7	29.7	46.1	66.1
0.6	1.84	7.51	16.7	29.7	46.0	66.0
0.7	1.84	7.50	16.7	29.7	46.0	66.0
0.8	1.84	7.50	16.7	29.6	46.0	65.9
0.9	1.84	7.49	16.7	29.6	45.9	65.9
1.0	1.84	7.49	16.7	29.6	45.9	65.9
1.1	1.84	7.49	16.7	29.6	45.9	65.8
1.2	1.84	7.48	16.7	29.6	45.9	65.8
1.3	1.84	7.48	16.7	29.6	45.9	65.8
1.4	1.84	7.48	16.7	29.6	45.9	65.8
1.5	1.84	7.48	16.7	29.6	45.8	65.8
1.6	1.84	7.48	16.7	29.6	45.8	65.7
1.7	1.84	7.48	16.7	29.6	45.8	65.7
1.8	1.84	7.48	16.7	29.6	45.8	65.7

The analysis is performed for a single CMUT with a radius of 60 μm. The values in the table show that frequency change with the net gap is very low for the first mode. However for higher modes at higher frequencies are affected more. As the net gap increases, the natural frequency tends to decrease.

The modal analysis is performed for CMUTs with radii 60 μm, 44 μm, 36 μm, 27 μm and 22 μm. The results for 3 different gap values are shown in Table 3.7.

Table 3.7: Relationship between gap and resonant frequencies for different CMUT sizes

Net Gap (µm)	Frequency (MHz)				
	60-µm	44-µm	36-µm	27-µm	22-µm
0.5	1.84	3.38	4.99	8.69	12.84
1	1.83	3.37	4.97	8.64	12.75
1.5	1.83	3.36	4.96	8.61	12.70

The values in Table 3.7 indicate that natural frequencies are inversely proportional with CMUT radii. Only first mode frequencies are shown.

Figure 3.35 shows the mode shapes of the structure caused by dynamic loads. Since the substrate thicknes is much greater than membrane thickness, degree of freedom in vertical direction for the substrate is constrained to zero. Since a real circular CMUT is composed of several single cells [Figure 3.1], degree of freedom in the horizontal direction is also set to zero for the whole structure. Only the membrane moves due to applied loads. Maximum total displacement in one direction is obtained in the first mode. This means maximum pressure can be obtained in the first mode only.

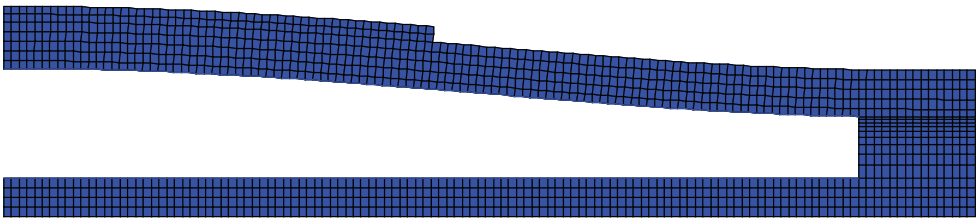

(a) Deflected membrane shape when natural frequency is at Mode 1

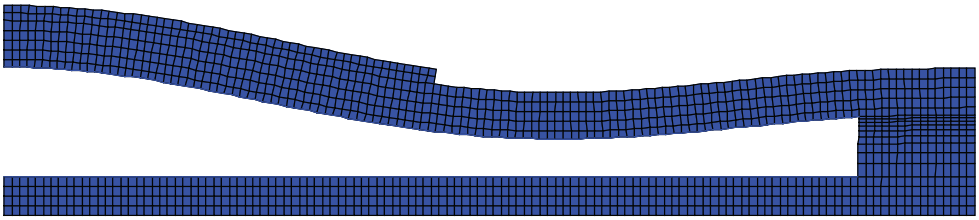

(b) Deflected membrane shape when natural frequency is at Mode 2

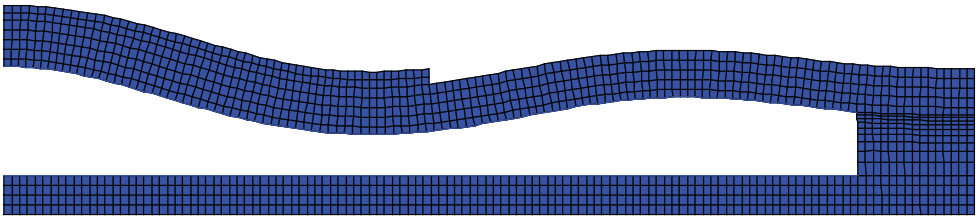

(c) Deflected membrane shape when natural frequency is at Mode 3

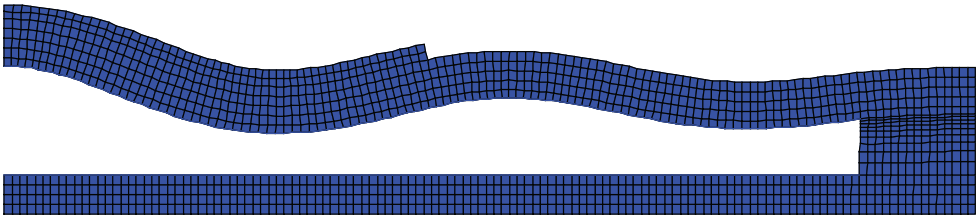

(d) Deflected membrane shape when natural frequency is at Mode 4

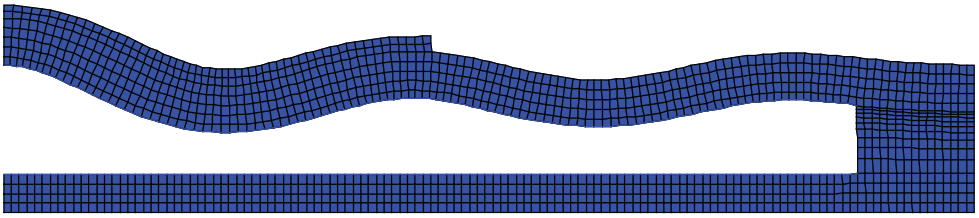

(e) Deflected membrane shape when natural frequency is at Mode 5

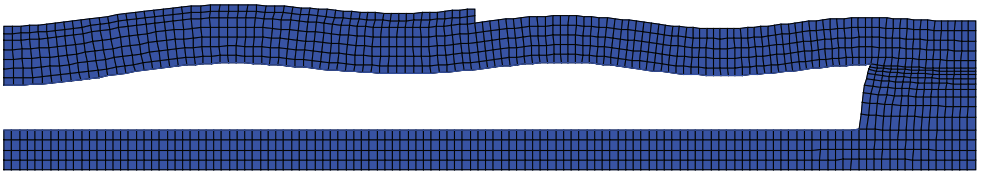

(f) Deflected membrane shape when natural frequency is at Mode 6

Figure 3.35: Mode shapes for a capacitive micromachined

A more realistic case is to perform the modal analysis for prestressed CMUTs. Since the atmospheric pressure causes deflection on the membrane shape, stress related with CMUT radius occurs on the membrane. ANSYS allows a prestressed modal analysis to be performed on a structure. The difference between a regular modal analysis and prestressed modal analysis in terms of procedure is the requirement of a static analysis just before the start of modal analysis. The static analysis is performed with "'PSTRES ON"' command under a static load and the stress values are calculated. Then, modal analysis as the solution type is set with "'ANTYPE,MODAL"' command and solution procedure is started. It is not allowed to perform any other analysis between prestress analysis and modal analysis. If it is performed, it is required to repeat prestress analysis.

A challenge in modal analysis is to include the large deflection effects in the analysis. If the membrane deformation caused by a static load is significantly different from the original profile, this is called large deflection. Not every analysis type can be performed with this effect in ON state. However Ansys allows to perform modal analysis with this using "'NLGEOM,ON"' command. "'PSOLVE"' command is required instead of classical "'SOLVE"' command to start solution when large deflection occurs after static analysis.

Table 3.8 shows the results of prestressed modal analysis for CMUTs with various sizes and net gaps.

Table 3.8: Relationship between gap and resonant frequencies for different CMUT sizes. Stress distribution due to atmospheric pressure is included.

Net Gap (μm)	Frequency (MHz)				
	60-μm	44-μm	36-μm	27-μm	22-μm
1.5	1.98	3.67	5.34	9.34	13.6

According to the results, natural frequencies increase when the membrane is exposed to stress caused by static loads (e.g. air pressure, electrostatic forces).

3.4.2 Harmonic Analysis

When a cyclic load is applied on a transcuder, the response will be the harmonic response [30]. A CMUT is biased with DC voltage to set the membrane as near as possible to collapse state where efficiency of energy conversion is maximum. Then, AC signal is applied to generate a superimposed signal. The sinusoidal AC signal with high frequency causes membrane to vibrate and create ultrasonic waves. The operational frequency of the CMUT is chosen according to the resonance frequency of the structure. At this frequency, CMUT surface velocity is maximum and creates highest pressure levels. These frequency levels have already been evaluated in modal analysis results.

While modal analysis finds eigenvalues of the system and gives modal frequencies of the structure, harmonic analysis allows the steady-state response of the system to be characterized. The response for a frequency range is obtained. Minimum and maximum frequencies with step size are input of the analysis. Only forced vibrations for the CMUTs are considered. There exist a transient response caused by membrane vibration. However this is ignored by harmonic analysis.

ANSYS solves the harmonic analysis problem as a linear analysis. Nonlinear behaviour of a structure is not considered although it is defined in the input file. It is possible to perform a prestressed harmonic analysis but large deformation effects cannot be included.

Harmonic response can be evaluated in three different methods. These are full, reduced and mode supersposition method. The most time consuming and CPU intensive method is the full method. All displacements and stress levels are calculated. The other two methods are faster and less CPU intensive but have some constraints on defining degrees of freedom values and applied loads.

In a harmonic analysis, all types of loads have to be sinusoidal in time domain. Several loads can be applied on the structure but cannot be different in terms of frequency.

Harmonic analysis for CMUTs with diamond membranes is performed using full method. The model in Figure 3.2 is used. Boundry conditions are set for the structures. Displacement of the substrate in vertical dimension is constrained. Sinusoidally time-varying load is applied as pressure on the membrane and top electrode surface. Frequency of the load is defined as a

range using the outputs of modal analysis.

In harmonic analysis, steady-state response of a linear structure is solved with the equation [30]:

$$[M]\{\ddot{u}\} + [C]\{\dot{u}\} + [K]u = F^a \tag{3.2}$$

where [M] is structural mass matrix, [C] is structural damping matrix, [K] is structural stifness matrix, $\{\ddot{u}\}$ is nodal acceleration vector, $\{\dot{u}\}$ is nodal velocity vector, $\{u\}$ is nodal displacement vector and $\{F^a\}$ is the applied load vector.

Stiffness, damping and mass effects are assumed to be constant at any frequency step. Although applied loads have to be same in frequency, phase difference is allowed. Anyhow, harmonic analysis of CMUTs with diamond membranes are performed with only one sinusoidal load (i.e. pressure). Analysis results are exported as tables and plotted in logarithmic scale using Matlab. Figures 3.36, 3.37, 3.38, 3.39, 3.40 show the normalized magnitudes for CMUTs with radii 60 μm, 44 μm, 36 μm, 27 μm and 22 μm respectively.

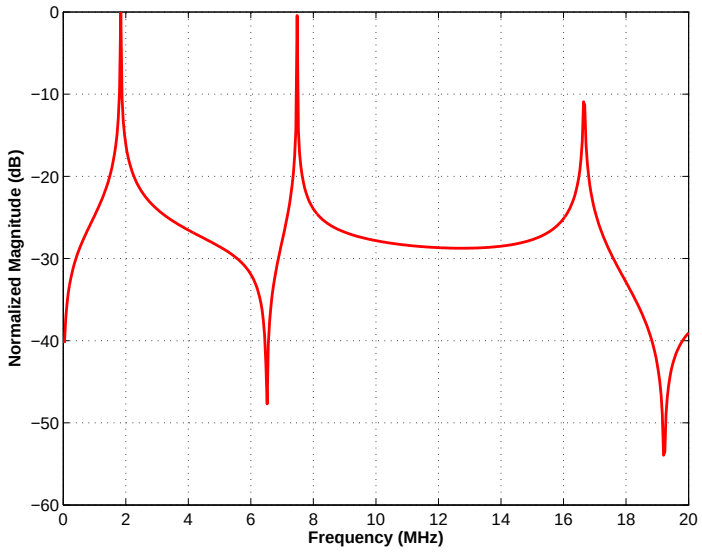

Figure 3.36: Harmonic analysis result for CMUT with radius 60 μm. Stress caused by atmospheric pressure is ignored.

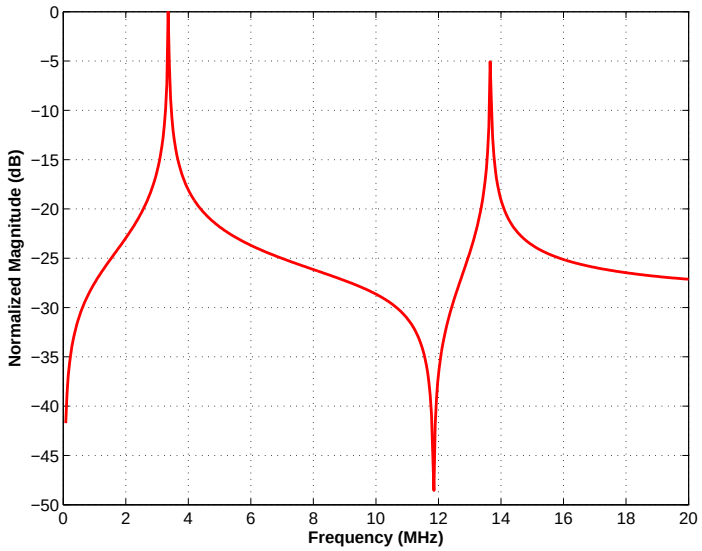

Figure 3.37: Harmonic analysis result for CMUT with radius 44 μm. Stress caused by atmospheric pressure is ignored.

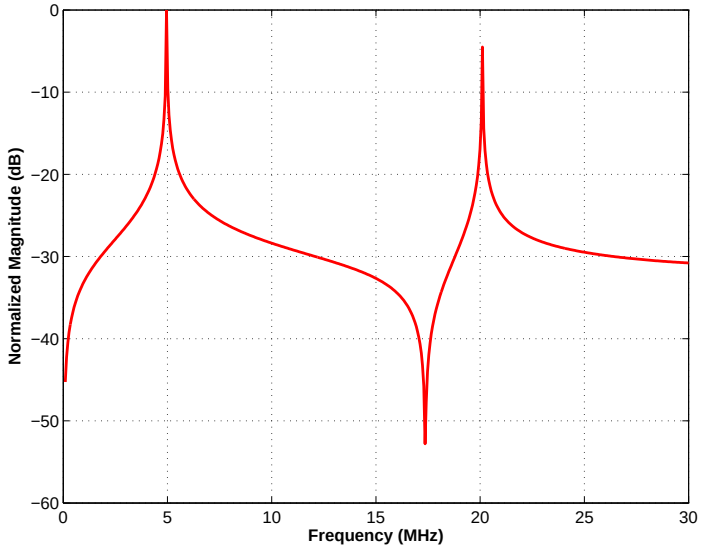

Figure 3.38: Harmonic analysis result for CMUT with radius 36 μm. Stress caused by atmospheric pressure is ignored.

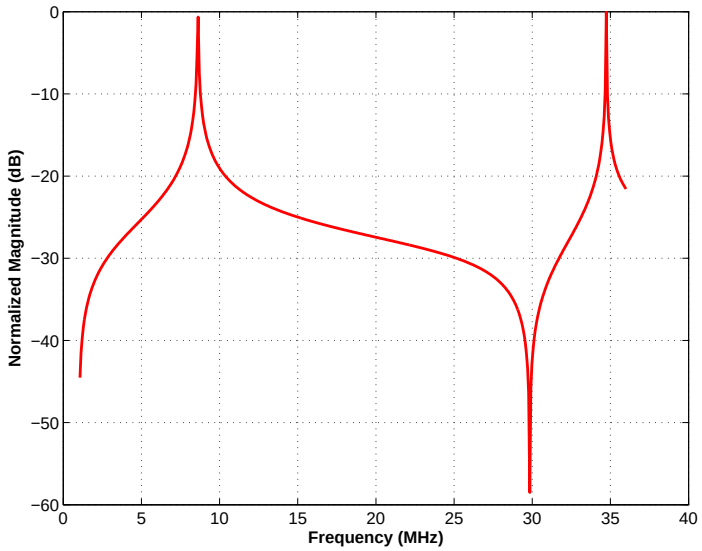

Figure 3.39: Harmonic analysis result for CMUT with radius 27 μm. Stress caused by atmospheric pressure is ignored.

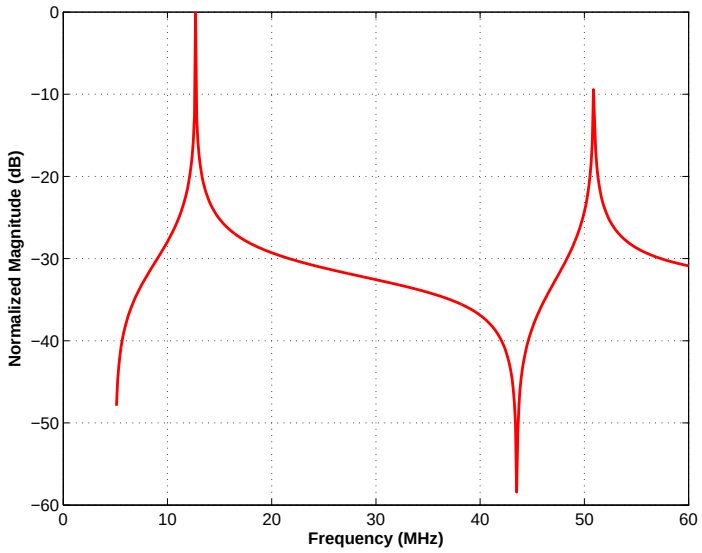

Figure 3.40: Harmonic analysis result for CMUT with radius 22 μm. Stress caused by atmospheric pressure is ignored.

Analysis is performed in vacuum environment. The data is extracted using time-history post-processor. Plots are the variation of displacement in vertical direction. Nodal displacement is chosen on the membrane center of the axisymmetric model. The displacement is the me-

chanical response of CMUT membrane to excitation signal at a specific frequency. Maximum displacement generates maximum pressure in the operational environment.

Harmonic analysis allows the bandwidth of transducers to be determined. 3-dB bandwidth around resonance frequency is obtained and shown for each CMUT radius. The results around the first mode of resonant frequencies indicates that simulations for harmonic analysis and modal analysis are consistent with each other.

3.5 Design

The CMUT masks are designed using a commercially available software package L-Edit (Tanner EDA Software Tools). A single CMUT with a circular shape which includes several cells is chosen [Figure 3.41]. The cell sizes are decided to increase the success of manufacturing process and have different resonance frequencies. While the cell size increases, the resonance frequency decreases and gap height needs to be increased due to air collapse. Circular cells are preferred in the microfabrication of the first diamond-based CMUTs in literature because of fast 2-D axisymmetric finite element modelling of these cells with a trade-off in transducer fill factor and electromechanical coupling efficiency [16].

The inner radius of circular CMUT is 2.6 mm. A 300 μm wide ground disk encircles the inner structure. The transducer surface of the inner structure is composed of many circular cells [Figure 3.42]. The distance between cells have different values for each single CMUT. Either 6 μm or 12 μm is used as the cell-to-cell seperation. Changing the cell-to-cell seperation helps to improve the fill factor of the transducer, which also improves the sensitivity or the output pressure magnitude.

The sensitivity and high output pressure is essential in a transducer design [40]. Many applications require the best performance. Penetration through a tissue and high signal-to-noise ratio can be obtained with optimum design parameters. High sensitivity and output pressure relies on the membrane displacement of a CMUT during the operation. As average displacement is increased, these values also increase.

The fill factor is defined as the ratio of total active area to the total CMUT area. Active area is the region where membrane is free to move. It is obvious that increasing the fill factor

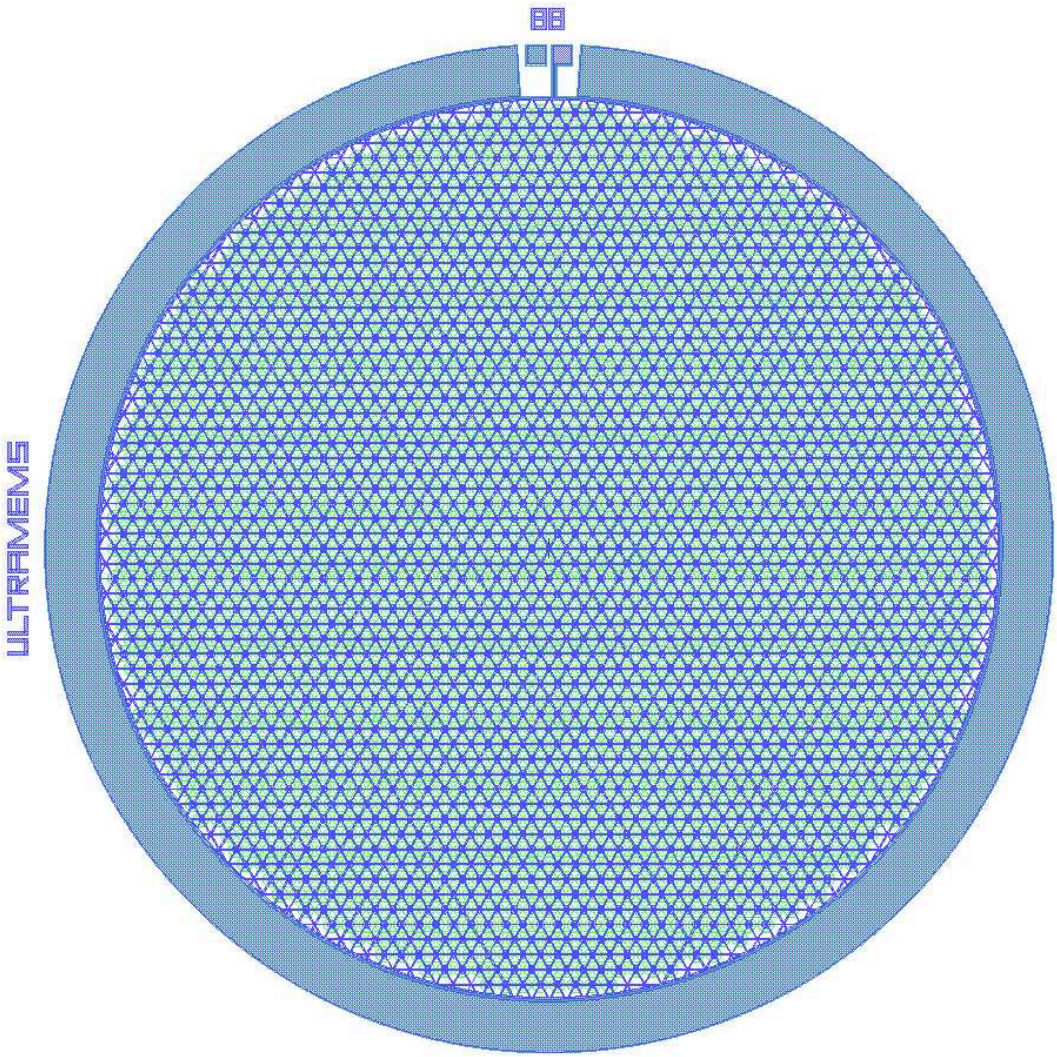

Figure 3.41: Diamond based single CMUT with 2708 cells.

increases the average displacement [40]. The calculated fill factors are given in Table 3.9.

Since the transducers are designed to operate between 1 MHz and 10 MHz, 60 μm, 44 μm, 36 μm, 27 μm and 22 μm are chosen as CMUT cells radii in the design based on the simulation results. Both 6 μm and 12 μm cell-to-cell seperation are used. Metal lines connect all cells to each other in every 6 possible direction. Each cell has a circular top electrode with a radius which is equal to the half of the membrane radius. Half-metallization provides an optimum gain-bandwidth product for a CMUT as a receiver [86]. The physical dimensions of the CMUTs are given in Table 3.9.

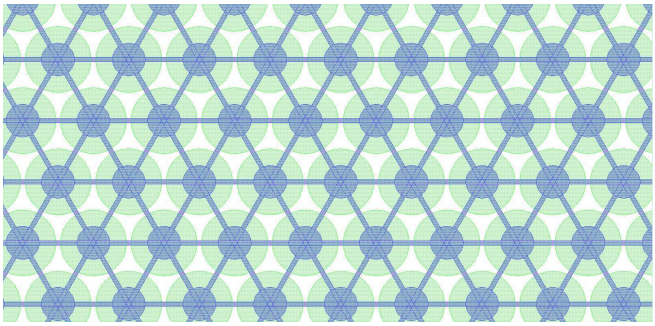

(a)

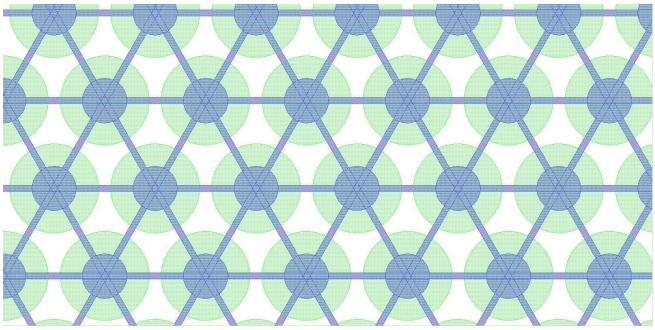

(b)

Figure 3.42: Diamond-based cells with radius 44 μm and seperation distances of (a) 6 μm and (b) 12 μm placed inside single CMUTs.

Table 3.9: Physical dimensions of diamond-based single CMUTs

Cell Diameter (µm) - Seperation (µm)	Inner radius of CMUT (µm)	Number of cells	Center-to-center cell spacing (µm)	Membrane diameter (µm)	Electrode diameter (µm)	Fill Factor (%)
120-12	2586	1372	132	120	60	74.95
120-6	2586	1500	126	120	60	82.26
88-12	2586	2398	100	88	44	70.23
88-6	2586	2708	94	88	44	79.48
72-12	2586	3404	84	72	36	66.63
72-6	2586	3930	78	72	36	77.27
54-12	2586	5538	66	54	27	60.71
54-6	2586	6698	60	54	27	73.46
44-12	2586	7682	56	44	22	55.99
44-6	2586	9656	50	44	22	70.23

Since all single CMUTs have a radius of 2.6 mm, several cells need to be placed inside with

the best accuracy. In the first design of a single CMUT mask, a cell is created in the hierarchy. Then it was placed inside the CMUT ground circle one by one. The difficulty of this design was to find the best location to start and create the layout without any misalignment. The time required to finalize a CMUT layout was too long to stay focused. Therefore, a code based algorithm is developed thanks to custom macro support of L-Edit. C programming language is used as the basis of this macro. For each cell size, a custom function is created. This function improved the design accuracy and allowed to obtain error-free design. It is possible to create a CMUT layout with any cell size and cell-to-cell seperation in a minute by changing required parameters. Although it is not used in the first production, design of hexagonal cells are also performed [Figure 3.43]. This shape allows to increase the number of cells in a single CMUT and is assumed to increase output pressure although simulations are not performed in this dissertation.

Single CMUTs with circular cells are located on the wafer as shown in Figure 3.44. A combination of all different diameters and cell-to-cell seperation distances is created to obtain a successful result in the design of the first diamond-based CMUT.

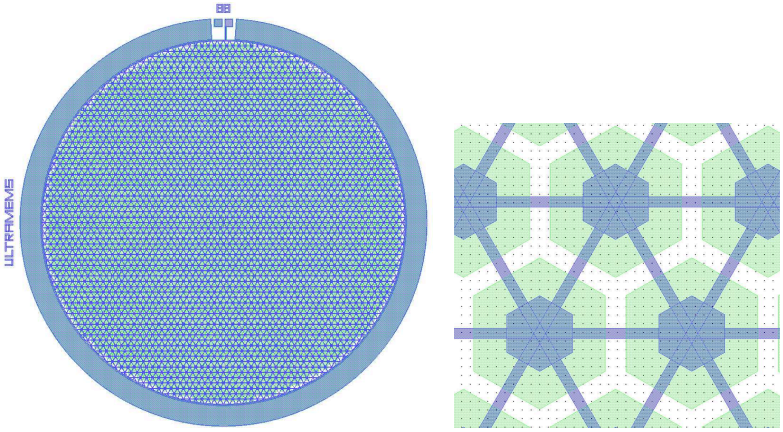

(a) (b)

Figure 3.43: (a) Single CMUT with hexagonal cells. (b) Cells with hexagonal shapes placed inside the single CMUT.

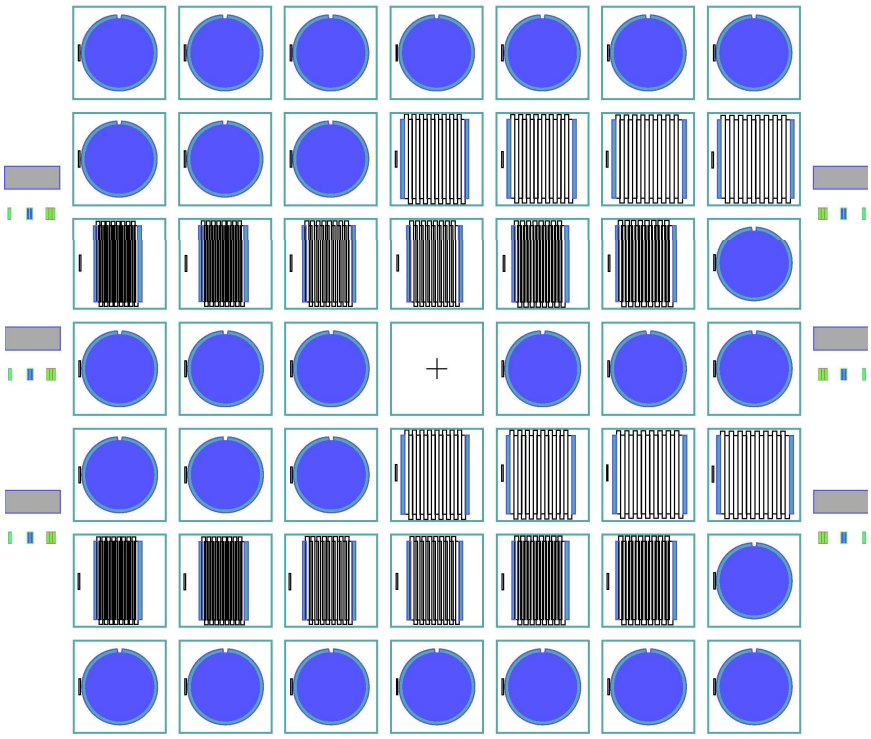

(a) Wafer mask design.

Single CMUT Radius= 60um Seperation = 6 um	Single CMUT Radius= 60um Seperation = 12 um	Single CMUT Radius= 44um Seperation = 6 um	Single CMUT Radius= 44um Seperation = 12um	Single CMUT Radius= 36um Seperation = 6 um	Single CMUT Radius= 36um Seperation = 12 um	Single CMUT Radius= 27um Seperation = 6 um
Single CMUT Radius= 27um Seperation = 12 um	Single CMUT Radius= 22um Seperation = 6 um	Single CMUT Radius= 22um Seperation = 12 um	1D Array Radius= 60um Width=375um Seperation = 6um	1D Array Radius= 60um Width=375um Seperation = 12um	1D Array Radius= 44um Width=375um Seperation = 6um	1D Array Radius= 44um Width=375um Seperation = 12um
1D Array Radius= 36um Width=250um Seperation = 12um	1D Array Radius= 36um Width=250um Seperation = 12um	1D Array Radius= 27um Width=250um Seperation = 6um	1D Array Radius= 27um Width=250um Seperation = 12um	1D Array Radius= 22um Width=250um Seperation = 6um	1D Array Radius= 22um Width=250um Seperation = 12um	Single CMUT Radius= 60um Seperation = 6 um
Single CMUT Radius= 60um Seperation = 12um	Single CMUT Radius= 22um Seperation = 6 um	Single CMUT Radius= 44um Seperation = 12 um	X	Single CMUT Radius= 36um Seperation = 6 um	Single CMUT Radius= 36um Seperation = 12 um	Single CMUT Radius= 27um Seperation = 6 um
Single CMUT Radius= 27um Seperation = 12 um	Single CMUT Radius= 22um Seperation = 6 um	Single CMUT Radius= 22um Seperation = 12 um	1D Array Radius= 60um Width=375um Seperation = 6um	1D Array Radius= 60um Width=375um Seperation = 12um	1D Array Radius= 44um Width=375um Seperation = 6um	1D Array Radius= 44um Width=375um Seperation = 12um
1D Array Radius= 36um Width=250um Seperation = 6um	1D Array Radius= 36um Width=250um Seperation = 12um	1D Array Radius= 27um Width=250um Seperation = 6um	1D Array Radius= 27um Width=250um Seperation = 12um	1D Array Radius= 22um Width=250um Seperation = 6um	1D Array Radius= 22um Width=250um Seperation = 12um	Single CMUT Radius= 22um Seperation = 6 um
Single CMUT Radius= 22um Seperation = 12 um	Single CMUT Radius= 36um Seperation = 6 um	Single CMUT Radius= 36um Seperation = 12 um	Single CMUT Radius= 27um Seperation = 6 um	Single CMUT Radius= 27um Seperation = 12 um	Single CMUT Radius= 22um Seperation = 6 um	Single CMUT Radius= 22um Seperation = 12um

(b) Wafer mask layout.

Figure 3.44: Design and layout of single CMUTs and 1-D CMUT arrays.

CHAPTER 4

TEST AND VERIFICATION

4.1 Introduction

Ultrananocrystalline diamond (UNCD), featuring smaller grain size and surface roughness has been recently explored for microelectromechanical systems (MEMS) applications such as RF MEMS resonators [19], hybrid piezoelectric/UNCD cantilevers [20], and capacitive micromachined ultrasonic transducers. Microfabrication of CMUTs with diamond membranes [21] is based on the plasma-activated wafer bonding technology, and use of diamond as a membrane material enables the utilization of key material properties of diamond such as high Young's Modulus, extreme hardness and large thermal conductivity [18] to improve performance and reliability of CMUTs.

Diamond-based CMUT is operated in immersion for the first time. Experimental characterization of the first generation CMUT in immersion is performed using a broadband hydrophone in an ultrasound measurement system. Based on the 2-D pressure map of the CMUT, main lobe and side lobes are experimentally identified and are verified with theory. The spectrum of the diamond-based CMUT is measured for different AC amplitudes with a frequency sweep.

4.2 Device Description

A single CMUT having a circular shape is designed with an inner radius of 2.6 mm [Figure 4.1(a)]. A 300 μm wide ground disk encircles the inner structure. The transducer surface of the inner structure is composed of many circular cells [Figure 4.1(b)]. Half metallization of the top electrode and cell-to-cell separation of 6 μm are used in the design. Circular cells

are preferred in the microfabrication of the first diamond-based CMUTs in literature because of fast 2-D axisymmetric finite element modelling of these cells with a trade-off in transducer fill factor and electromechanical coupling efficiency [16].

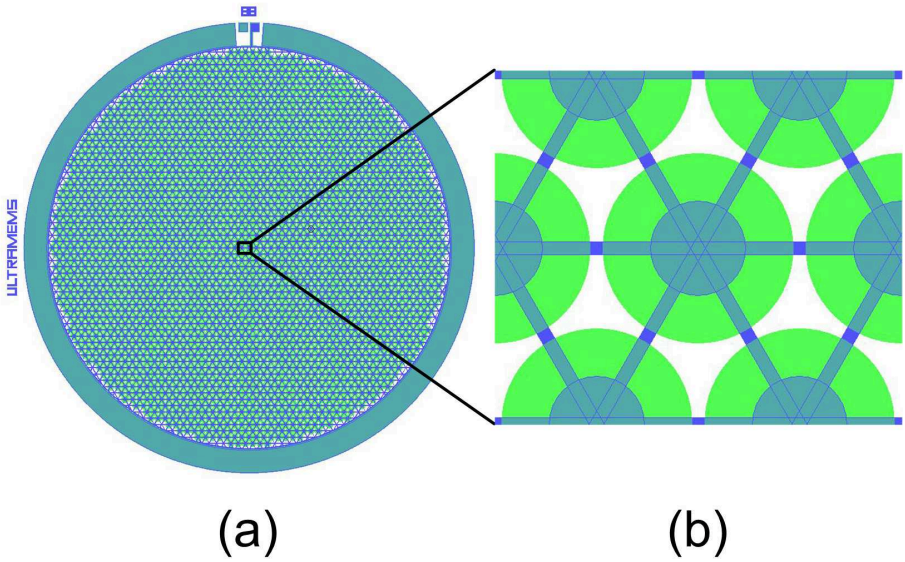

Figure 4.1: A single CMUT design having a circular shape. (a) Top view of single CMUT drawing. (b) Magnified, top view of a CMUT cell and its neighboring cells.

The cross-sectional drawing of the diamond-based CMUT was shown in Figure 3.1. The physical dimensions of the CMUTs tested are given in Table 4.1.

Table 4.1: Physical Parameters of the diamond-based CMUTs.

Inner radius of the CMUT, μm	2586	2586
Number of cells	1500	2708
Center-to-center cell spacing (d_s), μm	126	94
Membrane diameter (d_m), μm	120	88
Electrode diameter (d_{Al}), μm	60	44
Electrode thickness (t_{Al}), μm	0.4	0.4
Diamond membrane thickness (t_m), μm	1.0	1.0
High temperature oxide thickness (t_{hto}), μm	0.23	0.23
Oxide and gap thickness (t_o), μm	1.57	1.57
Silicon substrate thickness (t_s), μm	525	525

4.3 Ultrasound Measurement Software

Getting results with minimal errors is subject to setup a healthy and stabilized environment and acquire as much data as possible. Automated measurement becomes very important at this step. Using measurement devices manually causes waste of time and labor while increasing human factor in errors. Therefore, in order to control and monitor measurement devices and acquire measurement results, it is decided to develop a software based application. Among others, Labview, as a widely used development environment in industrial applications and providing support for many devices, has been chosen to build this application.

Labview is a product of National Instruments and includes an environment where a graphical programming language is used. In Labview, it is possible to develop an application with a convenient user interface while communicating with the measurement devices of test setup in the background. It is possible to use Labview on Microsoft Windows, Unix or Linux. Applications developed in Labview environment can be built to create executables which will run standalone. A standalone application will benefit more from the processing power. In addition, multithreaded structure will help to get a more responsive application.

In a graphical programming environment, symbols representing measurement equipments are used easily with drag-&-drop. However, as the application size and complexity of the program increases, it becomes more difficult and takes more time to maintain stability and efficiency when compared to traditional text based programming languages. Error control has to be carefully programmed and applications need to be tested intensively. Debugging with graphical programming is more difficult than debugging with textual programming and switching between several windows (i.e. graphical code) has to be done. When multithreaded structure of a program is used with graphical programming language, topology has to be handled carefully.

Modularity lets the developer to reuse the graphical code in the application. Yet, variable data transfer between modular blocks and timing of multithreaded blocks preserves the difficulty in the planning of topology.

Labview contains many packages and it is possible to include these to process data during measurement in an application. On the fly processing of data helps to monitor and verify a healthy test setup without having to wait till the end of measurement which may last for a few

days.

With all advantages and disadvantages, Labview has been chosen and as a result of long development and test progress, the Ultrasound Measurement Software (ULTRASCAN) is created. It is aimed to easily control and monitor all the test equipments during the measurements with a single user interface as shown in Figure 4.2. This user interface helps to easily initialize the equipments and reflect the status of parameters at each step. Simplicity of the interface helps the user to focus on test procedure while many and complex blocks are running in the backgrund.

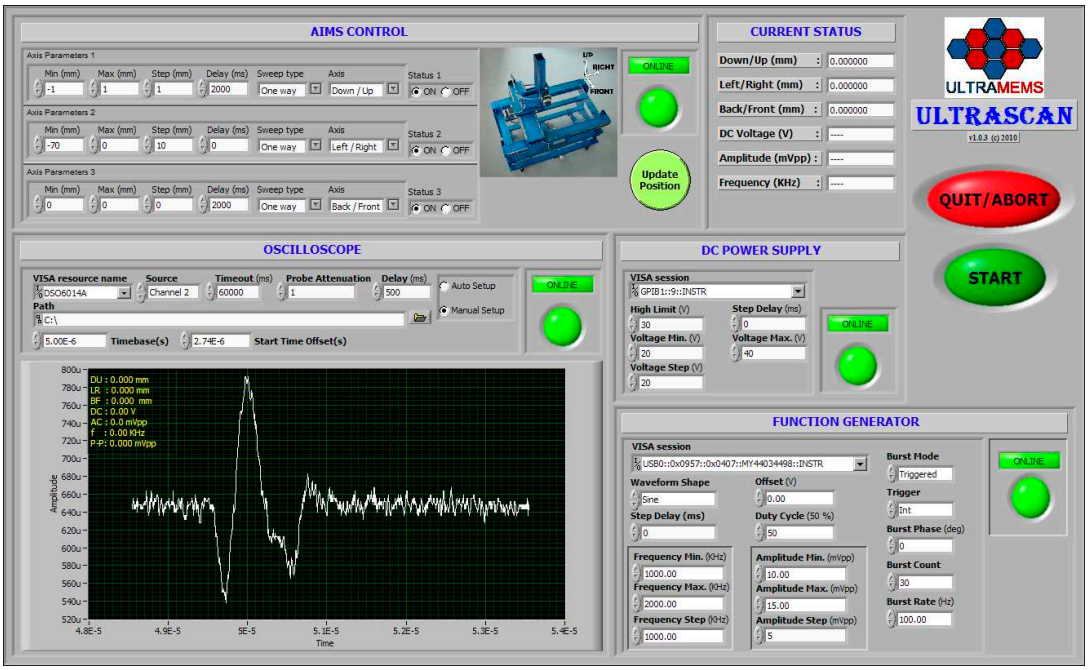

Figure 4.2: Front Panel of ULTRASCAN.

ULTRASCAN is able to control AIMS (Acoustic Intensity Measurement System), a function generator, a dc power supply and an oscilloscope. All these equipments are controlled with a loop-in-loop principle. It is possible to run a test procedure with any combination and order of these equipments. Any test equipment can be disabled with ONLINE buttons. Although ULTRASCAN benefits from the 3D positioning capability of AIMS, not only the whole system but also any axis can be disabled. Therefore, 1D, 2D or 3D measurements are different options which can be chosen in a test procedure.

Complex block diagram of the main front panel running in the background is placed in stacked sequence structures which show only the chosen block in the sequence at any time. While this helps to decrease the complexity of view during development, real size of the graphical code is hidden. However there exists also a disadvantage which is the risk of affecting the hidden code while modifying the visible one.

ULTRASCAN uses VISA (Virtual Instrument Software Architecture) to communicate with the test equipments (i.e. equipments except AIMS). VISA is used in industry as a standard I/O language which provides the capability to communicate with the devices having different interface types (e.g. Serial, GPIB, VXI, USB etc.). Labview by National Instruments implements NI-VISA, a version of VISA. VISA hides the low-level driver calls and provides standard high-level APIs (Application Programming Interface) regardless of the interface types. Therefore, it is possible to change the interface type of equipment in the setup without changing the code. VISA is portable among different platforms.

Notifier Operations as shown in Figure 4.3 are used to synchronize the subsystems and transfer status parameters between main block and sub blocks. Notifier functions help to suspend the execution of block diagrams for synchronization purposes. When a command is executed on equipment, a message is sent to the main panel and waits until ”continue message” is received from the main panel. Main panel tells the block which is waiting in the order to continue. Since the Notifier functions do not buffer sent messages, unexpected behavior of equipments are prevented during initialization or measurement.

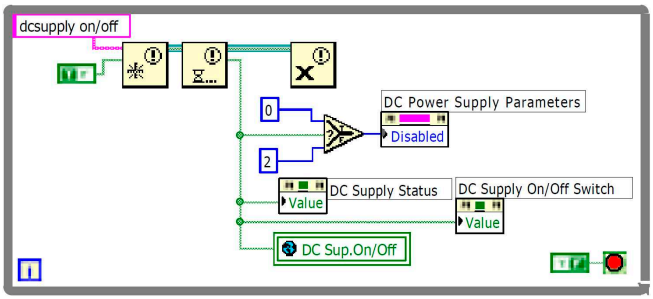

Figure 4.3: Notifiers used to send messages and transfer parameters between blocks.

ULTRASCAN controls the step motors on the AIMS through its special hardware and software. AIMS software exports the required functions to control and acquire the status through

its DLLs. Labview environment supports calling these functions inside the applications. The block diagram of the separate VI which interfaces AIMS and controls one axis is behind the front panel shown in Figure 4.4. When ULTRASCAN is run, it checks for AIMS software and warns if it is not available in the environment. If it is available, it requests for the status of step motors and initializes status parameters and axis coordinates.

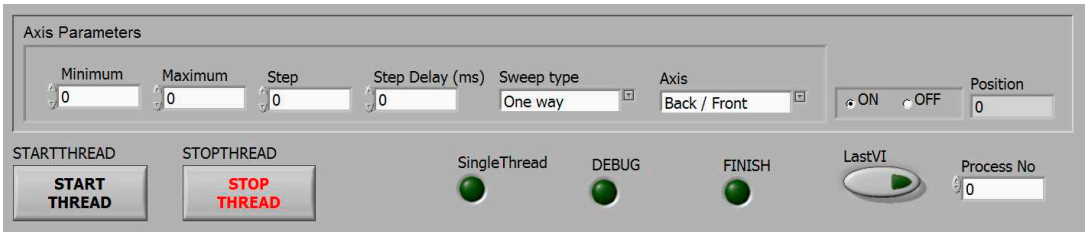

Figure 4.4: Axis Control front panel.

Since hardware limits are not available for step motors, positional movements need to be handled very carefully. However, thanks to functions implemented in ULTRASCAN, positional limits can be defined through the user interface shown in Figure 4.5 and block diagram is hidden behind it.

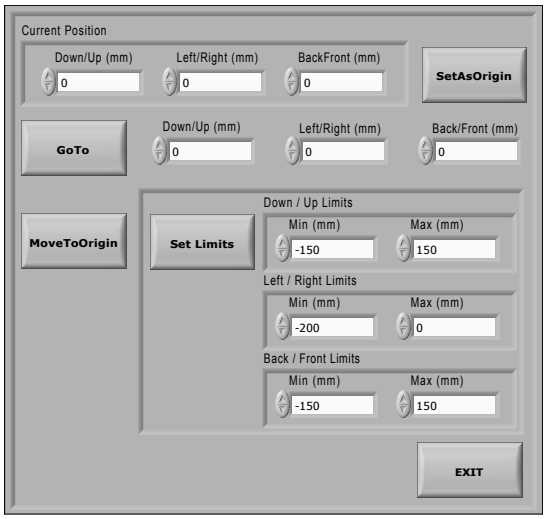

Figure 4.5: Front Panel used for AIMS position update

Step range for each axis is defined through application user interface. At each measurement

step, positions of step motors for each axis are changed in a pre-defined order. To maintain mechanical stability, pre-defined delay is applied between each position update. Sweep type can be defined either one way or bidirectional. Step size can be as small as 11.1 um.

Communication with DC power supply is performed through VISA session. Voltage range is defined with Vmin and Vmax values before measurement is started. High Limit parameter sets the limit on DC power supply to prevent unexpected voltage increase. Step delay can be defined for stabilization purposes. DC power supply is controlled through a separate subVI. When main application is run, all subVIs are loaded into memory. The front panel of subVI which controls DC power supply is shown in Figure 4.6. When it is loaded, it waits for continue message from main panel and executes one step at each message arrival. Initial parameters are carried through a cluster of wires. When the status changes, main block is informed through functions.

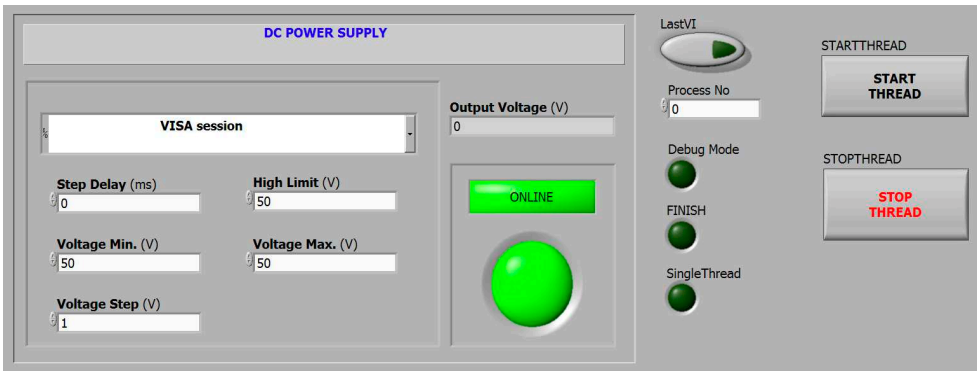

Figure 4.6: Block diagram used to control DC Power Supply

The front panel of subVI used to control function generator is shown in Figure 4.7. Function generator can be set to either continuous mode or burst mode. Several waveform shapes are supported by ULTRASCAN in case of the hardware support existance. All the parameters required for a CMUT test can be set through ULTRASCAN functions. Both frequency sweep and amplitude sweep are available. Step delay can be set if it is required for stabilization.

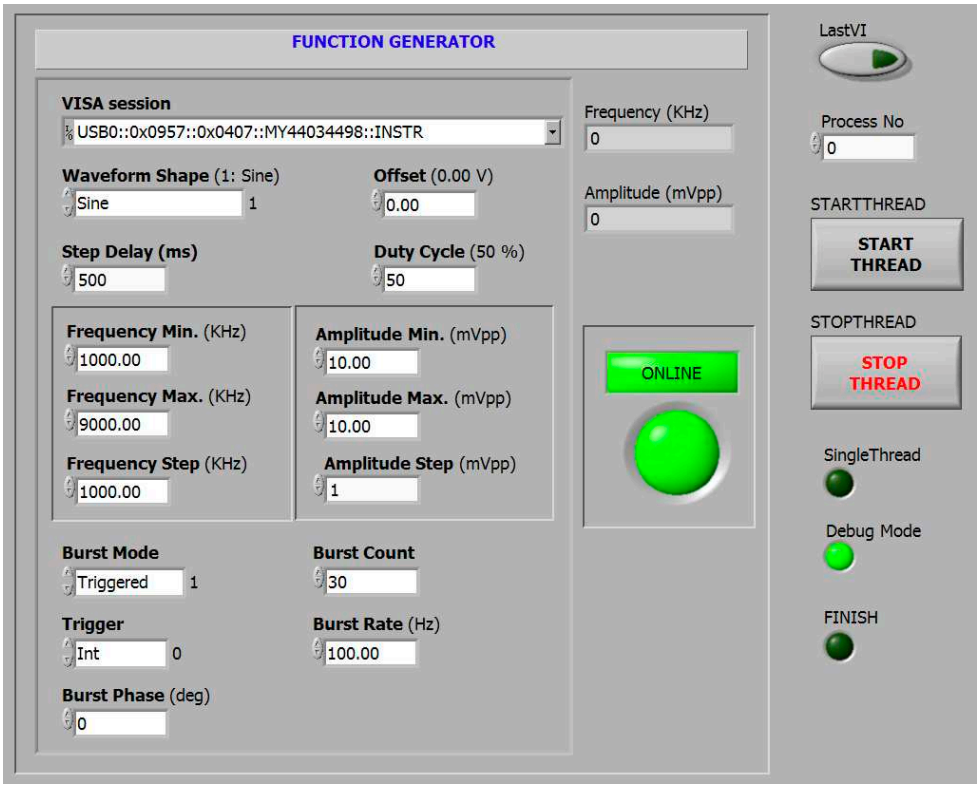

Figure 4.7: Block diagram used to control Function Generator

Oscilloscope is controlled through the subVI where its front panel is given in Figure 4.8. This instrument is also controlled through a VISA session. However, error control and setting the parameters need to be handled very careful with this equipment since it is the slowest in the test setup. Either auto setup or manual setup can be used for measurements. At each measurement step graphical representation of the acquired data and key parameters are shown on the PC screen through application user interface. All these data are also saved to a pre-defined path as a separate file for each measurement step in a special format which can be handled by Matlab.

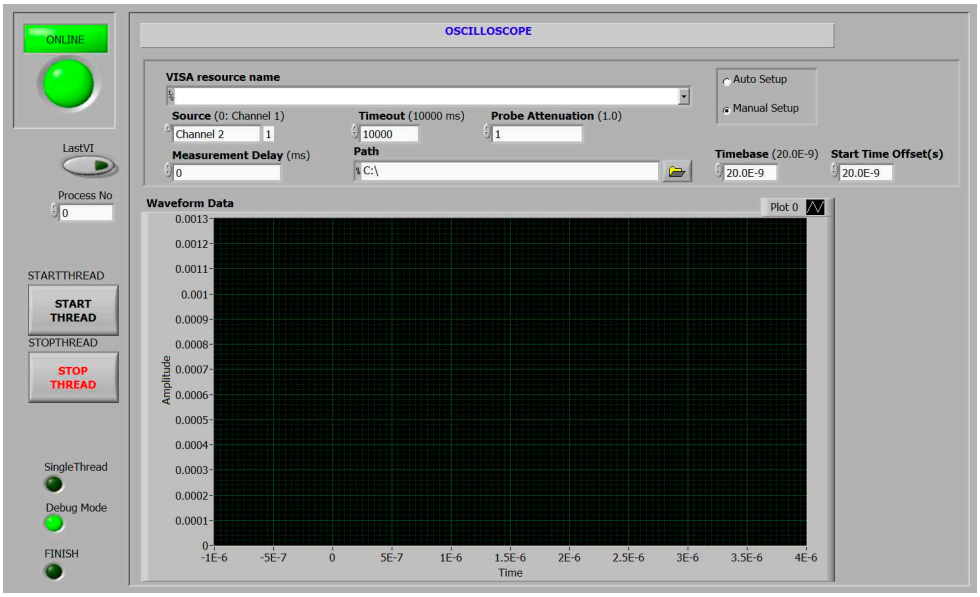

Figure 4.8: Block diagram used to controlOscilloscope

4.4 Experimental Setup

The acoustic pressure produced by a diamond-based CMUT is measured using the experimental setup in Figure 4.9. The setup includes a DC supply (PS310, Stanford Research Systems, CA, USA) and a function generator (33220A or 81150A, Agilent Technologies, CA, USA) connected to an RF power amplifier (A-075, Electronics&Innovation, NY, USA) for biasing and driving the transducer, respectively. The DC and AC voltages are provided to a bias-T circuit connected to the CMUT. A broadband hydrophone (HNA-0400, Onda Corporation, CA, USA) connected to an immersible preamplifier (AH-2020-25, Onda Corporation, CA, USA) is placed in a motion controlled stage in an ultrasound measurement system (AIMS, Onda Corporation, CA, USA). The output signal of the preamplifier is acquired by an oscilloscope (DSO6034A, Agilent Technologies, CA, US), which is triggered by the function generator. All these instruments are controlled and monitored by a PC running in-house developed ULTRASCAN program based on a software package (LabView, National Instruments, TX, USA). Communication with the instruments is handled by a commonly used object oriented I/O language, VISA (Virtual Instrument Software Architecture).

Ultrasound measurement system features special hardware and software for positioning hy-

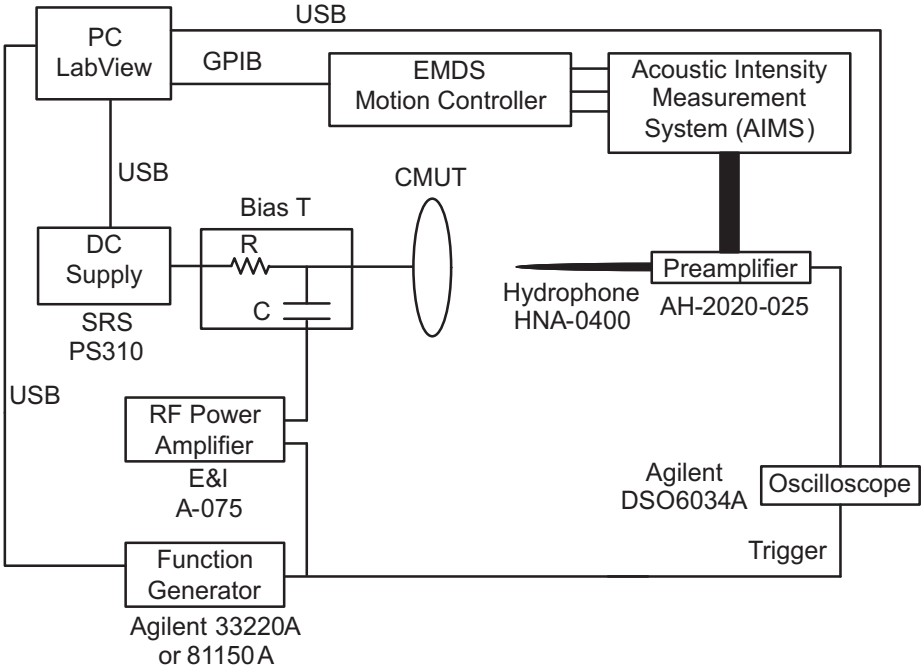

Figure 4.9: Experimental setup used for acoustic field scan of a CMUT.

drophone in 3 axes (x,y,z) with 11.1 μm resolution. ULTRASCAN communicates with AIMS [Figure 4.10] through its software and functions exported through the installed DLLs. The data acquired by the oscilloscope has 1000 points for waveform snapshot in averaging mode. However, this software can acquire a data having higher number of points by changing time base and offset parameters automatically to receive multiple waveforms, and merging them as a single waveform.

4.5 Diffraction

Measurement results need to be carefully handled since accuracy is crucial to verify with the theoretical results. CMUTs, which are used in the experiments, have circular geometry where several single cells reside inside. Hydrophone is also a circular transducer which is operated in receive mode. If the transmitter and receiver were ideally point sources, measurement results could be used as is. However, diffraction of acoustical signals should be considered when geometry makes it require.

Figure 4.11 shows that paths between two points on the surfaces of transducers are not always

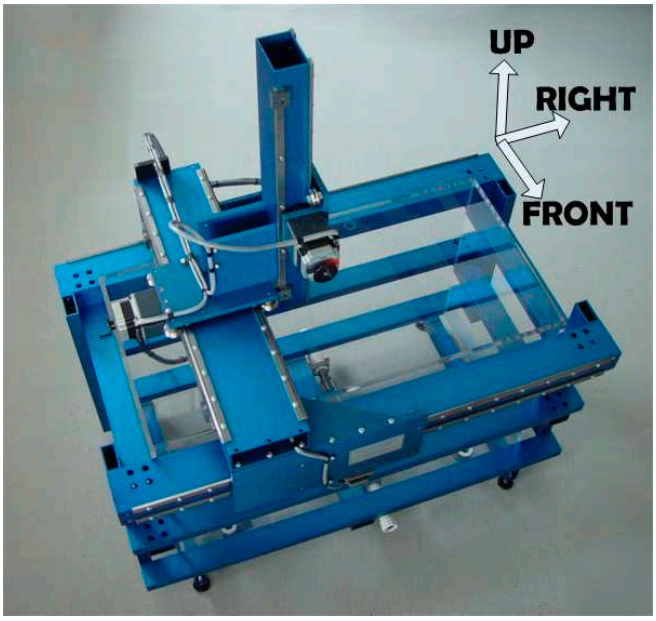

Figure 4.10: Photo of AIMS

equal. Shortest path is between the centers and longest path is between the opposite edges.

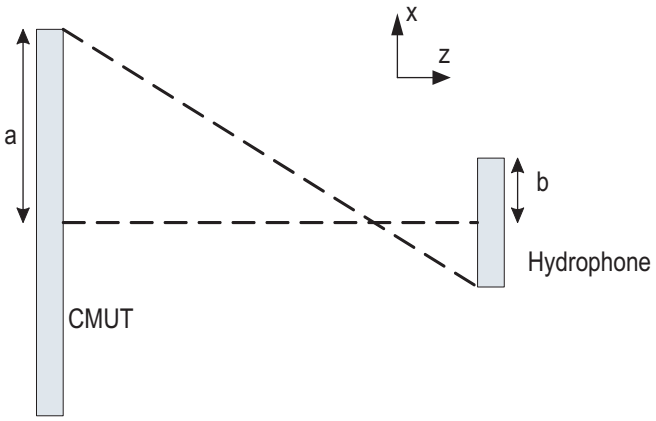

Figure 4.11: CMUT as a transmitter with radius a and hydrophone as a receiver with radius b.

To minimize the measurement errors, diffraction correction factor (D) [31] can be calculated for the axial pressure of a circular piston transducer using an exact theoretical expression by [32]:

$$D = \begin{cases} e^{-jkz} - \dfrac{2}{\pi\gamma^2} \displaystyle\int_{1-\gamma}^{1+\gamma} \sqrt{1 - \left(\frac{1-\gamma^2+\xi^2}{2\xi}\right)} \times \exp\left[-jka\sqrt{\xi^2 + \left(\frac{z}{a}\right)^2}\right] d\xi \ , \ \gamma \leq 1 \\ \\ \dfrac{e^{-jkz}}{\gamma^2} - \dfrac{2}{\pi} \displaystyle\int_{1-1/\gamma}^{1+1/\gamma} \sqrt{1 - \left(\frac{1-\gamma^{-2}+\xi^2}{2\xi}\right)} \times \exp\left[-jka\sqrt{(\gamma\xi)^2 + \left(\frac{z}{a}\right)^2}\right] d\xi \ , \ \gamma > 1 \end{cases} \tag{4.1}$$

where a is the radius of the transducer, b is the radius of the hydrophone, γ is the ratio of b over a, and z is the axial distance form the transducer center.

An approximate expression is also available [33]:

$$D = 1 - \frac{2\sqrt{z^2+a^2}}{kab} J1\left(\frac{kab}{\sqrt{z^2+a^2}}\right) x e^{-jk(\sqrt{z^2+a^2}-z)} \tag{4.2}$$

where z is axial distance from transducer surface and λ is wavelength. This equation is valid only for $\frac{b}{a} << 1$, $\frac{ab}{z^2} << 1$ and $\frac{a^2}{\lambda} << \frac{z^3}{b^2}$ [31].

In the measurements, exact theoretical expression [Equation 4.1] is used to calculate and apply diffraction correction factor.

4.6 Measurements

When the experimental test setup is built and the first diamond-based CMUTs are manufactured, the CMUT with a membrane radius of 60 μm is tested in air. The electrical impedance value and resonance frequency are obtained. Then, the CMUT with a membrane radius of 44 μm is tested in air. Electrical impedance of it is also measured. The resonance frequency in air is found. This CMUT is later immersed in sunflower oil and experimental results are obtained.

CMUT with a membrane radius of 60 μm

The diamond-based CMUT with radius 60 μm is used to get the first measurement results.

The first step was to use an impedance analyzer (4294A, Agilent Technologies, CA, USA)) to find the electrical impedance values. The CMUT is biased with a DC voltage of 40 V. The impedance is measured between 1 MHz and 3 MHz [Figure 4.12].

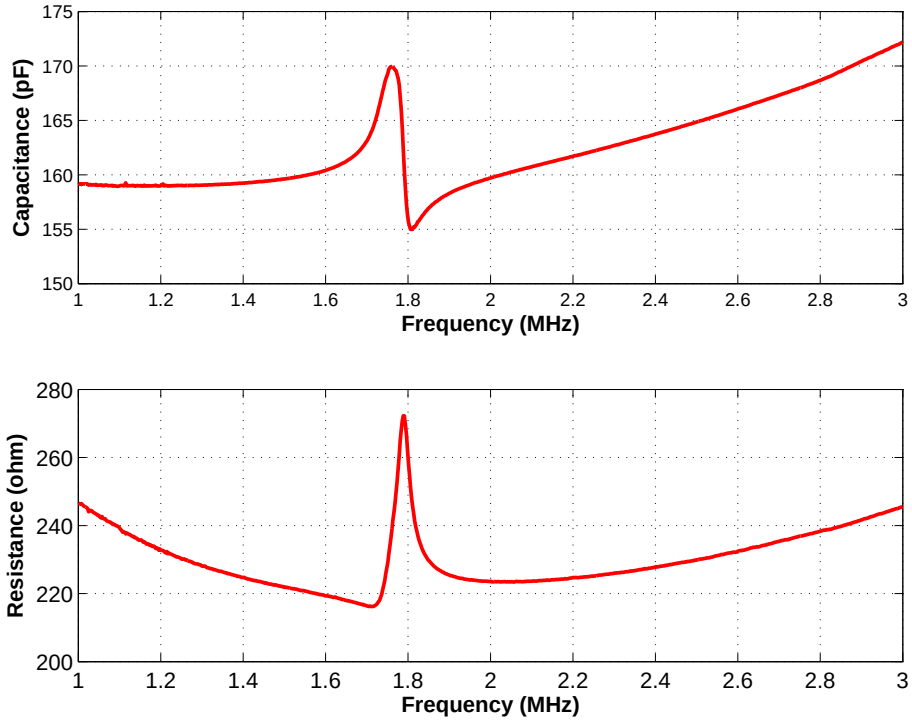

Figure 4.12: Electrical impedance measurement (capacitance and resistance) of CMUT with radius 60um in air at a bias voltage of 40 V.

The resonance frequency is observed to be 1.79 MHz in air. The frequency analysis of the CMUT using finite element method with ANSYS (ANSYS Inc., PA, USA) was calculated as 1.83 MHz which is very close to the measured value. The CMUT is then tested in the experimental setup [Figure 4.9]. Hydrophone is positioned at the origin along the normal of the CMUT and which has a distance of 2.6 mm from the CMUT surface. A DC voltage of 100 V and a sine signal of 36 $V_{p\text{-}p}$ is applied to the CMUT. The frequency of the sine signal is swept from 1.7 MHz to 1.9 MHz. The mechanical resonance frequecy is also observed to be 1.79 MHz [Figure 4.13].

CMUT with a membrane radius of 44 μm

Electrical impedance measurement of the CMUT is performed in air at a probe station using an impedance analyzer (4294A, Agilent Technologies, CA, USA). The impedance of the

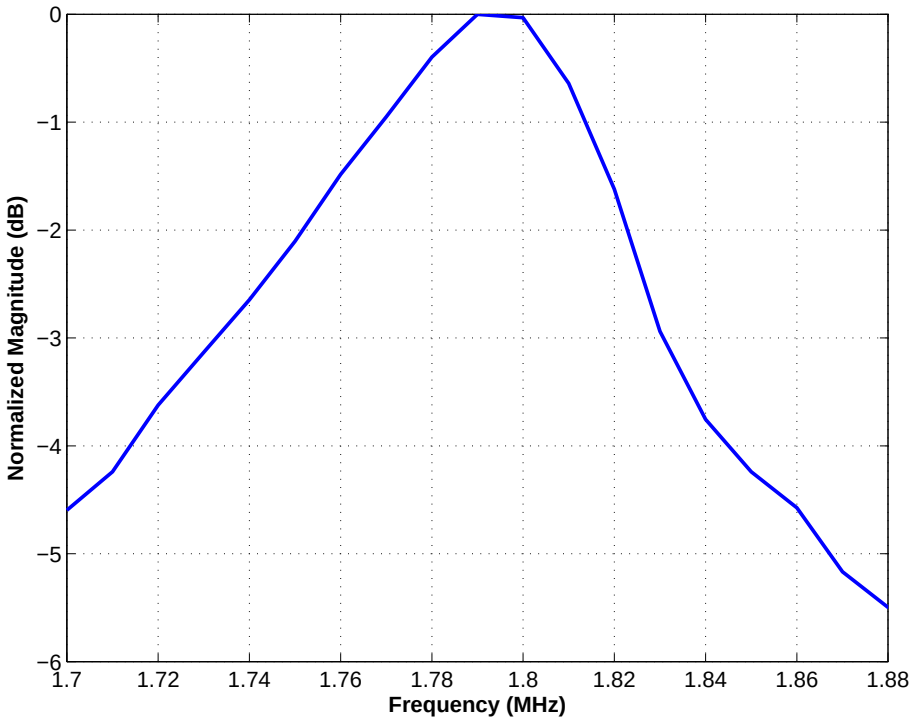

Figure 4.13: Spectrum of the diamond-based CMUT with radius 60 μm in air with a DC bias voltage of 100 V and AC sine signal of 36 $V_{p\text{-}p}$

CMUT biased at 40 V is measured between 2 MHz and 4 MHz [Figure 4.14].

Resonance frequency of 2.8 MHz is observed in the experiment. Based on finite element modelling (FEM) using a commercially available software package (ANSYS, ANSYS Inc., PA, USA), resonance frequency of 3.36 MHz is calculated for the CMUT. A collapse voltage of 557 V is calculated using finite element analysis (FEA). The experimental and calculated collapse voltages are expected to be close although a maximum DC voltage of 150 V is applied for this CMUT during the experiments. This is to protect the insufficiently thick and wide metallization of the top electrode over the diamond membrane from electrical failure.

The CMUT is tested in air with a DC bias voltage of 100 V and an AC signal of 36 $V_{p\text{-}p}$. A spectrum measurement is performed between the frequencies 2.6 MHz and 3 MHz. The peak magnitude of the measured signal is observed as expected at 2.8 MHz [Figure 4.15].

The ultrasonic field generated by the diamond-based CMUT is measured in sunflower oil using a broadband hydrophone calibrated between 1 MHz and 20 MHz. The hydrophone and the CMUT are aligned by making several initial hydrophone measurements [Figure 4.16].

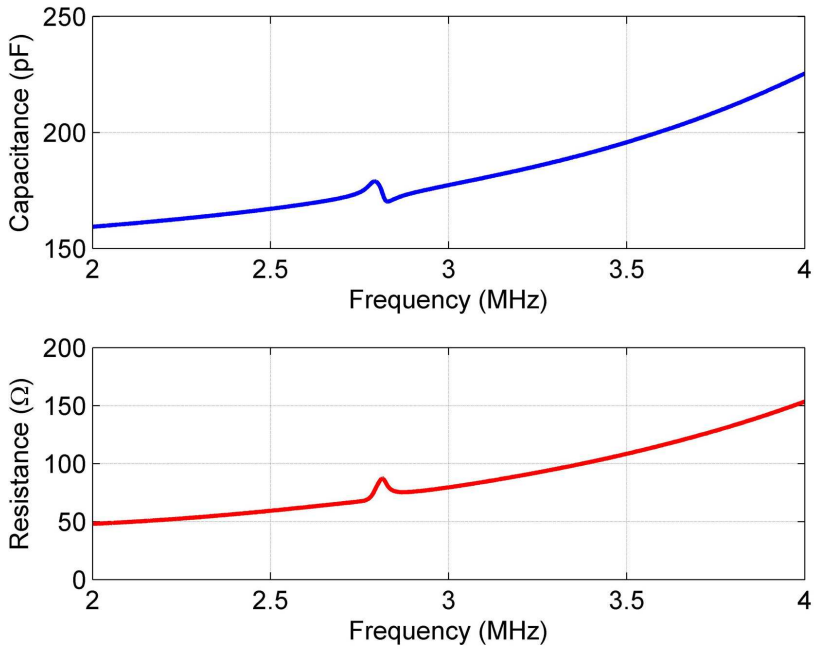

Figure 4.14: Electrical impedance measurement (capacitance and resistance) of CMUT in air at a bias voltage of 40 V.

A minimum separation distance of 4.1 mm is selected to protect the hydrophone needle from mechanical damage. The CMUT, biased at 100 V, is excited with a 10-cycle burst of 36 V_{p-p} sine signal at 3.5 MHz. The hydrophone scanned the 2-D area with a step size of 0.25 mm and 0.2 mm in x and y coordinates, respectively. The peak-to-peak hydrophone voltage is calculated using MATLAB (The MathWorks Inc., MA, USA) for the central zone of the received signal in order to remove the transient effects occurring in the initial and final parts of the 10-cycle burst [31]. The ULTRASCAN program adjusts the time base and offset of the oscilloscope to capture the received hydrophone signal automatically based on the time of flight calculations for the coordinates of the current scan location. 4096 averages are taken during the measurement. Measurement results of the peak-to-peak hydrophone voltage are shown for 2-D scan area in Figure 4.17.

Theoretical lines separating the main lobe and the side lobes are calculated using equation (2.38) for an ideal circular piston transducer [28], and are also drawn as straight lines on top of the measurement data. An excellent agreement for positioning of the main lobe and side lobes is observed between the measurement results and the theoretical calculations.

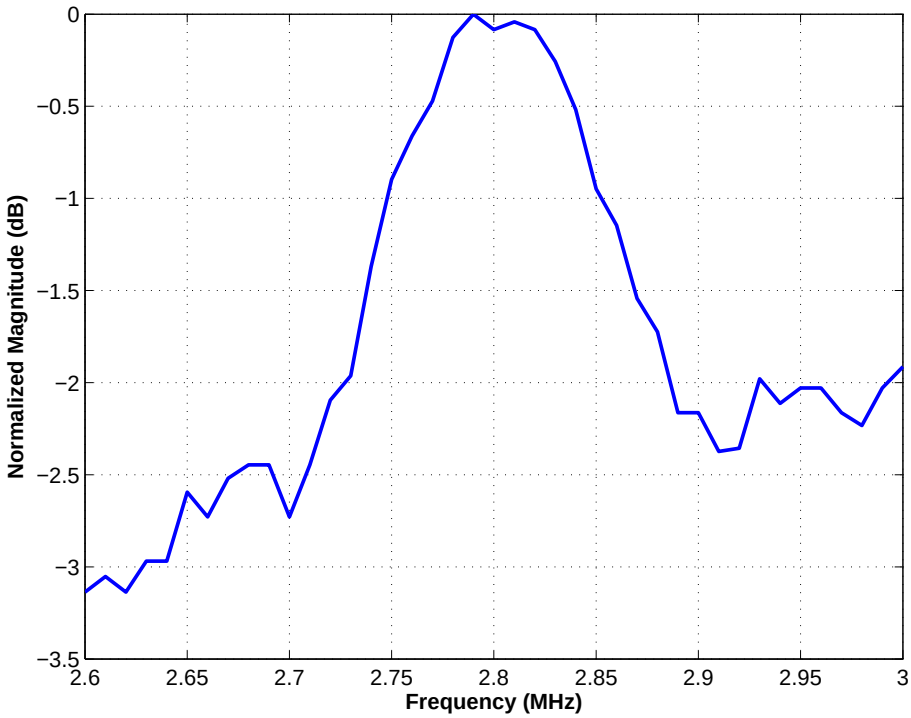

Figure 4.15: Spectrum of the diamond-based CMUT with radius 44 μm in air with a DC bias voltage of 100 V and AC sine signal of 36 $V_{p\text{-}p}$

The peak-to-peak hydrophone signal at the center line of the CMUT (x=0 mm) is extracted from the 2-D scan data, and presented in Figure 4.18.

A theoretical calculation of the pressure at the center line for a circular piston transducer is also presented using equation (4.2) for comparison [31]. Hydrophone radius of 200 μm [31] and attenuation (0.657 dB/cm at 3.5 MHz) of sunflower oil [34] are taken into account in the calculations. In the Fraunhofer region (-45 mm<y<-15 mm), an excellent match is observed between the measurement and the theory. In the Fresnel region, rapid interference maxima and minima is expected from the theory [28]. Because of the minimum separation distance of hydrophone and the CMUT, the measurement data is limited in the Fresnel region. The experimental and theoretical minima coincide at x=-8 mm, although the normalized measured pressure (-6.3 dB) is not as low as that of the theoretical one (-23.4 dB).

Using the 2-D scan data, and the calibration values of the hydrophone and the preamplifier, the acoustic output pressure is presented in Figure 4.19 along the x-axis parallel to the CMUT surface at y=15 mm (Fresnel distance (S=1)), y=30 mm (S=2), and y=8.2 mm (S=0.5). A

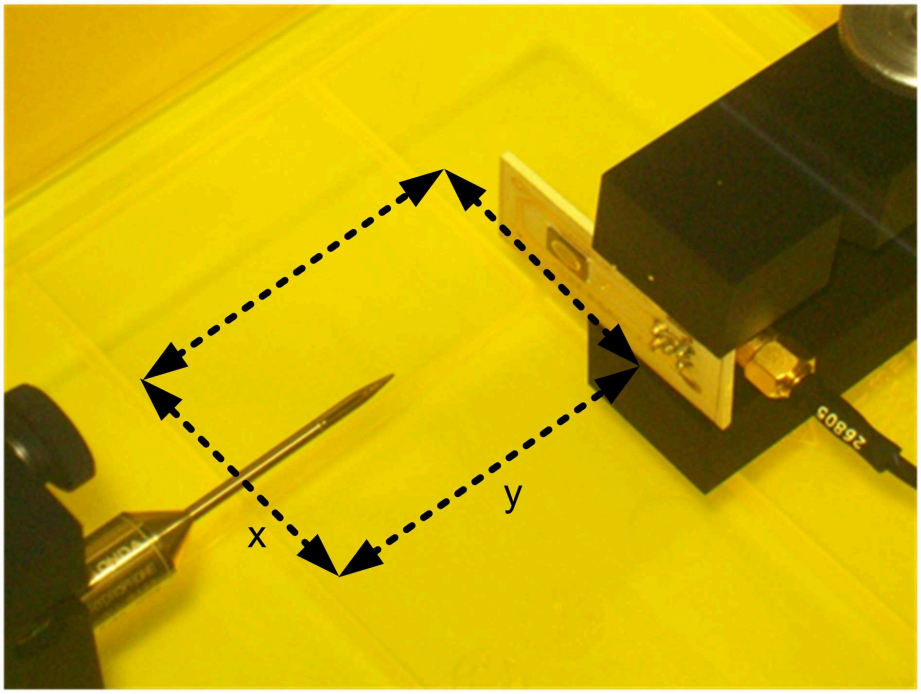

Figure 4.16: Photo of aligned diamond-based CMUT and needle hydrophone in immersion. 2-D scan area in x and y coordinates are shown visually.

maximum pressure of 8.2 kPa is measured at the Fresnel distance at x=0. A symmetrically spaced double peak at S=0.5 and a single peak with a reduced pressure magnitude at S=2 are measured as expected by the theory [28].

The hydrophone is positioned at y=-54.1 mm along the normal of the CMUT. The CMUT, biased at 100 V, is excited with a 30-cycle burst of 9 V_{p-p}, 36 V_{p-p} and 54 V_{p-p} sine signal while the frequency of the signal is swept from 1 MHz to 8 MHz with a step of 100 kHz [Figure 4.20]. A peak response at 5.6 MHz is measured for all AC amplitudes. A broadband response of the CMUT is observed except the dip observed at 4.2 MHz. Although a higher acoustic output response is observed at 5.6 MHz, 3.5 MHz is used in the 2-D scan measurement to observe the pressure in the Fresnel and the Fraunhofer regions in our limited scan area. As the AC amplitude is increased, almost a linear increase in pressure is observed in agreement with the operation of the CMUT.

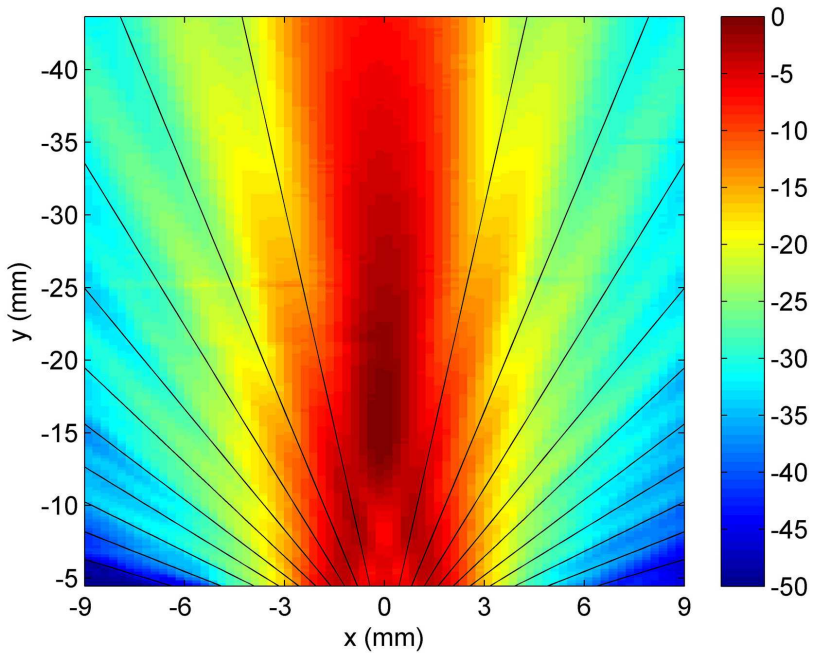

Figure 4.17: Measurement results of the normalized peak-to-peak pressure for 2-D scan area. Theoretically calculated lines separating the main lobe and the side lobes are also shown on top of the measurement data.

4.7 Discussion

The total capacitance of the diamond-based CMUT is calculated via FEM to be 89.4 pF for membranes, assuming the voltage of the top electrode extending over the full membrane. High resistive UNCD causes the actual half metallization to extend over a larger area electrically similar to other high resistive membrane materials [14]. Because the peak membrane deflection is %8 of the gap height under only atmospheric pressure, and membrane capacitance is measured at approximately %10 of the collapse voltage, theoretical capacitance calculation should be a good estimation of the membrane capacitance. Comparison with the measured total capacitance [Figure 4.14] reveals a parasitic capacitance as large as the membrane capacitance. Even more interesting is the increase of the capacitance from 160 pF at 2 MHz to 225 pF at 4 MHz whereas the series resistance increases from 50 ohm at 2 MHz to 150 ohm at 4 MHz. The silicon substrate and the undoped diamond are resistive enough to cause comparable series resistance to the capacitance of the CMUT. Although half metallization is used to reduce parasitics assuming the undoped diamond to act like an insulator, slightly graphitic

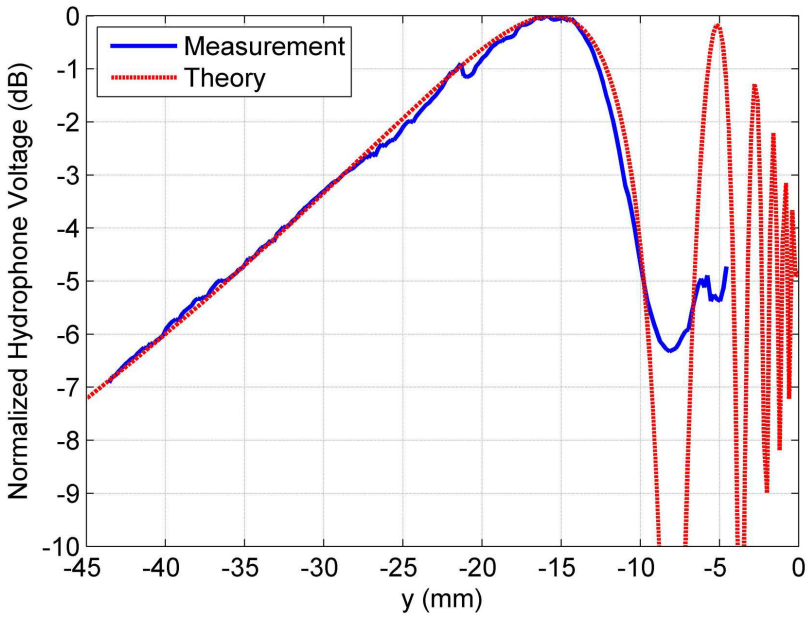

Figure 4.18: Experimental and theoretical results of the normalized peak-to-peak pressure on the normal of the CMUT surface.

nature of the UNCD makes it electrically resistive rather than an insulator, and the electrical behavior of the membrane becomes quite complex at the frequency of interest. This electrical problem causes the electrical mismatch of the transducer in transmit reducing the signal coupling to the capacitance of the CMUT at 4.2 MHz.

When the CMUT is biased at 100 V, a leakage current of 0.08 mA is supplied by the DC supply. High leakage current is an indication of the high parasitic capacitance formed by the silicon dioxide support regions of the circular membranes. However, the thickness and the width of the metal lines are initially selected for half metallization over an insulating diamond membrane. With the conductive nature of UNCD, the capacitance is larger than considered. Higher bias voltages are avoided to protect the metallization of the top electrode from electromigration under high current densities particularly over the thin metal line connecting the pad electrode to the metal on circular cells.

The experimental setup in [Figure 4.9] is a strong platform for performing precise and reliable acoustic scanning measurements. The most sensitive and vulnerable part of the system is the hydrophone. The hydrophone is broadband to be able to receive signals from all angles, and calibrated from 1 MHz up to 20 MHz. The hydrophone is of needle type, causing very low

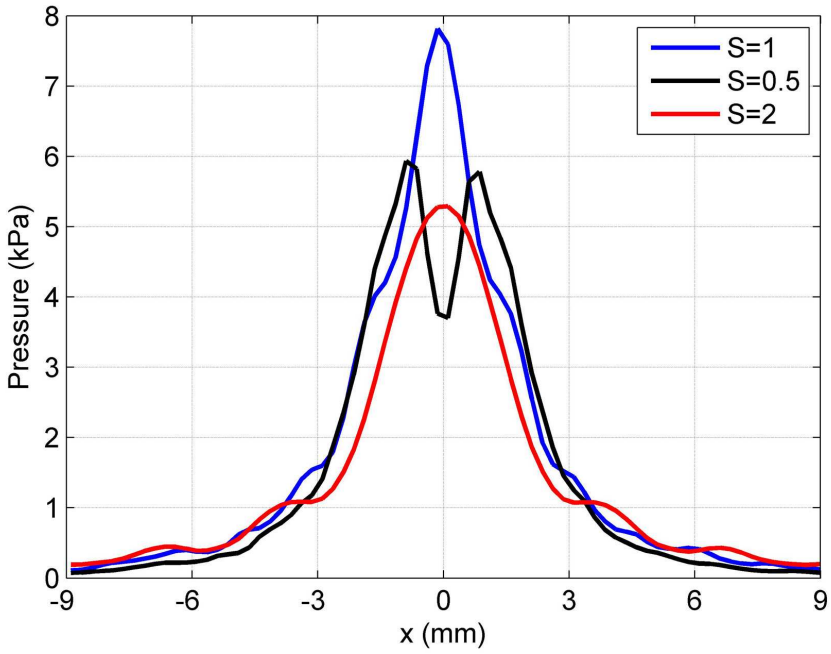

Figure 4.19: Experimental acoustic output pressure along the x-axis parallel to the CMUT surface at y=15 mm (Fresnel distance (S=1)), y=30 mm (S=2), and y=8.2 mm (S=0.5).

field disturbance. It is a commercially available hydrophone developed for high intensity ultrasound field measurements. The 2-D scan data presented in Figure 4.17 was collected in 22 hours because of averaging of 4096 waveforms for each scan location.

In all hydrophone measurements, sufficient delay of the received signal is provided for pressure mapping in the Fresnel region so that the actual acoustic signal will not be affected by the electromagnetic interference picked up by the hydrophone for high burst counts.

A broadband response of the CMUT is observed except the dip observed at 4.2 MHz. Reduced pressure output at 4.2 MHz is an indication of the electrical impedance mismatch explained earlier. Because of the comparable values of real and imaginary impedances around 4 MHz, electrical impedance mismatch causes a 5 dB loss in the transmit pressure.

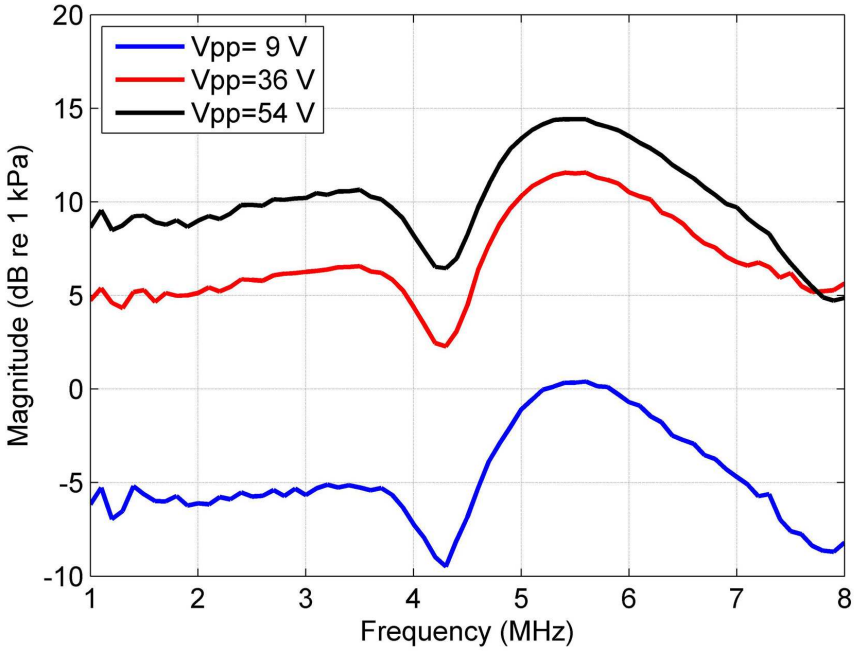

Figure 4.20: Spectrum of the diamond-based CMUT.

CHAPTER 5

CONCLUSION AND FUTURE WORK

This dissertation introduced the design and analyses results of diamond-based single CMUTs with cell-membrane radii of 60 μm, 44 μm, 36 μm, 27 μm and 22 μm. A commercially available software package, ANSYS, is used to develop the finite element models. Air deflection values are obtained for diamond membranes with a thickness of 1 μm. Stress analyses are performed and the results are provided for all membrane radii subject to this thesis. The relationship between the collapse-snapback voltages and CMUT gap heights is provided with tables. Capacitance, electrical energy, mechanical energy and stress figures are presented. Resonance frequencies are obtained with modal analyses. Harmonic analyses around first mode frequencies are done. Single CMUT masks are prepared with a commercially available software package, L-Edit (Tanner Tools) and introduced in this thesis.

A special and custom in-house software is developed for experimental test setup with a commercially available package, Labview (National Instruments) and presented. This software is designed to command and control all equipments (i.e. dc power supply, function generator, AIMS and oscilloscope) of the test setup. It is capable of gathering high-resolution data from oscilloscope with a special algorithm although the oscilloscope capabilities are limited. The in-house ultrasound measurement software allowed us to perform measurements for several hours, even days, without any interaction.

The first diamond-based CMUTs in the literature are tested in air and measurement results are provided in this thesis. The single CMUTs with cell-membrane radii of 60 μm and 44 μm are used in the tests. The test results are verified with the finite element analyses results.

The diamond-based CMUT with cell-membrane radius of 44 μm is operated in immersion for

the first time. Fresnel and Fraunhofer regions of the CMUT are characterized in sunflower oil using a combination of advanced hardware and software. The experimental results of radiation and diffraction for the diamond-based circular CMUT are verified by the theoretical calculations for a circular piston transducer.

The conclusion of this thesis can be summarized as follows:

- The novel design of diamond-based CMUTs in literature are successfully performed using ANSYS. A model to be used for FEM simulations of future work is developed and optimized.
- The first generation diamond-based CMUTs in literature are successfully tested both in air and immersion. The measurement results are verified with simulations and theoratical calculations.
- Fresnel and Fraunhofer regions of the diamond-based CMUT are characterized in sunflower oil experimentally and verified by the theoretical calculations.
- The key challenges for improving these devices are identified.

Improvement in the design of diamond-based CMUTs to operate at higher electromechanical coupling efficiency in order to increase the acoustic output pressure may be the focus of future work.

REFERENCES

[1] MEMS and Nanotechnology Exchange , www.mems-exchange.org, last visited on December 31, 2010,

[2] Southwest Center for Microsystems Education, www.scme-nm.net, last visited on September 30, 2010,

[3] http://www.cellular-news.com, last visited on January 1, 2010,

[4] Sensors Magazine, http://archives.sensorsmag.com/articles/1203/20/main.shtml, last visited on December 31, 2010,

[5] H.T. Soh, I. Ladabaum, A. Atalar, C.F. Quate, B.T. Khuri-Yakub, *Silicon micromachined ultrasonic immersion transducers*, Applied Physics Letters, Vol.69, No.24, pp.3674-3676, December 1996.

[6] M.W. Chang, T.J. Gwo, T.M. Deng, H.C. Chang, *Modeling and Design of Capacitive Micromachined Ultrasonic Transducers Based-on Database Optimization*, Journal of Physics: Conference Series, Vol.34, No.1, 2006.

[7] Matthew I. Haller, Butrus T. Khuri-Yakub *A Surface Micromachined Electrostatic Ultrasonic Air Transducer*, Ultrasonics Symposium Proceedings, IEEE, Vol.2, pp.1241-1244, 1-4 Nov 1994.

[8] D. Spoliansky, I. Ladabaum, B.T. Khuri-Yakub, *Micromachined Ultrasonic Air-Transducers (MUTs)*, Microelectronic Engineering, Vol.30, Issues 1-4, pp.535-538, January 1996.

[9] Khuri-Yakub Ultrasonics Group, http://www-kyg.stanford.edu, last visited on December 2010,

[10] I. Ladabaum, X.C. Jin, B.T. Khuri-Yakub, *Miniature drumheads: microfabricated ultrasonic transducers*, Ultrasonics, Vol.36, Issues 1-5, pp.25-29, February 1998.

[11] K.K. Park, M. Kupnik, H.J. Lee, B.T. Khuri-Yakub, I.O. Wygant, *Modeling and Measuring the Effects of Mutual Impedance on Multi-Cell CMUT Configurations*, IEEE Ultrasonics Symposium, October 2010.

[12] A.S. Ergun, Y. Huang, X. Zhuang, O. Oralkan, G.G. Yarahoglu, B.T. Khuri-Yakub *Capacitive Micromachined Ultrasonic Transducers: Fabrication Technology*, IEEE Transactions on Ultrasonics, Ferroelectrics and Frequency Control, Vol.52, No.12, pp. 2242-2258, December 2005.

[13] Y. Huang, A.S. Ergun, E. Haeggstrom, M.H. Badi, and B.T. Khuri-Yakub, *Fabricating capacitive micromachined ultrasonic transducers with wafer-bonding technology*, Journal of Microelectromechanical Systems, Vol. 12, pp. 128–137, 2003.

[14] A. S. Ergun, G. G. Yaralioglu, O. Oralkan, B. T. Khuri-Yakub, *MEMS/NEMS Techniques and Applications Techniques and Applications of Capacitive Micromachined Ultrasonic Transducers*, Springer, pp.553-615, 2006.

[15] Goksen G. Yaralioglu, Arif Sanli Ergun, Baris Bayram, Edward Hzggstrom, Butrus T. Khuri-Yakub, *Calculation and Measurement of Electromechanical Coupling Coefficient of Capacitive Micromachined Ultrasonic Transducers*, IEEE Transactions on Ultrasonics, Ferroelectrics and Frequency Control, Vol.50, No.4, April 2003.

[16] Baris Bayram, Edward Hæggstrom, Goksen G. Yaralioglu, Butrus T. Khuri-Yakub, *A New Regime for Operating Capacitive Micromachined Ultrasonic Transducers*, IEEE Transactions on Ultrasonics, Ferroelectrics and Frequency Control, Vol.50, No.9, September 2003.

[17] Baris Bayram, Omer Oralkan, A. Sanli Ergun, Edward Hæggstrom, Goksen G. Yaralioglu, Butrus T. Khuri-Yakub, *Capacitive Micromachined Ultrasonic Transducer Design for High Power Transmission*, IEEE Transactions on Ultrasonics, Ferroelectrics and Frequency Control, Vol.52, No.2, February 2005.

[18] V. Ralchenko, T. Galkina, A. Klokov, A. Sharkov, S. Chernook, V. Martovitsky, *Science and Technology of Semiconductor-On-Insulator Structures and Devices Operating in a Harsh Environment*, Springer, Dordrecht, p.77, 2005.

[19] Sergio P. Pacheco, Peter Zurcher, Steven R. Young, Don Weston, William J. Dauksher, Orlando Auciello, John A. Carlisle, Neil Kane, James P. Birrell *Characterization of Low-Temperature Ultrananocrystalline Diamond RF MEMS Resonators*, 13th GAAS Symposium, 2005.

[20] S. Srinivasan, J. Hiller, B. Kabius, O. Aucielloa, *Piezoelectric/ultrananocrystalline diamond heterostructures for high-performance multifunctional micro/nanoelectromechanical systems*, Applied Physics Letters, Vol.90, No.13, pp.134101-134101-3, March 2007.

[21] Baris Bayram, Orhan Akar, Tayfun Akin, *Plasma-activated direct bonding of diamond-on-insulator wafers to thermal oxide grown silicon wafers*, Diamond and Related Materials, Vol.19, No.11, pp.1431-1435, November 2010.

[22] Ayhan Bozkurt, Igal Ladabaum, Abdullah Atalar, Butrus T. Khuri-Yakub, *Theory and Analysis of Electrode Size Optimization for Capacitive Microfabricated Ultrasonic Transducers*, IEEE Transactions on Ultrasonics, Ferroelectrics and Frequency Control, Vol.46, No.6, November 1999.

[23] Igal Ladabaum, Xuecheng Jin, Hyongsok T. Soh, Abdullah Atalar, Butrus T. Khuri-Yakub, *Surface Micromachined Capacitive Ultrasonic Transducers*, IEEE Transactions on Ultrasonics, Ferroelectrics and Frequency Control, Vol.45, No.3, May 1998.

[24] Arif S. Ergun, Goksen G. Yaralioglu, Butrus T. Khuri-Yakub *Capacitive Micromachined Ultrasonic Transducers: Theory and Technology*, Journal of Aerospace Engineering, April 2003.

[25] Baris Bayram, Goksen G. Yaralioglu, Mario Kupnik, A. Sanli Ergun, Omer Oralkan, Amin Nikoozadeh, Butrus T. Khuri-Yakub, *Dynamic Analysis of Capacitive Micromachined Ultrasonic Transducers*, IEEE Transactions on Ultrasonics, Ferroelectrics and Frequency Control, Vol.52, No.12, December 2005 .

[26] J. Fraser, P. Reynolds, *Finite-Element Determination of Electromechanical Coupling Coefficient with Applications to Piezoelectric and Electrostatic Transducers*, presented at Joint 140th meeting of ASA/NOISECON, 2000.

[27] Goksen G. Yaralioglu, Mohammed H. Badi, A. Sanli Ergun, Butrus T. Khuri-Yakub, *Improved equivalent circuit and finite element method modeling of capacitive micromachined ultrasonic transducers*, IEEE Ultrasonics Symposium, Vol.1, pp.469-472, October 2003.

[28] J. D. N. Cheeke, *Fundamentals and applications of ultrasonic waves*, CRC Press LLC, chapter 6, 2002.

[29] Leo L. Beranek, *Acoustics*, Acoustical Society of America, 1993.

[30] Ansys.Inc, *Ansys 12 Manual*,

[31] Albert Goldstein, Darshan R. Gandhi, William D. O'Brien, *Diffraction Effects in Hydrophone Measurements*, IEEE Transactions on Ultrasonics, Ferroelectrics and Frequency Control, Vol.45, No.4, July 1998.

[32] K.Beissner, *Exact integral expression for the diffraction loss of a circular piston source*, Acustica, vol.49, pp.212-217, 1981.

[33] A. Khimunin, *Ultrasonic propogation parameter measurements incorporating exact diffraction corrections*, Acustica, vol.39, pp.78-95, 1978.

[34] Ratjika Chanamai, D. Julian McClements, *Ultrasonic Attenuation of Edible Oils*, JAOCS, Vol.75, No.10, pp.1447-1448, 1998.

[35] Can Bayram, Selim Olcum, Muhammed N. Senlik, Abdullah Atalar, *Bandwidth Improvement in a cMUT Array with Mixed Sized Elements*, IEEE Ultrasonics Symposium, 2005.

[36] Kenichiro Suzuki, Kohei Higuchi, Hiroshi Tanigawa, *A Silicon Electrostatic Ultrasonic Transducer*, IEEE Transactions on Ultrasonics, Ferroelectrics, and Frequency Control, Vol.36, No.6, November 1989.

[37] Yongli Huang, Edward O. Hæggstrom, Xuefeng Zhuang, Arif S. Ergun, Butrus T. Khuri-Yakub *A Solution to the Charging Problems in Capacitive Micromachined Ultrasonic Transducers*, IEEE Transactions on Ultrasonics, Ferroelectrics, and Frequency Control, Vol.52, No.4, November 2005.

[38] Meynier, C., Certon, D., Teston, F., Felix, N., Ferin, G., *Accurate Assessment of CMUT Devices Through Precise Electrical Impedance Measurement in Air*, IEEE Ultrasonics Symposium, 2007.

[39] Serena H. Wong., Mario Kupnik., Kim Butts-Pauly, Butrus T. Khuri-Yakub, *Advantages of Capacitive Micromachined Ultrasonics Transducers (CMUTs) for High Intensity Focused Ultrasound (HIFU)*, IEEE Ultrasonics Symposium, 2007.

[40] Serena H. Wong, Mario Kupnik, Xuefeng Zhuang, Der-Song Lin, Kim Butts-Pauly, Butrus T. Khuri-Yakub, *Evaluation of Wafer Bonded CMUTs with Rectangular Membranes Featuring High Fill Factor*, IEEE Transactions on Ultrasonics, Ferroelectrics and Frequency Control, Vol.55, No.9, September 2008.

[41] Serena H. Wong, Ronald D. Watkins, Mario Kupnik, Kim Butts Pauly, Butrus T. Khuri-Yakub, *Feasibility of MR-Temperature Mapping of Ultrasonic Heating from a CMUT*, IEEE Transactions on Ultrasonics, Ferroelectrics and Frequency Control, Vol.55, No.4, April 2008.

[42] Baris Bayram, Mario Kupnik, Goksen G. Yaralioglu, Omer Oralkan, Arif Sanli Ergun, Der-Song Lin, Serena H. Wong, Butrus T. Khuri-Yakub, *Finite Element Modeling and Experimental Characterization of Crosstalk in 1-D CMUT Arrays*, IEEE Transactions on Ultrasonics, Ferroelectrics and Frequency Control, Vol.54, No.2, February 2007.

[43] Baris Bayram, Goksen G. Yaralioglu, Arif S. Ergun, B.T. Khuri-Yakub, *Influence of the Electrode Size and Location on the Performance of a CMUT*, IEEE Ultrasonics Symposium, Vol.2, pp.949-952, October 2001.

[44] B.T. Khuri-Yakub, M. Karaman, C.H. Cheng, A.S. Ergun, G.G. Yaralioglu, B. Bayram, U. Demirci, S. Hansen, M. Badi, Ö. Oralkan, *Micromachined Capacitor Ultrasonic Transducers*, Abstracts of the 10th US-Japan Seminar on Dielectric and Piezoelectric Ceramics, pp.391-399, September 2001.

[45] Y. Huang, E. Hæggström, B. Bayram, X. Zhuang, A.S. Ergun, C.H. Cheng, B.T. Khuri-Yakub, *Collapsed Regime Operation of Capacitive Micromachined Ultrasonic Transducers based on Wafer-Bonding Technique*, IEEE Ultrasonics Symposium, Vol.2, pp.1161-1164, October 2003.

[46] Yongli Huang, Edward Hæggstrom, Baris Bayram, Xuefeng Zhuang, Arif Sanlı Ergun, Ching-Hsiang Cheng, Butrus T. Khuri-Yakub, *Comparison of Conventional and Collapsed Region Operation of Capacitive Micromachined Ultrasonic Transducers*, IEEE Transactions on Ultrasonics, Ferroelectrics and Frequency Control, Vol.53, No.10, October 2006.

[47] Omer Oralkan, Baris Bayram, Goksen G. Yaralioglu, A. Sanli Ergun, Mario Kupnik, David T. Yeh, Ira O. Wygant, Butrus T. Khuri-Yakub, *Experimental Characterization of Collapse-Mode CMUT Operation*, IEEE Transactions on Ultrasonics, Ferroelectrics and Frequency Control, Vol.53, No.8, August 2006.

[48] Goksen G. Yaralioglu, Arif S. Ergun, Baris Bayram, Theodore Marentis, B.T. Khuri-Yakub, *Residual stress and Young's modulus measurement of capacitive micromachined ultrasonic transducer membranes*, IEEE Ultrasonics Symposium, Vol.2, pp.953-956, October 2001.

[49] M. Kaltenhacher, H. Landes, K. Niederer, R. Lerch, *3D Simulation of Controlled Micromachined Capacitive Ultrasound Transducers*, IEEE Ultrasonics Symposium, 1999.

[50] David T. Yeh, Omer Oralkan, Ira O. Wygant, Matthew O'Donnell, Butrus T. Khuri-Yakub, *3-D Ultrasound Imaging Using a Forward-Looking CMUT Ring Array for Intravascular/Intracardiac Applications*, IEEE Transactions on Ultrasonics, Ferroelectrics, and Frequency Control, Vol.53, No.6, June 2006.

[51] Ira O. Wygant, Mario Kupnik, Jeffry C. Windsor, Wayne M. Wright, Mark S. Wochner, Goksen G. Yaralioglu, Mark F. Hamilton, Butrus T. Khuri-Yakub, *50 kHz Capacitive Micromachined Ultrasonic Transducers for Generation of Highly Directional Sound with Parametric Arrays*, IEEE Transactions on Ultrasonics, Ferroelectrics, and Frequency Control, Vol.56, No.1, January 2009.

[52] Ayhan Bozkurt, *A Lumped-Circuit Model for the Radiation Impedance of a Circular Piston in a Rigid Baffle*, IEEE Transactions on Ultrasonics, Ferroelectrics, and Frequency Control, Vol.55, No.9, September 2008.

[53] Matthew I. Haller, Butrus T. Khuri-Yakub *A Surface Micromachined Electrostatic Ultrasonic Air Transducer*, IEEE Transactions on Ultrasonics, Ferroelectrics, and Frequency Control, Vol.43, No.1, January 1996.

[54] Sudeep Bosu, Baskaran Sundaram, *Advantages, Limitations and Error Estimation of Mixed Solid Axisymmetric Modeling*, International ANSYS Conference Proceedings, 2004.

[55] Alessandro Caronti, Giosui Caliano, Antonio Iula, Massimo Pappalardo, *An Accurate Model for Capacitive Micromachined Ultrasonic Transducers*, IEEE Transactions on Ultrasonics, Ferroelectrics, and Frequency Control, Vol.49, No.2, February 2002.

[56] Ira O. Wygant, Mario Kupnik, Butrus T. Khuri-Yakub, *Analytically Calculating Membrane Displacement and the Equivalent Circuit Model of a Circular CMUT Cell*, IEEE Ultrasonics Symposium Proceedings, 2008.

[57] X.Zhuang, A.Nikoozadeh, M A Beasley, G.G.Yaralioglu, B.T.Khuri-Yakub, B.L.Pruitt *Biocompatible coatings for CMUTs in a harsh, aqueous environment*, IOPScience Journal of Micromechanics and Microengineering, Vol.17,No.5, May 2007

[58] Mohammed H. Badi, Goksen G. Yaralioglu, A. Sanli Ergun, Sean T. Hanseu, Eehern J. Wong, Butrus T. Khuri-Yakub *Capacitive Micromachined Ultrasonic Lamb Wave Transducers Using Rectangular Membranes*, IEEE Transactions on Ultrasonics, Ferroelectrics, and Frequency Control, Vol.50, No.9, September 2003.

[59] Alessandro Caronti, G. Caliano, R. Carotenuto, A. Savoia, M. Pappalardo, E. Cianci, V. Foglietti *Capacitive micromachined ultrasonic transducer (CMUT) arrays for medical imaging*, Elsevier Microelectronics Journal, Vol.37, No.8, August 2006.

[60] Serena H. Wong, Mario Kupnik, Ronald D. Watkins, Kim Butts-Pauly, Butrus T. (Pierre) Khuri-Yakub *Capacitive Micromachined Ultrasonic Transducers for Therapeutic Ultrasound Applications*, IEEE Transactions on Biomedical Engineering, Vol.57, No.1, January 2010.

[61] Amin Nikoozadeh, Pierre T. Khuri-Yakub *CMUT With Substrate-Embedded Springs For Non-Flexural Plate Movement*, IEEE Ultrasonics Symposium, San Diego, CA, Oct. 11-14, 2010.

[62] K.K. Park, H.J. Lee, G.G. Yaralioglu, Ö. Oralkan, M. Kupnik, C.F. Quate, B.T. Khuri-Yakub, T. Braun, H.P. Lang, M. Hegner, C.Gerber, J. Gimzewski *Capacitive micromachined ultrasonic transducers for chemical detection in nitrogen*, Applied Physics Letters, Letter 91, 2007.

[63] Srikant Vaithilingama, Ira O. Wyganta, Paulina S. Kuoa, Xuefeng Zhuanga, Omer Oralkana, Peter D. Olcottb, Butrus T. Khuri-Yakuba, *Capacitive Micromachined Ultrasonic Transducers (CMUTs) for Photoacoustic Imaging*, Proceedings of SPIE, Vol.6086, 2006.

[64] Omer Oralkan, A. Sanlı Ergun, Jeremy A. Johnson, Mustafa Karaman, Utkan Demirci, Kambiz Kaviani, Thomas H. Lee, Butrus T. Khuri-Yakub, *Capacitive Micromachined Ultrasonic Transducers: Next-Generation Arrays for Acoustic Imaging?*, IEEE Transactions on Ultrasonics, Ferroelectrics and Frequency Control, Vol.49, No.11, November 2002.

[65] Yongli Huang, Xuefeng Zhuang, Edward O. Haeggstrom, A. Sanli Ergun, Ching-Hsiang Cheng, Butrus T. Khuri-Yakub, *Capacitive micromachined ultrasonic transducers (CMUTs) with isolation posts*, IEEE Ultrasonics Symposium, Vol.3, August 2004.

[66] Yongli Huang, Xuefeng Zhuang, Edward O. Hæggstrom, A. Sanli Ergun, Ching-Hsiang Cheng Butrus T. Khuri-Yakub, *Capacitive Micromachined Ultrasonic Transducers with Piston-Shaped Membranes: Fabrication and Experimental Characterization*, IEEE Transactions on Ultrasonics, Ferroelectrics and Frequency Control, Vol.56, No.1, January 2009.

[67] Yongli Huang, Edward O. Hæggström, Xuefeng Zhuang, Arif S. Ergun, and Butrus. T. Khuri-Yakub, *Capacitive micromachined ultrasonic transducers (cmuts) with piston-shaped membranes*, IEEE Ultrasonics Symposium, Vol.1, pp.589-592, September 2005.

[68] Dominique Certon, F. Patat, C. Meynier, F. Teston, *Collective Behavior of cMUT cells for the prediction of electroacoustic response and directivity pattern*, IEEE Ultrasonics Symposium, pp.1967-1970, October 2006.

[69] E. Kohn, P. Gluche, M. Adamschik, *Diamond MEMS, a new emerging technology*, Diamond and Related Materials, Vol.8, No.2, March 1999.

[70] Xuecheng Jin, Igal Ladabaum, F. Levent Degertekin, Sam Calmes, Butrus T. Khuri-Yakub, *Fabrication and Characterization of Surface Micromachined Capacitive Ultrasonic Immersion Transducers*, IEEE Journal of Microelectromechanical Systems, Vol. 8, No.1, March 1999.

[71] Yongrae Roh, Butrus T. Khuri-Yakub, *Finite Element Analysis of Underwater Capacitor Micromachined Ultrasonic Transducers*, IEEE Transactions on Ultrasonics, Ferroelectrics and Frequency Control, Vol.49, No.3, March 2002.

[72] Yongrae Roh, Butrus T. Khuri-Yakub, *Finite Element Modeling of Capacitor Micromachined Ultrasonic Transducers*, IEEE Ultrasonics Symposium, Vol.1, pp.905-908, October 2000.

[73] Goksen G. Yaralioglu, A. Sanli Ergun, Butrus T. Khuri-Yakub, *Finite-Element Analysis of Capacitive Micromachined Ultrasonic Transducers*, IEEE Transactions on Ultrasonics, Ferroelectrics and Frequency Control, Vol.52, No.12, December 2005.

[74] Franck Teston, Dominique Certon, Frédéric Patat, Nicolas Felix, *Implementation of master curves for cMUT arrays design*, IEEE Ultrasonics Symposium, pp.1933-1936, September 2005.

[75] J. Pei, B. T. Khuri-Yakub, F.L. Degertekin, B.V.Honein, F.E.Stanke, Krishna C. Saraswat, *In situ simultaneous measurement of temperature and thin film thickness with ultrasonic techniques*, IEEE Ultrasonics Symposium Proceedings, Vol.2, pp.1039-1042, November 1996.

[76] Mohammed H. Badi, Goksen G. Yaralioglu, A. Sanlı Ergun, Sean T. Hansen, B.T. Khuri-Yakub, *Lamb Wave Devices Based On Capacitive Micromachined Ultrasonic Transducers*, IEEE Ultrasonics Symposium Proceedings, Vol.2, pp.1031-1034, October 2002.

[77] Annette Lohfink, Peter-Christian Eccardt, *Linear and Nonlinear Equivalent Circuit Modeling of CMUTs*, IEEE Transactions on Ultrasonics, Ferroelectrics and Frequency Control, Vol.52, No.12, December 2005.

[78] Yukihide Tsuji, Mario Kupnik, Butrus T. Khuri-Yakub, *Low Temperature Process for CMUT Fabrication with Wafer Bonding Technique*, IEEE Ultrasonics Symposium, October 2010.

[79] Orlando Auciello, James Birrell, John A Carlisle, Jennifer E Gerbi, Xingcheng Xiao1, Bei Peng, Horacio D Espinosa, *Materials science and fabrication processes for a new MEMS technology based on ultrananocrystalline diamond thin films*, IOPScience Journal of Physics: Condensed Matter, Vol.16, No.16, April 2004.

[80] I. Ladabanm, X. Jin, H.T. Soh, F. Pierre, A. Atalart, B.T. Khuri-Yakub, *Microfabricated Ultrasonic Transducers: Towards Robust Models and Immersion Devices*, IEEE Ultrasonics Symposium Proceedings, Vol.1, pp.335-338, November 1996.

[81] F. Levent Degertekin, Abdullah Atalar, Butrus T. Khuri-Yakub, *Micromachinable ultrasonic leaky wave air transducers*, Applied Physics Letters, Vol.73, No.6, August 1998.

[82] Jeremy A. Johnson, Mustafa Karaman, B.T. Khuri-Yakub, *Phased Subarray Processing for Underwater 3D Acoustic Imaging*, OCEANS'02 MTS/IEEE, vol.4, pp.2145-2151, October 2002.

[83] B.T. Khuri-Yakub, F.L. Degertekin, X.C. Jin, S. Calmes, I. Ladabaum, S. Hansen, X.J. Zhang, *Silicon micromachined ultrasonic transducers*, IEEE Ultrasonics Symposium Proceedings, Vol.2, pp.985-991, October 1998.

[84] Omer Oralkan, Xuecheng Jin, F. Levent Degertekin, Butrus T. Khuri-Yakub, *Simulation and Experimental Characterization of a 2-D Capacitive Micromachined Ultrasonic Transducer Array Element*, IEEE Transactions on Ultrasonics, Ferroelectrics and Frequency Control, Vol.46, No.6, November 1999.

[85] Xuecheng Jin, Igal Ladabaum, Butrus T. Khuri-Yakub, *The Microfabrication of Capacitive Ultrasonic Transducers*, IEEE Journal of Microelectromechanical Systems, Vol.7, No.3, pp.295-302, September 1998.

[86] Selim Olcum, Muhammed N. Senlik, Can Bayram and Abdullah Atalar, *Design Charts to Maximize the Gain-Bandwidth Product of Capacitive Micromachined Ultrasonic Transducers*, IEEE Ultrasonics Symposium, Vol.4, pp.1941-1944, September 2005.

[87] Nadim Maluf, Kirt Williams, *An Introduction to Microelectromechanical Systems Engineering*, Artech House, Inc., 2004.

[88] Jan G. Korvink, Oliver Paul, *MEMS: A Practical Guide to Design, Analysis, and Applications*, Williams Andrew Publishing, 2006.

[89] Antonio Arnau Vives, *Piezoelectric Transducers and Applications*, Springer, 2008.

[90] Frank Fahy, Paolo Gardonio, *Sound and Structural Vibration*, Elsevier, 2007.

[91] Ian R. Sinclair, *Sensors and Transducers*, Butterworth-Heinemann, 2001.